

POLITECNICO DI TORINO

Master of Science in Electrical Engineering

Academic Year 2018 - 2019



Master of Science Thesis

**Advanced Transient Thermal Modeling
of Traction Motors in COMSOL**

Supervisors:

Prof. *Aldo Boglietti* – Politecnico di Torino (Italy)

Dr.-Ing. *Shafigh Nategh* – ABB AB (Sweden)

**Candidate:
*Claudio Scema***

April 2019



Advanced Transient Thermal Modeling of Traction Motors in COMSOL

Claudio Scema

Politecnico di Torino
Facoltà di Ingegneria - Dipartimento Energia
Corso di Laurea Magistrale in Ingegneria Elettrica
Anno Accademico: 2018 - 2019

Relatori:

Prof. Aldo Boglietti
Politecnico di Torino
Torino, Italy

Dr.-Ing. Shafiqh Nategh
ABB AB Traction Motors
Västerås, Sweden

Candidato:

Claudio Scema

Turin, 15 April 2019

Abstract

This thesis has been performed thanks to work project collaboration between Politecnico di Torino (Turin, Italy) and ABB AB Traction Motors (Västerås, Sweden).

It deals with study and thermal analysis of electric motors for high-performance applications, where focus is placed on electric traction motors for e-mobility and railway applications. Calculations are done in COMSOL, a simulation software for Computational Fluid Dynamic calculation.

The thesis can be divided in six main topics.

In the first chapter, focus is on different cooling layouts for electric motor, operating conditions of traction motor and finally different thermal modelling methods. The thesis structure is presented and a list of publications in which the author has contributed to during this M.Sc. project are finally indicated.

At the chapter 2, numerical modeling of cooling flow is presented. First an introduction is given on different Computational Fluid Dynamic (CFD) methods including finite element and finite volume. The second part of this chapter focuses on the geometry fan building with which I worked in COMSOL, with exhaustive explanation about main functions. Subsequently, calculation solvers and mesh setups are elaborated. Finally, air flow results are presented.

Chapter 3 is reserved to the presentation and discussion of the developed CFD model to calculate the air flow in the motor as input for the complete thermal model.

At the chapter 4, traction motor model is presented and temperature results, obtained from thermal simulations, are discussed.

In chapter 5, the experimental setup is outlined and a comparison between simulation and measurements results is presented. At last, another thermal experimental method, about *Short-Time Transient Thermal Measurements Method*, is discussed.

Conclusions and future works resulting from this study in chapter 6 are discussed.

Finally, in the appendix A, B and C are respectively listed the acronyms and measurement units used and the selected publications from this project.

Index Terms: *Electric Motors, Railway Traction, E-Mobility, Computational Fluid Dynamic, Thermal Modeling, Heat transfer, Cooling Layouts, Finite Elements, Lumped Parameters, COMSOL, MATLAB, Excel.*

Sommario

Questo lavoro di tesi è il risultato di una collaborazione tra il Politecnico di Torino (Torino, Italia) e la multinazionale svizzero-svedese ABB, in particolare il ramo ABB AB Traction Motors (Västerås, Svezia).

Il lavoro concerne lo studio e l'analisi termica dei motori elettrici per trazione, con particolare attenzione rivolta ai motori per trazione ferroviaria e per l'e-mobility. I calcoli e le simulazioni di fluidodinamica computazionale sono stati eseguiti in COMSOL.

La tesi è stata elaborata in sei principali capitoli.

Nel primo capitolo sono presentate le differenti tecnologie di raffreddamento dei motori elettrici, le diverse condizioni di funzionamento dei motori per trazione e i possibili metodi di modellizzazione termica.

La struttura del tesi è presentata seguita dalla lista delle pubblicazioni in cui l'autore ha collaborato durante il progetto di tesi magistrale.

Nel capitolo 2 è stato presentato il modello numerico del flusso di raffreddamento. Successivamente ad una introduzione riguardo la fluidodinamica computazionale (CFD), ed il metodo agli elementi finiti, l'attenzione è stata rivolta al modello in COMSOL della ventola, spiegando le funzioni del tool, il risolutore e la mesh applicati. Infine, sono discussi i risultati relativi ai calcoli fluidodinamici.

Il terzo capitolo è riservato alla presentazione del modello CFD sviluppato per calcolare i valori di flusso d'aria nel motore che costituiranno l'input per il modello termico completo.

Nel capitolo 4 è presentato il modello termico completo del motore, con un'analisi teorica e modellistica del modello in COMSOL, discutendo infine i risultati termici ottenuti.

Il capitolo 5 è riservato al confronto dei risultati, fluidodinamici e termici, calcolati e misurati. L'ultima parte del capitolo è dedicata alla presentazione del metodo di analisi termica *Short-Time Transient Thermal Measurements Method*.

Nel capitolo 6 sono presentate le conclusioni ed i possibili sviluppi futuri conseguenti dallo studio effettuato.

Infine, nell'appendice A, B e C sono riportati rispettivamente gli acronimi e le unità di misura adottati nella stesura e le pubblicazioni derivanti da questo progetto.

Parole Chiave: *Motori elettrici, Trazione Ferroviaria, Mobilità Elettrica, Fluidodinamica Computazionale, Modellizzazione Termica, Trasferimento di Calore, Tecnologie di raffreddamento, Elementi Finiti, Parametri Concentrati, COMSOL, MATLAB, Excel.*

Acknowledgements

This thesis was carried out to conclude my Master of Science in Electrical Engineering at the Politecnico di Torino.

For this work, first of all, I would like to thank my main supervisor Dr.-Ing. Shafiq Nategh, for the opportunity given to me to apply my knowledges, studies and skills on a great project in ABB, moreover, to thank him for his time, suggestions and chance during these almost twelve months and for his hospitality during my internship at ABB AB at Västerås, in Sweden.

I would also thank my academic professor Aldo Boglietti for his teachings, opportunities and time whenever it was necessary.

I further would like to thank all my family; my father, my mother and my sister Jlenia for their encouragement and aid and, together to uncles and cousins, for their unfailing support, suggestions and comprehension along the way.

I want to thank for my colleague and friend Fabio Piras for his whenever suggestions and presence since the first day and for my colleague Luca Boscaglia with which I have worked hard during the last year.

Last, but not least, I would extend my thanks for all my friends; I would like to write their names one by one but I limit myself to thank the friends known in these years in Turin of the "Isperv" group, who now historical from University of Cagliari and also the new friends known in Turin, for their support, fun and parties.

Claudio Scema
Turin, Italy
April 2019

Contents

1	Introduction	1
1.1	Thermal Analysis of Traction Motors	1
1.2	Traction Motors Cooling Layouts	2
1.3	Traction Motors Operating Conditions	6
1.4	Different Thermal Modeling Methods	7
1.4.1	Thermal Modeling Methods: Analytical Approach	7
1.4.2	Thermal Modeling Methods: Numerical Method	9
1.5	Thesis Structure	11
1.6	List of Publications	12
2	Numerical Modeling of Cooling Flow	13
2.1	Introduction: Finite Element vs. Finite Volume	13
2.2	Geometry Building	18
2.3	Boundary Conditions	22
2.4	Solver Setup	25
2.5	Mesh Setup	29
2.6	Fluid Velocity Results	33
3	CFD Modeling of Traction Motors	44
3.1	Introduction	44
3.2	Model Building and Setting	45
3.3	Solver Setup: <i>Frozen Rotor</i> Function	47
3.4	Mesh Qualities	48
3.5	CFD Results	53
4	Thermal Modeling of Traction Motors	57
4.1	Introduction	57
4.2	Analytical Thermal Model	59
4.3	Thermal Modeling in COMSOL	64
4.3.1	Geometry and Physics	64
4.3.2	Solver and Mesh Setting	68
4.4	Temperature Results	70

5	Experimental Results	73
5.1	Experimental Measurements Setup	73
5.2	Flow Measurements	74
5.3	Thermal Measurements	76
5.4	Short-Time Transient Thermal Measurements Method	79
5.4.1	Experimental Test Setup	80
5.4.2	Experimental Test Results	82
6	Conclusion and Future Works	87
6.1	Final Summary	87
6.2	Future Developments	88
A	List of Acronyms	89
B	List of Measurement Units	92
C	List of Selected Publications	93
	List of Figures	94
	List of Tables	97
	Bibliography	98

Chapter 1

Introduction

In this chapter thermal modeling of electric motors, with focus on electric traction motors, are analyzed. Different cooling layouts of traction motors, different operating conditions and finally different thermal modelling methods are presented.

1.1 Thermal Analysis of Traction Motors

The high demand for life cycle costs is an important issue for electric traction motors, especially in e-mobility and railway applications. These costs include production and maintenance costs during life time. Consequently, long maintenance intervals are needed that can be in the range of thousands of kilometres. This involves accumulation of dirt in electric components, especially in trains operating in dirty environments, such as subways. In this case, the main problem in the traction motor is the blockage of rotor and stator ducts resulting in high temperature in the critical parts, e.g. winding and bearing. This can reduce the life time of the components and the motor. It is estimated that the life time of the insulation of the windings is reduced by half, for each increment of 10 degrees of the temperature. This itself explains the great importance of thermal calculations for efficient use of electric traction motors.

To implement an efficient thermal model, operating and cooling conditions of traction motors should be considered. In fact, for example in railway traction, traction motors are run on their thermal capacity which needs dimensioning according to duty cycle operation during transient; instead, industrial motors are dimensioned in respect to their thermal performance corresponding to a specific operating point. This involves requirements on the thermal models developed for railway traction to have an accurate and fast behaviour in both steady state and transient operating [1].

Based on this, thermal modeling methods are therefore important to define and to make an accurate estimation of temperature in the critical parts of the motor. As shown in below, main approaches that are studied and used for this kind of calculation are analytical and numerical methods.

In particular, the analytical model is mainly based on lumped parameters, however, the numerical methods are based on finite elements and computational fluid dynamic calculations.

The model presented in this thesis is based on a combination of analytical and numerical models where, in particular, the complex solid parts, e.g. windings, are modeled using the numerical method and lumped parameters modeling is used to model the motor end parts.

The analytical modeling is based on lumped parameters and allows to represent through a simplify model in which fields that are distributed in the space can be approximated as a number of single scalars. However, this is an efficient way to calculate a thermal parameters, often the estimate of temperature in critical parts only with lumped parameters modeling is not very accurate and may result in an imprecise estimation of temperature. Numerical methods based on finite elements and computational fluid dynamic calculations provides the possibility to solve this problem and to improve the accuracy of temperature estimation in motor critical points, however they are normally time-consuming to develop and solve [2].

Finally, the combination of two modeling methods enables obtaining an efficient method to estimate temperature, also in critical parts, with a reasonable calculation time and accuracy. Furthermore, using combination it is possible to study the influence of stator and rotor ducts on the motor thermal performance, also in the cases where stator and rotor ducts are blocked due to dirt accumulation.

1.2 Traction Motors Cooling Layouts

In high-performance applications, such as traction motors, high torque/power density is increasingly required. To obtain high power density, two methods can be employed. The first method is based on high density of current in the windings of motors and the second is instead based on high speed of rotor rotation. Both methodologies have advantages and disadvantages. In the first place, working with high density of current involves high copper loss and, therefore, high temperature in the points, so called “hot spots”.

Having high speed of rotor implies high current and voltages frequencies which increases copper and iron losses. In the case that produced heat is not adequately dissipated, the temperature would increase with problems in the motor parts that are difficult to access, e.g. the rotor. It follows, therefore, that in traction applications, the demand for high torque and power density requires special attention to the development of an efficient cooling method. In this regard, many and different cooling methods have been presented and analyzed, with reasonable temperature results in critical parts of motor. Among different methods studied, the one mainly exploited is indeed the method based on air forced-ventilation, specifically as it provides the motor with a clean and constant cooling, that make it less sensitive in respect to the operating point of motor and the external environmental conditions.

However, this cooling method needs more space for air ducts and external fan.

This, in particular, in the applications such as subways, can be a problem as reduces available sitting space.

However, it is also necessary to add that, in the event where the current density in the motor is very high, this method may not be suitable and the needs for liquid cooling arises. When the coolant is water, cooling of the winding is obtained faster, but it is not particularly optimal because it causes problems, mainly on motors with long end windings and with a reduced number of poles.

An alternative to water, the oil can be used. In the directly oil cooled motors, an efficient cooling of end windings and rotor is possible.

Before describing different cooling layouts of electric traction motors, it can be mentioned that, in order to decide the cooling system configuration, distribution of losses when motor is run in duty cycles is considered. This, from a thermal point of view, raises the need to reduce losses in motor critical points such as windings or bearings.

However, after that, attention must be paid to the spaces required for cooling systems. In general, the cooling system should provide heat dissipation at each critical point in an efficient manner.

Before looking in detail, cooling systems are classified based on coolant types and cooling methods. Cooling systems can be divided into inducted or forced ventilation. If it is inducted type the shaft-mounted fan builds air pressure inside motor, sucking in it and pushing out. In the forced cooling, air is forced by the external fan to the motor and pushed out.

I. Open Air Forced-Ventilated Cooling

Referring to electric traction motors, such as high-speed trains and locomotives, it can be said that the cooling method is mainly forced air cooling with framed or frameless design.

As already mentioned above, the main reason for the use of forced ventilation is to have the possibility of ensuring high levels of torque and power that needs efficient cooling regardless of the operating points of the motor.

The need for high torque density involves high windings losses and as a result more cooling. However, this limits applicability of cooling methods based on shaft-mounted fan as cooling depends on motor speed in this kind of cooling topology. In general, with wheel diameters in the range of 840-920 mm, and rotational speeds below 6500 rpm, the gear ratio is in the range of 3. The low gear ratio raises the need for the motor to supply a high level of torque.

From a flow point of view, the air flowing in the motor passes three parallel paths of rotor ducts, stator ducts and air gap. Air forced-ventilated traction motors are supplied by the fans externally located on the roof. This could guarantee good air quality for ventilation in comparison to cases in which the fan is mounted on the shaft. Best air quality means also lower risk to block ventilation ducts.

Overall, air forced ventilated cooling systems represent a technological solution now consolidated but much expensive. Therefore, focus on cost reductions could represent a challenge for this cooling configuration in future. As mentioned above, air forced ventilation can be implemented in both framed and frameless designs as shown in figure 1.1 below comes from [1].

In the framed design, the stator lamination is covered by a round, e.g. aluminium case, where the cooling ducts are located.

However, in a frameless design cooling is directly applied to the stator lamination.

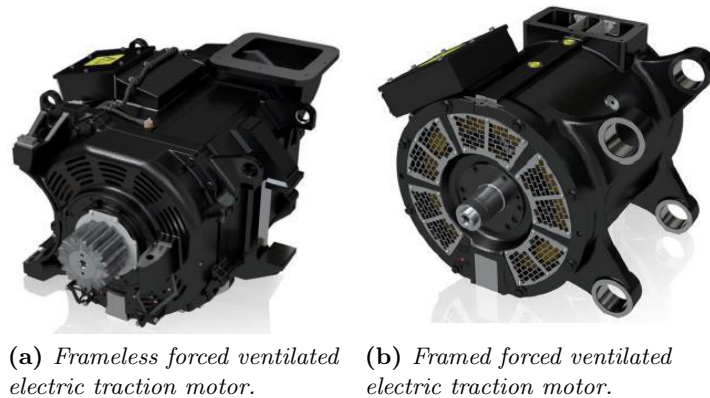


Figure 1.1: Open air forced ventilated motors [1].

II. Open Air Self-Ventilated Cooling

Regarding electric traction motor for subways, main cooling method is based on open self-ventilation. In this cooling topology, as showed in the picture, the shaft-mounted fan is able to guarantee air flow in rotor and stator cooling ducts as well as the air gap.

Despite forced cooling method described above, in which rotational speed is below 6500 rpm, in self-ventilated motors rotation speed is lower and in the range of 5500 rpm. The limitation in the speed mainly due to limitation in the maximum mechanical stresses that can be handled by the shaft-mounted fan.

Main advantage for this cooling systems is facility of design, without air ducts and the need for the fan placed externally. This represents a cost benefit that is lower than forced ventilated system. Subways have max speeds about 150 km/h which is not high and provide the possibility for having a high gear ratio.

The higher gear ratio reduces the need for extreme cooling as the requested torque in the motor lowers. However, a limiting factor for this motor type is the necessity to ensure an acceptable range of noise and of mechanical vibrations of rotating parts. The air quality is normally lower in this kind of cooling that raises the need for filters to avoid decrease of life time in motor critical components.

In figure 1.2 an example of open air self-ventilated electric traction motor is shown.



Figure 1.2: Open air self-ventilated electric traction motor [1].

III. Enclosed Air Self-Ventilated Cooling

Another cooling type which is analysed is enclosed air self-ventilated cooling. From efficiency point of view, this motor type is compared to open air self-ventilated. Its structure provides two separate areas, inner and external. In the outer area, radial fan is mounted on the shaft to provide air flow through external stator laminations. In the inner area, air flows around stator end windings through wafers mounted on the rotor circuit ring.

The two main reasons that provides the possibility of using this method are linked to environmental conditions. For example, in the city trams the cooling air is supplied from the bottom of floorboard, but it is not clean containing high level of dirt and dust. The second reason is linked to fact that, in case of permanent magnet motor, metallic and magnetic parts should not be in contact with rotor.



Figure 1.3: Enclosed air self-ventilated motor electric traction motor [1].

IV. Enclosed Liquid Cooling

Finally, the last method to cool the motor involves the liquid cooling. Main liquids used are oil and water. In this method, heat transfer occurs through the cooling ducts located in the housing. However, it is necessary to use a housing water jacket because the water cannot be in direct contact with the inner parts of motor, as for example the stator and rotor steel laminations.

In this regard, the water flows in controlled paths and this provides the possibility for more accurate modeling of heat transfer in the coolant ducts.

In conclusion, the main advantages of water cooling are the reduction of vibrations and noise emissions compared to air ventilated cooling where fan is main source of noise and the compactness of the design in comparison to air-cooled motor. However, the main disadvantage of indirect liquid cooling is the reduced cooling of the end windings especially in the motors with long end windings. New approached e.g. potting is proposed to solve this issue.

1.3 Traction Motors Operating Conditions

In railway traction, motors are dimensioned based on their thermal behaviour in transient state when running in duty cycles. An efficient model should be able to simulate thermal behaviour of the motor for long running profiles so called thermal dimensioning cycles. These operating cycles are defined by the operator and characterize the train operation when it starts from the first station and ends in the final station.

As an example, figure 1.4 presents a typical duty cycle and show how stator winding and bearing temperature changes as a function of time when motor torque and speed are varied [2]. In Fig. 1.4 torque (in black line), starting to 0 s, torque increases positive and negative alternately until 2000 s where it becomes constant over time until 3000 s. Also, the speed (in blue line) increases and reduces from 0 s to 2000 s but it remains at zero level until 3000 s because in this range of time the train is stopped. Consequently, the temperature of the winding (in brown line estimated and green line measured) increases from 0 s to 2000 s, then decreases until 3000 s and finally increases again.

About the bearing, considering the same torque and speed, the thermal behaviour is similar except that due to the higher thermal capacity, the temperature (in brown line estimated and green line measured) is less dependent on load and speed.

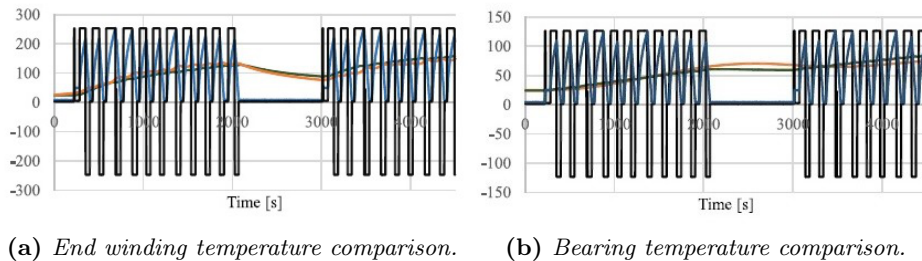


Figure 1.4: Comparison between estimated (brown) and measured (green) temperature of the end winding (a) and of the bearing (b), at specific torque (black) and speed (blue) [2].

The abovementioned operating condition involves a detailed requirement about the thermal model to be accurate and fast functioning both in the steady state and transient operating. So, as in detail described in chapter 1.4., in this thesis the complete thermal model is defined by analytical model and numerical model.

In particular, to avoid transient numerical modeling, the numerical model with CFD calculation is used only to be run in a single operating point and then heat transfer coefficients (HTC) are calculated and scaled based on motor or fan speed with analytical method.

1.4 Different Thermal Modeling Methods

As introduced in the preface, the complete developed thermal model is a combination of two approaches [2].

The first approach is based on analytical method particularly lumped parameter modeling (LP) and the second method is based on numerical method including finite element and fluid dynamics calculation (FE and CFD, respectively).

Both approaches, however, should meet the following targets:

- Possibility to estimate hot spot temperature in critical motor points with an acceptable accuracy;
- A reasonable transient calculation time;
- Possibility to implement the model in a fast manner to be able to use in a design optimization process.

1.4.1 Thermal Modeling Methods: Analytical Approach

The first attempt to develop an analytical thermal model was to provide temperature estimations in the electric motor different parts based on thermal network for induction motors. An analytical model with LP can be developed so that results are obtained with reasonable precision assuming *thermal resistances* and *capacitances* quite accurately. In particular, with LP modeling the heat transfer laws can be described based on the dimensional data of motor and the thermal properties of the material used. For example, a simple thermal model of electric motor is shown in figure 1.5, in which the thermal resistance R_{ew1} allows to model half of the end winding coil and the slot surface of the stator slot to the middle of end winding. Based on this example scheme, also other thermal resistances R_{ew2} can be calculated using the general equation of heat conduction in solid materials.

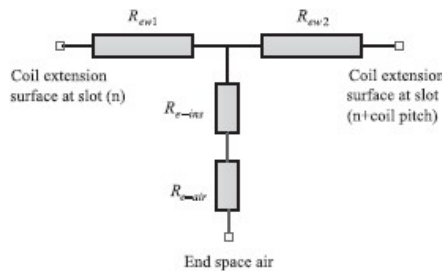


Figure 1.5: Example of analytical LP model of the end winding [2].

Thermal capacitances can be calculated based on the component's specific heat, density and volume. Obviously, the number of model elements with resistances and capacitances is a function of the motor design, the number stator slots, etc. In figure 1.6, a simple LP thermal model is shown where heat transfer laws are represented. The table of parameters can be found in table 1.1.

Complete thermal model consists of analytical thermal models of different motor parts and by heat data, such as the heat transfer in the winding, copper and iron losses, etc.

Knowing this, it is possible to estimate temperature distribution in every part of motor, using a thermal network.

At last, thermal model based on the analytical approaches cannot be used to model accurately the thermal effects of complex structures of electric motors, even though this modeling method is simple and quick. In fact, for example, analytic methods can risk underestimating the hot spot temperature of winding [3].

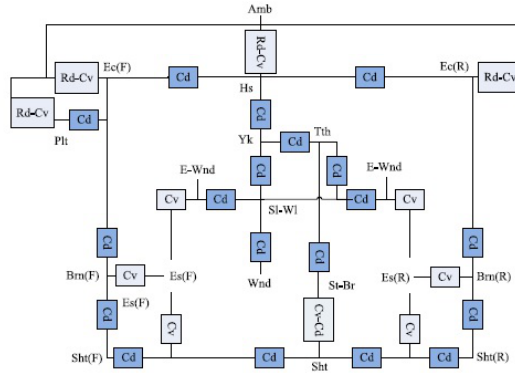


Figure 1.6: Example of lumped parameters thermal model of an electric motor [3].

Symbol	Abbreviation	Symbol	Abbreviation
F	Forward	Hs	Housing
R	Rear	Plt	Plate
Cd	Conduction	Sht	Shaft
Cv	Convection	Sl-Wl	Slot wall
Rd	Radiation	St-Br	Stator bore
Brn	Bearing	Yk	Stator yoke
Ec	End cap	Tth	Stator tooth
Es	End space	Wnd	Winding
E-Wnd	End winding	-	-

Table 1.1: List of model parameters [3].

1.4.2 Thermal Modeling Methods: Numerical Method

As mentioned above, analytical models are not an efficient method when temperature in motors critical parts should be calculated. Consequently, it is necessary to employ numerical models.

The main numerical modeling methods are finite element analysis (FEA) and CFD. They allow solving this problem and to improve the temperature estimate in motor critical points.

In fact, through finite element analysis it is possible to calculate a precise picture of the temperature distribution in complex solid parts. Consequently, heat transfer in stator coils, stator lamination, housing can be modeled using this method. Particularly, using FE modeling it is possible to model the complete active part considering temperature variation in the insulation components and temperature difference between the cold side and the hot side of traction motors.

In this case, solid parts are modeled using thermal conductivity, specific heat and mass density of the material used.

FEA can guarantee an accurate picture of temperature distribution in solid parts, however, convective heat transfer to the coolant should be modeled using boundary conditions [3]. In detail, colours represent different solid elements; for example, stator steel laminations are grey, conductors are yellow, insulation is dark blue, impregnation is light blue and end winding ring is green. In the below picture, temperature distribution in a FE model is presented.

The CFD analysis are made to model, for example, the complex distribution of the air between the stator ducts, air gap and rotor ducts as well as to estimate the air velocity in the motor end parts. In particular, in the CFD model of the forced-ventilated motor, the external fan for ventilation can be replaced by a boundary condition that represents pressure-flow curve.

However, in a CFD model of a self-ventilated fan, the fan should be included in the CFD model.

CFD analysis is time-consuming. In particular, it is less adapted for the design process with a high number of iterations. Therefore, it is not convenient to use this modeling method in the optimization process of design.

Summarizing, the above-mentioned requirements described in the beginning of chapter 1.3. cannot be satisfactory by neither fully analytical nor numerical methods. In fact, to have an accurate estimation of the temperature, the fan performance, flow distribution, and flow in the motor end parts, are accurately described by numerical CFD calculations. However, this needs more time to calculate. About analytical model, as mentioned, it is not suitable to model thermal effects of the motor complex structures.

Finally, the complete thermal method analyzed is a combination of analytical and numerical modeling methods. In fact, for example to accurately estimation the hot spot temperature in windings, FE modeling is utilized, that is not able to represent flow and rotating parts.

Therefore, CFD calculation can be made to provide flow velocity and to calculate heat transfer coefficients. Additionally, analytical modeling is used to model heat transfer in motor non-active parts.

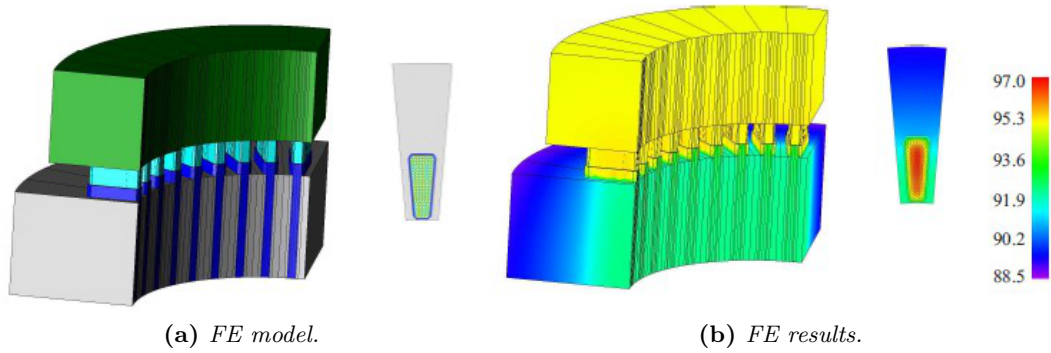


Figure 1.7: Example of thermal FE model of the stationary part of an electric motor [3].

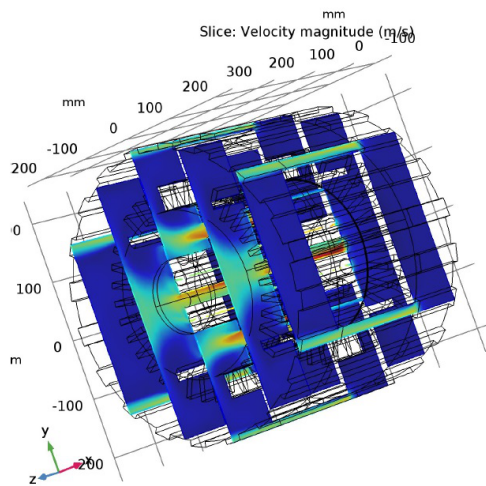


Figure 1.8: Example of velocity in CFD motor model.

1.5 Thesis Structure

This thesis is organized so that, in the chapters, the scientific background with theoretical and experimental concepts are presented.

It is structured as follows.

In chapter 2 numerical modeling of cooling flow is presented. In the first part of this, a theoretical presentation about fluid dynamic and Computational Fluid Dynamic methods, with focus on finite element and finite volume, is discussed. After this, an exhaustive presentation about the COMSOL fan modeling is presented, focussing on geometry building, mesh, and frozen rotor solver.

In the chapter 3 the attention is focussed on the motor model to calculate the flow rate and the air speeds in the motor ducts. Here, the motor model is built starting from the real geometry, a frozen rotor function solver is applied in function of different rotational speeds, and the flow results are obtained and explained.

Chapter 4 is divided in two main part. The first part is dedicated to explanation of the analytical modeling about heat transfer coefficient in different flow conditions, considering the flow results obtained from chapter 3. The second part is reserved to understand the modeling in COMSOL, in such that to achieve the thermal results as hybrid modeling, previously introduced.

In the chapter 5 the experimental measurements are calculated and compared both for flow and thermal modeling. The setting experimental conditions are explained and the comparison between measured and calculated results are discussed. The last part is instead reserved to explanation of three experimental tests to know the thermal parameters of the motor and to validate the *Short-Time Transient Thermal Measurements Method*. Good results for all test measurements are obtained.

Chapter 6 presents the conclusion of the thesis and supplies some future work and developments proposals from this work.

In appendix A and B the acronyms and measurement units are respectively reported and in appendix C the selected publications deriving this work are finally listed.

1.6 List of Publications

In this section a publications list in which the author has contributed to during this M.Sc. thesis project is reported.

- I. **C. Scema**, S. Nategh, A. Boglietti, L. Boscaglia, D. Ericsson, " *A Hybrid Thermal Modeling Method for Traction Motors Used in Duty-Cycles*", IEEE International Electric Machines and Drives Conference (IEMDC), San Diego (CA), May 2019.
- II. S. Nategh, A. Boglietti, E. Carpaneto, **C. Scema**, L. Boscaglia, " *An Optimization Method for Cooling System Design of Traction Motors*", IEEE International Electric Machines and Drives Conference (IEMDC), San Diego (CA), May 2019.
- III. L. Boscaglia, S. Nategh, A. Boglietti, **C. Scema**, F. Bonsanto, " *Conjugate Heat Transfer Model for Self Ventilated Traction Motors*" ¹

¹Submitted in IEEE Energy Conversion Congress and Expo (ECCE), Baltimore (MD), Sept. 2019

Chapter 2

Numerical Modeling of Cooling Flow

The author would thank Daniel Ericsson and COMSOL team for their efforts and contributions in this chapter.

After the introduction on two main thermal modeling methods, this chapter focuses on numerical modeling of cooling flow. An introduction on finite element method and finite volume method is given, followed by a presentation on geometry building, boundary conditions, solver and mesh setup of numerical model in COMSOL. Finally, fluid velocity results are analyzed.

2.1 Introduction: Finite Element vs. Finite Volume

As mentioned in chapter 1, to implement an efficient thermal model with an accurate estimation of temperature, the two main methods of analytical and numerical modeling can be used. However, in the case of flow calculation, analytical models are not accurate enough and numerical modeling is necessary.

CFD calculation can be defined as a branch of fluid mechanics which studies, solves and analyzes fluid flows problems through numerical analysis and data structures, where interaction between liquids and gases with surfaces are defined by boundary conditions. One advantage with using CFD calculation is the possibility to obtain a detailed local information about the simulated system. However, before getting into CFD calculation details, it is necessary to present some important concepts [17].

Firstly, fluids are substances in which their molecular structure does not resist to external cutting forces. In fact, even a little force causes deformation of a fluid particle. Both liquids and gases follow the same laws of motion. Fluid flow is caused by action of externally applied forces. They can be divided as surface forces or body forces. The first one, such as pressure or cutting forces, is created by a movement of a rigid wall relative to the fluid.

Instead the other one, such as gravity, is the induced forces by rotation. All fluids have a similar behaviour under action of forces, however their macroscopic properties are different considerably.

The properties of fluids, e.g. viscosity, density, surface tension and heat conduction, are intrinsic properties described through temperature and pressure. Instead, properties linked to the flow include pressure, turbulence and turbulent viscosity. Regarding flow behaviour, it is possible to divide it as laminar or turbulent, steady-state or transient and single or multi phase. In this case study, velocity and pressure are two important aspects and they allow to understand flow differences. In particular, if the speed is low, it is possible to ignore the inertia of the fluid. When the speed increases, inertia gets important but each fluid particle follows a regular trajectory; this means fluid is laminar.

In the laminar flow, through Navier-Stokes equations, the momentum transport of flow dominated by viscous forces is described. In this method, through Direct Numerical Simulation (DNS) of the Navier-Stokes equations, if the flow is laminar, the CFD allows to obtain an accurate flow simulation for single-phase systems. Subsequently, when the speed increases more and more, the flow becomes turbulent; the process of the laminar-turbulent transition is an important, but difficult, behaviour that needs more detailed study. Turbulent flow can be described through Navier-Stokes equations; however, due to flow properties, it is difficult to solve the equations.

A feasible solution, alternative to this but possible only for smaller flows, consists to solve only the large-scale turbulence, then filtering with low-scale out turbulence and modelling these through flow dependent viscosity. This method, called Large Eddy Simulation (LES) is, however, featured by high calculation time. So, in case of complex flow, it is not possible to solve using this method. Another alternative to Navier-Stokes equations is given through Reynolds-averaged Navier-Stokes (RANS) methods. In this way, turbulent variations are time averaged and a reasonable velocity average can be simulated. However, unfortunately, in this case some flow properties cannot be solved neither using this method. Laminar and turbulent flows described above can be analyzed in both single or multi-phase forms. In single-phase, it is possible to obtain an accurate solution for both laminar and turbulent flow. However, the main disadvantage is represented by simulation of the mixing of reactants for fast reactions. In fact, when the reaction rate is fast compared with mixing, there are problems with solving and therefore it needs to use a model for mixing coupled with a chemical reaction. Multi-phase flow, typically, is used for combination systems such as liquid-liquid, gas-liquid, gas-solid, gas-liquid-solid. If the multiphase system has small particles, reasonable results can be obtained. In other cases, the quality of the simulations is not excellent because good models for multiphase flow do not exist [15].

After this short introduction on the fluids and their characteristics, before discussing discretization methods, we need to consider that the procedure of CFD calculation is usually the same. As accurately subsequently described, in fact, it can be divided in three main parts, which are pre-processing, simulation and post-processing.

In the first, at the pre-processing step, the geometry is built and modelled, defining boundaries. Then a grid is built, dividing geometry into small computational cells (meshes). After, properties and the initial conditions, inlet, outlet and wall conditions are set.

Subsequently, in the second step, the equations are solved iteratively with a steady-state or transient, starting the simulation. In particular, the solver is chosen, iteration method (with steady-state or transient) and convergence requirement are defined.

Finally, in the post-processing step, the results are analyzed and studied.

The starting point of numerical method is the mathematical model with the set of partial differential equations (PDE) and boundary conditions. In fact, the flows and related phenomena can be described by PDE that, however, cannot be solved analytically. This involves to obtain an approximate numerical solution, needed to use a simplification based on discretization method which, in turn, can be solved through the computer, with a system of algebraic equations. The quality of discretization is linked to accuracy of numerical solutions, then discretization methods have a fundamental role in the CFD process and they need an accurate study.

Discrete element method means a group of numerical methods for computing the motion and effect of a large number of small particles. Typically, these are computationally intensive, which limits either the length of a simulation or the number of particles. PDE working with incompressible fluid flow are mainly the Navier-Stokes equations and the continuity equation. The non-linearity of the momentum equations represents the main complication for solving the governing equations. As above-mentioned, the main developed approaches to solve this problem exploit discretization methods and they mainly are the Finite Element Method (FEM), Finite Volume Method (FVM), and the Finite Difference Method (FDM).

In this work, only FEM and FVM are analyzed in detail.

I. Finite Elements Method

The FEM is a numerical method mainly used for problems such as structural analysis, fluid flow, heat transfer, mass transport or electromagnetic potential. The analytical solution of these problem types typically requires the resolution to boundary value problems for partial differential equations; instead, through FEM, the formulation allows a system of algebraic equations. FEM is used to reduce the governing PDE to a set of algebraic equations. The dependent variables are represented through polynomial shape functions over a small area (element). Then, these elements are substituted into governing PDE and the weighted integral over the element is considered where the weight function is chosen to be the same as the form function. In this way, the result is a group of algebraic equations for the dependent variable at discrete points or nodes on every element [18].

The process consists, starting by a large domain, in a subdivision in a group of smaller subdomains, in which each subdomain is represented by a set of element equations to the original problem and, subsequently, assembling the group of element equations in a global system of equations for the final calculation. This can be calculate starting from the initial values of the original problem. The domain is therefore broken into a set of finite elements (but discrete volumes are also possible). Often, in 2D they are triangles or quadrilaterals and in 3D tetrahedra or hexahedra.

In other words, it is a procedure in which the error of approximation is minimized by including test function into the PDE. The process approximates locally PDE through a group of algebraic equations to solve steady-state problems or with a group, in the case in which ordinary differential equations, to solve transient problems. So, the main principles on which FE is based, are definition of continuative domain and discretization of domain through fixed points number. Subsequently, for each discretized point is written an equation and the unknown domain is approximated with Taylor's development. If PDE are linear, these followed equations are also linear; in particular for steady-state problems, set of equations used involves numerical linear algebra methods, instead for transient problems are used Euler method or Runge-Kutta method, with numerical integration.

II. Finite Volumes Method

The second method analyzed is the FVM [19].

The principle of the FVM is the local conservation. In general, this is a method to represent and analyze the PDE in the algebraic form equations. The governing equations are integrated over a volume or cell with a linear variation of the dependent variables made into pieces. This linear variation is an indication of accuracy and complexity. In fact, through integrations, fluxes are balanced across the boundaries of the individual domain. Typically, this is a discretization method used for numerical simulation of mass conservation laws. Some aspects of finite volume (FV) are similar to FE, such as the possibility to applicate it in arbitrary geometries through structured or unstructured mesh [21].

It is also important to say that the numerical flow is preserved from every cell. Furthermore, this method is conservative locally because is based on equilibrium approaches, then, local balance is indicated in every cell. The FVM process, to solve numerically equations, involves the entire computational domain that needs to be divide into "small" sub-volumes (CVs), called cells or mesh, as done in the previous FEM. The variable of interest is therefore located in the center of the control volume. In this way, values are calculated at discrete places on a meshed geometry and so finite volumes are referred to the volumes surrounding each node point on a mesh.

The next step is to integrate the differential form of the governing equations over each control volume. In this way the discretization equation expresses the conservation principle for the variable inside the control volume.

The main advantage of FVM is the possibility that the solution satisfies quantity conservation. This is ever verified for any control volume, for entire computational domain and for any number of control volumes.

In particular, non-continuative solutions arising from compressible flows can be calculated through FV integrals in PDE containing a divergence term are converted to surface integral with divergence theorem.

Finally, to solve equations, iterative way is typically used; this involves domain discretization makes of a numerical error into the solution. So, it is important to control the magnitude of the error after a solution has been calculated. The error tends to zero when cell size approaches to zero, therefore a sufficient increase of the cell size will reduce the error well. Furthermore, reducing the cell size, a large number of cells are will be created, involving an increasing the computational effort. Before to understand when it is better to use FEM or FVM, in table 2.1 main differences between two methods are summarized.

	Finite Element	Finite Volume
Advantages	More mathematics involved; Natural boundary conditions; Master element formulation; Equality of difficulty to model any shaped geometry;	More physical significance; of the flows;
Disadvantages	Reduced physical significance of the flows;	More difficulty modeling for irregular geometries;

Table 2.1: Comparison of advantages and disadvantages for FE and FV.

FEM and FVM analyzed, in this case study FEM is applied.

In fact, the CFD tool, COMSOL, works with this method. However, it is necessary to understand when and why it is better to use FEM than FVM or vice versa. It is important to anticipate that does not exist a single optimal method that is always valid but, the accuracy, calculation time and in general its behaviour are functions of study type [29], [31].

In fact, for example, if it is focussed on accuracy and computation cost, FEM is less efficient than FVM for highly non-linear flows. This because FEM is based on structural analysis, instead FVM is based on fluid dynamics context; then it seems FVM is better than FEM in CFD analysis.

However, in acoustics or wave propagation problems, FEM seems to be better [20].

So, in general, FVM performs better in terms of accuracy but in respect to FEM the cost of computation is more, then it means FEM provides acceptable approximation but lower computations.

Analyzing more in detail this case study done through COMSOL tool, this works both with multiphysics code and with CFD code.

It is based into FEM because the fluid side is expressed in FEM by data structures to work with multiphysics but, if the implementations are more efficient, the results are similar to FVM code. In general FEM is characterized by more degrees of freedom and consequently accuracy, however it is more memory intensive.

This is verified because FEM is not locally conservative and it works about the whole domain, through integration, instead FVM works about selected points. Typically, problems as solid mechanic and electromagnetic solvers are calculated with FEM. So, regarding solid mechanics this behaviour is fundamental because the configuration of solid mechanical systems is adapted to variational formulations. However, equations conservation does not follow this behaviour.

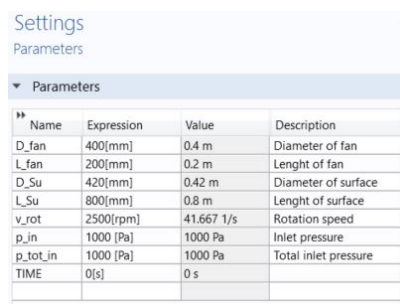
For simple flow physics, however, is not really important; in fact, FEM is more accurate than FVM with functions of linear shapes but it is more less than FDM. Furthermore, FVM solvers are optimized to solve flow problems, instead FEM are not.

2.2 Geometry Building

Discretization methods described and analyzed, this chapter is focussed on explanation of building geometry used in the COMSOL analysis. As above-mentioned, the first step of CFD calculation, called pre-processing step, is the preliminary phase of building and setting of the geometry, parameters and model.

The first step of fan model building is the indication of parameters list used in the model. This phase is fundamental because each part and element of the model are parameterized, so the geometry and the behaviour of study are not limited only for this building but they are valid for any value.

The figure 2.1 shows an example of parameterized values.



Name	Expression	Value	Description
D_fan	400[mm]	0.4 m	Diameter of fan
L_fan	200[mm]	0.2 m	Length of fan
D_Su	420[mm]	0.42 m	Diameter of surface
L_Su	800[mm]	0.8 m	Length of surface
v_rot	2500[rpm]	41.667 1/s	Rotation speed
p_in	1000 [Pa]	1000 Pa	Inlet pressure
p_tot_in	1000 [Pa]	1000 Pa	Total inlet pressure
TIME	0[s]	0 s	

Figure 2.1: Example of list of parameters of fan building.

The second step is real building of geometry; this can be divided in two sub-steps. The first, regarding fan and air guide, provides the study of fan and air guide both built and prototyped by ABB. Then, they are imported in COMSOL in the geometry building window through *import* function.

Figure 2.2 shows front, back and side respectively of ABB fan with its dimensions. Note that it is composed by 13 blades, not arranged symmetrically.

In figure 2.3, instead, different views of air guide are shown.

Finally, complete model of fan and air guide is shown at the figure 2.4. The air guide is moved through move function.

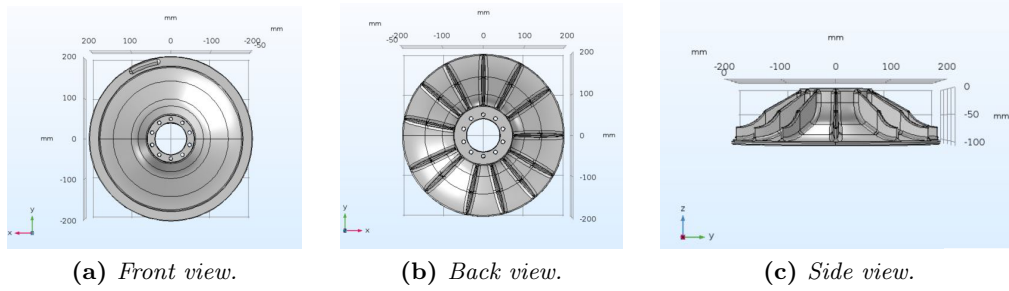


Figure 2.2: View of fan.

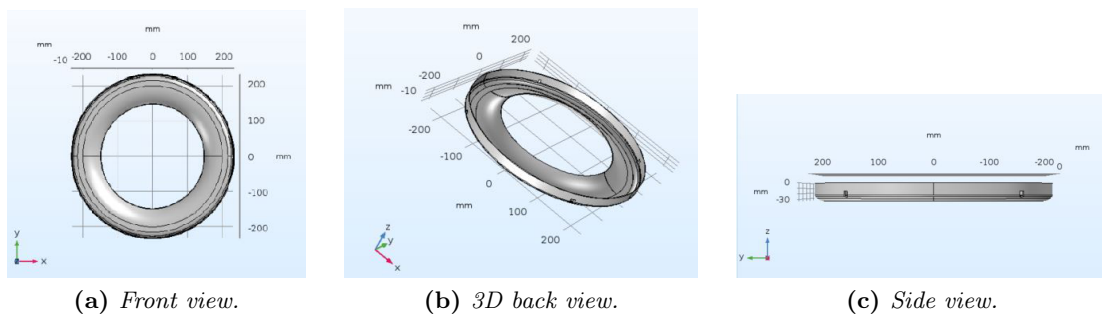


Figure 2.3: View of air guide.

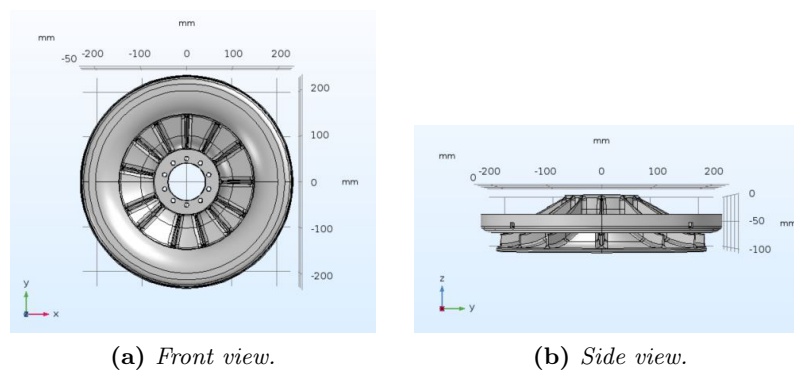


Figure 2.4: View of fan and air guide.

Another step forecasts to create the geometry through work plane in which, after that plane geometry is made, the 2D (x, y) geometry is built. Simple geometric shapes, such as circle, rectangle, Bezier polygon, etc., are used to create it. After this, using extrude function, 2D geometry is transformed in 3D (x, y, z).

Figures 2.5 and 2.6 show the details about work plane window and geometric shapes of plane geometry. Figure 2.7 shows an example of building model component, starting from a circle drawn on the plane geometry and after then it is extruded in 3D.

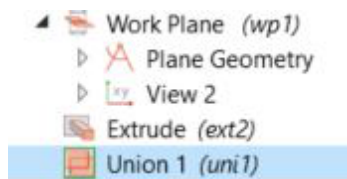


Figure 2.5: Work plane window.

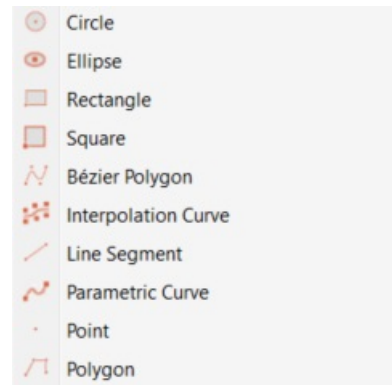
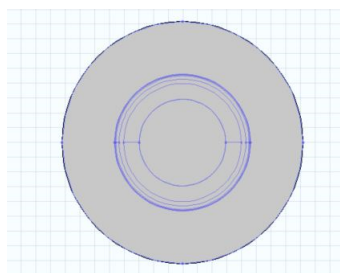
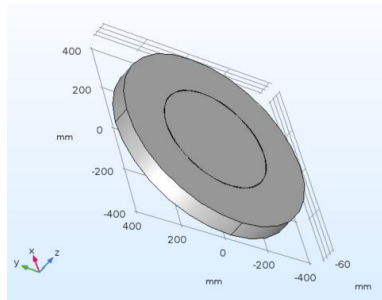


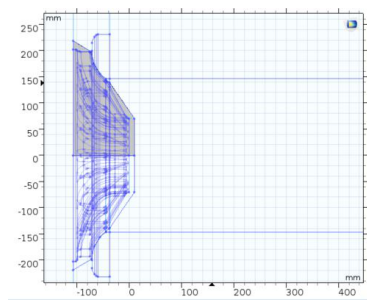
Figure 2.6: Geometrical shapes window.



(a) Circle in geometry plane.



(b) Extruded circle.



(c) Bezier polygon section.

Figure 2.7: Examples of geometry building.

Geometries parts built, they have been simplified and defeatured through defeaturing and repair function.

This is an important action to improve the mesh and to solve the calculation. In fact, each geometry is characterized by superfluous details, such as fillets or edges, that have a relevant weight in the calculation time.

Through these functions, the elements are “hidden” in the CFD calculation, involving, with an acceptable accuracy and calculation time, efficient results.

In figure 2.8 is shown defeaturing repair window and its application, instead in figure 2.9 there are examples of delete faces application with removed details.

It is possible to notice the fan details, circled in red, that are removed in right figure in respect to left picture.

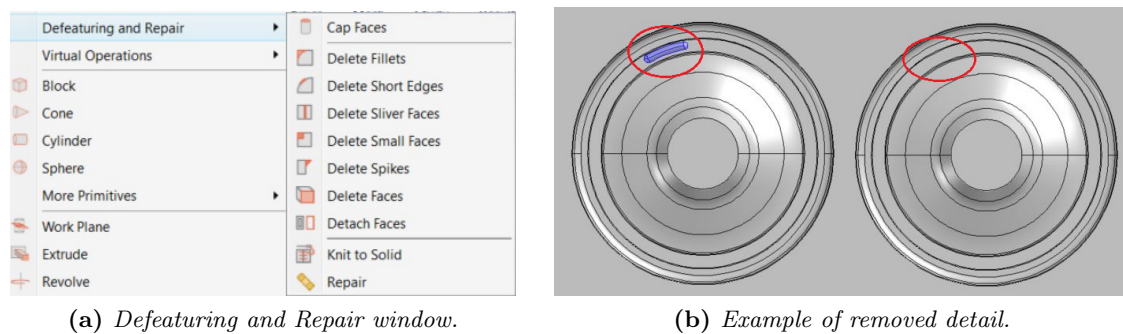


Figure 2.8: Examples of defeaturing and repair function.

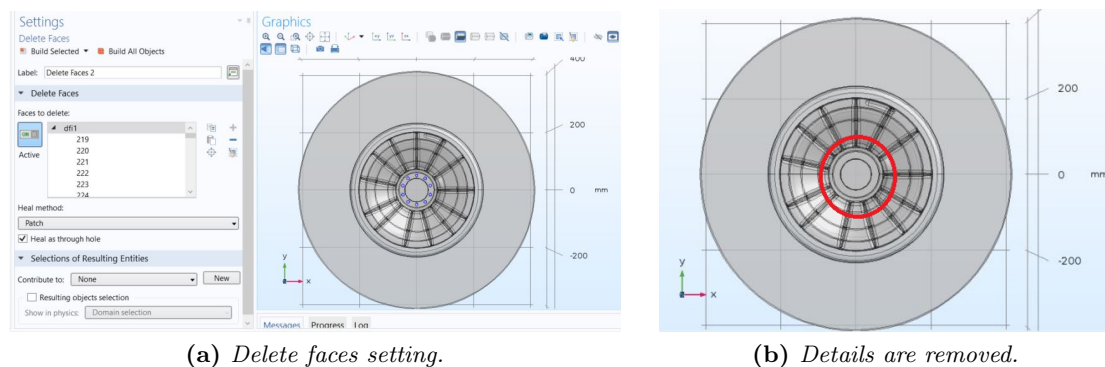


Figure 2.9: Example of delete faces function to remove details.

Other operations and improvement geometry types are discussed in chapter 2.5., when the mesh setup is analyzed.

This make, the complete geometry of fan model is then built. All the elements are assembled in entire geometry representative the complete fan model.

This can be observed into different views in figure 2.10, both through outer and inner view.

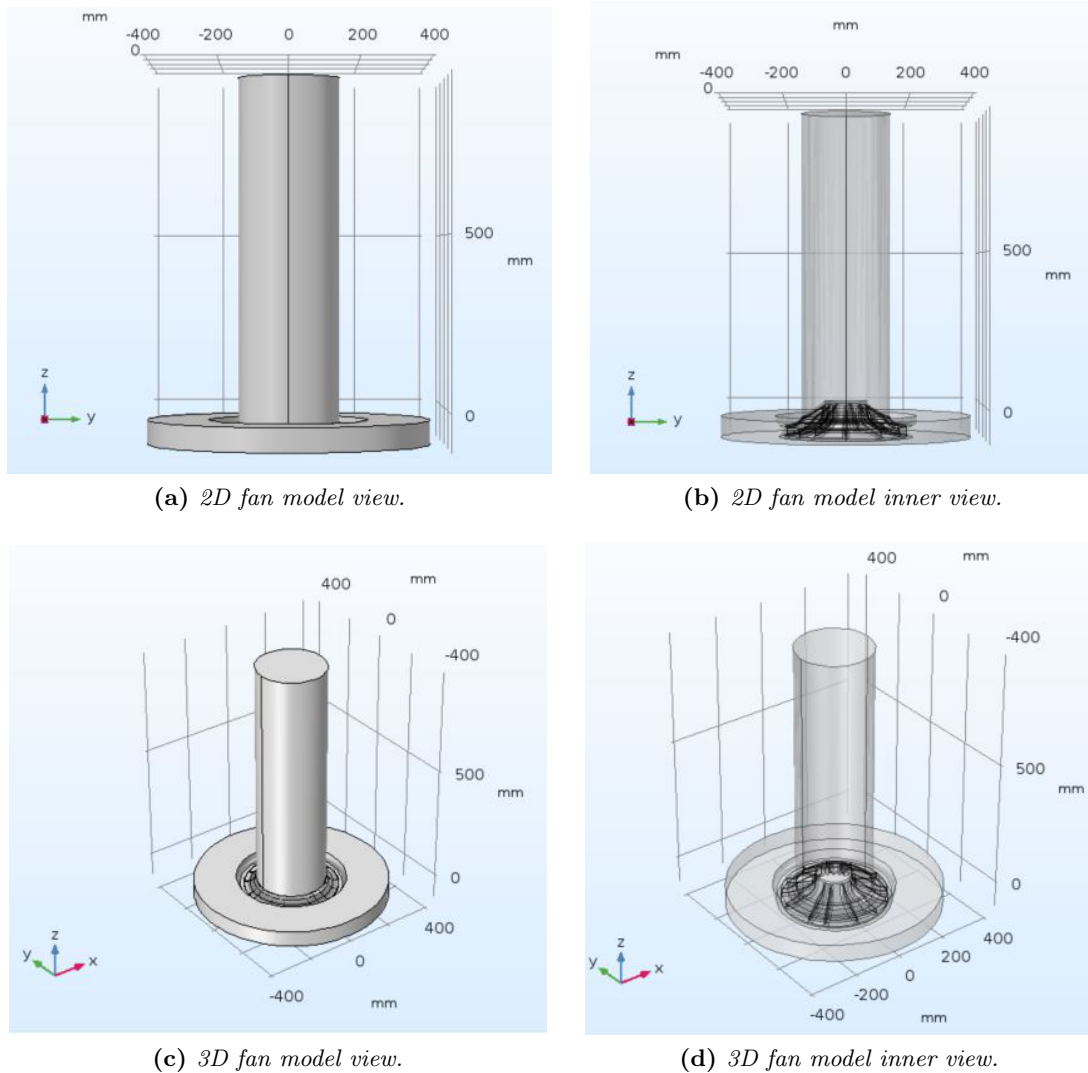


Figure 2.10: 2D (a), (c) and 3D (b), (d) outer and inner fan model view

2.3 Boundary Conditions

Geometry built, the next step consists in the boundary conditions explanation. In fact, almost every CFD problems are defined considering the limits of initial and boundary conditions.

To implement the boundary conditions, typically an extra node is added through physical boundary, in such a way that inlet conditions are assigned to the nodes just outside of the system and the physical boundaries can be coincident with the scalar control volume boundaries.

In general, the boundary conditions mean necessary constraints for the solution of a differential equations to be solved in a domain where, in its boundary, any conditions are valid. These types of problems are important because allow to model different types of phenomena and applications, such as solid mechanical or heat transfer. Typically, boundary conditions are necessary when the problem needs be solved in the space.

In COMSOL study, considering a selection where a physics feature is active, the behaviour is governed through its equations and material properties. Then, boundary conditions are applied to geometric entities which they divide this region to external. However, often, these are also applied to inner superficies into solid, especially in the case of 3D solid.

They are possible two ways to specify the boundary behaviour and two corresponding boundary condition types.

In the first, called Neumann boundary condition, flux conditions are considered to specify the behaviour of external interact with the model at the boundary. This can be expressed through an applied force, flux or current. In other words, a Neumann condition is used to prescribe a flux, then a gradient of the dependent variable [23].

In the second, called Dirichlet boundary condition, the interaction results are specified by constraints between the model and its boundaries, as expected values of the dependent variables. Through Dirichlet condition is possible to describe the variables for which the problem is solved.

Two boundary conditions types are related because in a specific model, every Neumann boundary condition (or flux condition) makes unique values of the dependent variables and every constraint requires a unique flux to makes the expected values. In the case of heat transfer, Neumann boundary condition is based on just heat transfer, instead, the Dirichlet condition on temperature. Another boundary condition is Robin boundary condition, that is a mixture of the Neumann e Dirichlet condition types, in which exists a relation between the variable and its gradient.

Boundary conditions shortly introduced, their applications in the case study is below described. As above done with building geometry, also for boundary conditions is necessary to define the variables that act to the model and how they are used, as shown in figure 2.11. After this, considering the model view shown in figure 2.12, model parts to whom are applied boundary conditions have been selected. In figure 2.12(a), wall selection is shown, instead, in 2.12(b) inlet and outlet selection.

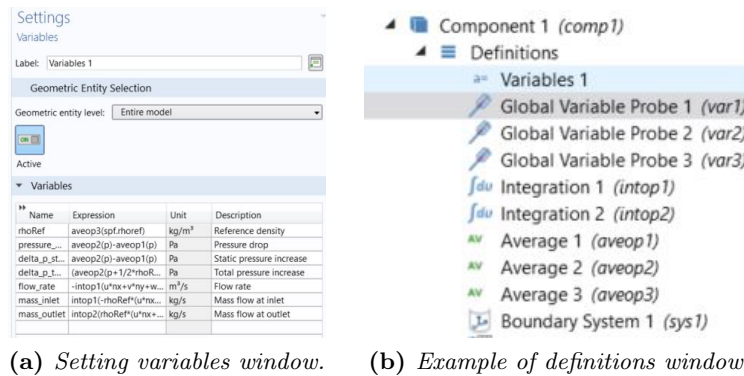


Figure 2.11: Boundary condition setting.

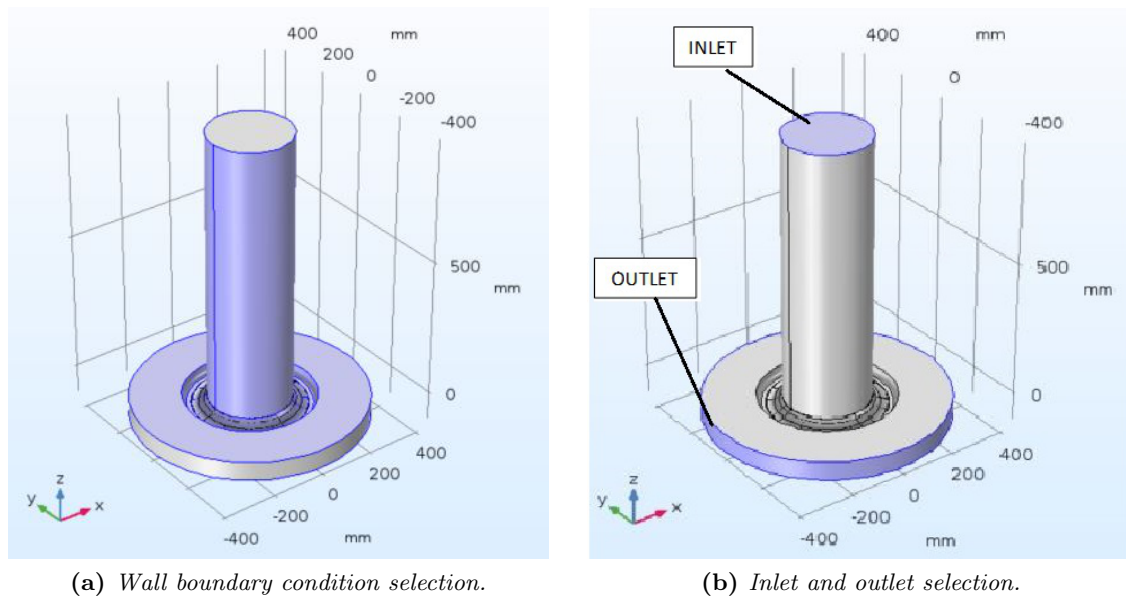


Figure 2.12: Boundary condition selection.

Referring to inlet, it requires velocity or pressure data. The first can be made through a velocity field using a velocity condition. This way is done in $inlet_1$ of the fan model. The alternative involves using the pressure component, as in $inlet_2$, in which the pressure can be specified through a stress condition. This condition requires a flow direction, which allows to have a well-posed condition.

Regarding *outlet* conditions, the common approach is to use a pressure through normal stress condition on the outlet, described to the equation $\mu \frac{\partial u_x}{\partial n} = 0$, where $\frac{\partial u_x}{\partial n}$ is the derivative of the tangential velocity field.

This introduced, in $inlet_1$ the speed equal to $U_o=0$ m/s is imposed, instead, in $inlet_2$, the pressure is used as inlet condition and it is described by function $p_tot_in-0.5*\rho Ref*aveop1(w^2)$ Pa; finally, in $outlet$ conditions pressure is equal to $P_0=0$ Pa, as below shown in figure 2.13.

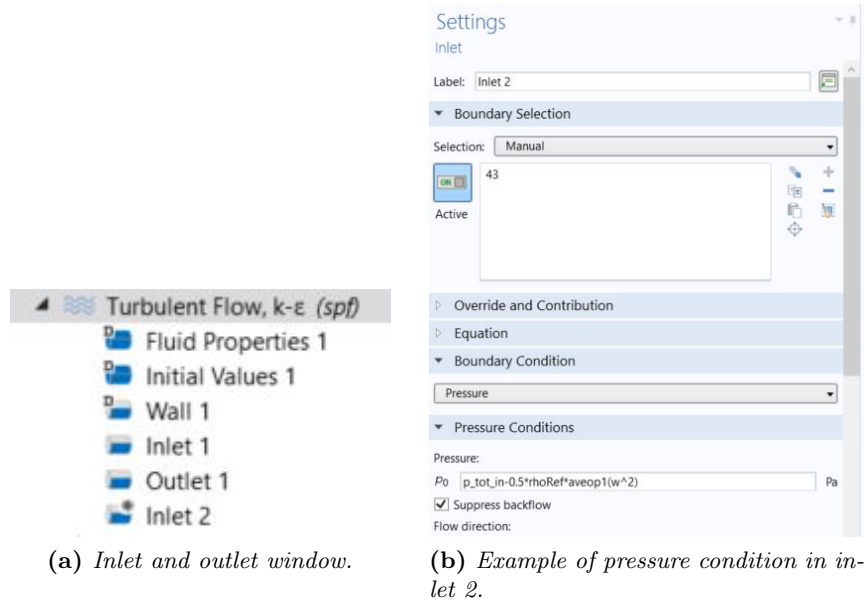


Figure 2.13: Example of boundary condition setting.

2.4 Solver Setup

As above-mentioned, the second step of each CFD analysis is the resolution of equations with iterative method. In this phase, turbulence modeling, solver and convergence requirement are defined. With turbulence means a property of the flow field that is characterized by different flow scales.

Through Reynolds number Re , it is possible to measure the propensity of an isothermal flow to become turbulent [22],[23].

$$Re = \frac{\rho UL}{\mu} \quad (2.1)$$

where μ [Pa·s] is the *dynamic viscosity*, ρ [kg/m³] the *density*, U [m/s] the *velocity* and L [m] the *length scales* of the flow.

If Re is high, the flow tends to become turbulent. To simulate turbulent flow, the Navier-Stokes equations can be used, however a large number of elements in order to represent the high number of scales in the flow are required. An alternative approach involves to divide the flow quantities into mean values and fluctuations; in this way the effect of the fluctuations is modeled through a turbulence closure.

This means that solving the model for the turbulence shutting, it can be numerically less expensive than resolving all turbulence scales. In this case study, the flow is considered *weakly compressible* and *k-ε Turbulent* model is applied.

This is a model used for turbulence models for industrial applications.

It is called *k-ε* because it uses two additional transport equations and two dependent variables, that are *turbulent kinetic energy k* and *turbulent dissipation rate ε*.

In this way, the turbulent viscosity is modeled as:

$$\mu_T = \rho C_\mu \frac{k^2}{\epsilon} \quad (2.2)$$

in which C_μ is the *model constant*.

The *k-ε* model considers different hypothesis, in which the most important is high value of Re . Furthermore, it needs to consider that the turbulence is in equilibrium in boundary layers, and that the production is equal to dissipation. However, unfortunately, these conditions are not always true and they limit the accuracy. On the other hand, in most cases, the limited accuracy is a trade-off for the computation resources that they are saved, compared to others complicated turbulence models.

This described, the next phase is to understand solver resolution used in this case study. In COMSOL, *Rotating Machinery, Laminar Flow* and *Rotating Machinery* and simple *Turbulent Flow* interfaces model the flow, in geometries with rotating elements. To describe this, the Navier-Stokes equations can be written in rotating 2.3 and non-rotating refe4 coordinate system:

$$\frac{\partial p}{\partial t} + \nabla \cdot (\rho v) = 0 \quad (2.3)$$

$$\rho \frac{\partial v}{\partial t} + \rho(v \cdot \nabla)v + 2\rho\Omega xv(\rho v) = \nabla \cdot [-\rho I + \tau] + F - \rho\left(\frac{\partial \Omega}{\partial t}xr + \Omega x(\Omega xr)\right) \quad (2.4)$$

where v is the *velocity vector*, r the *position vector* and σ the *angular velocity vector*.

The relation between velocity vector and the position vector in a stationary coordinate system is expressed as:

$$u = v + \frac{\partial r}{\partial t} \quad (2.5)$$

In COMSOL the user input for a rotating domain imposes the *angular frequency w*. So, the *angular velocity vector σ* can be calculated with *angular displacement ω*, as:

$$\frac{dr}{dt} = w \quad (2.6)$$

In this way, Ω is defined as Ω times the normalized axis of rotation. In particular, in 2D, the axis of rotation is the z direction, instead in 3D is set in the Rotating Domain features. This described, the next step consists in the presentation of Frozen Rotor solver. The Rotating Machinery acts with *frozen rotor* approach. This assumes that the flow in the rotating domain, expressed in rotating coordinate, is fully developed.

In this way the equation 2.3 can be reduced to:

$$\frac{\partial p}{\partial t} + \nabla \cdot (\rho v) = 0 \rightarrow \nabla \cdot (\rho v) = 0 \quad (2.7)$$

Frozen rotor solver is an optional setting for rotating analysis that involves reducing simulation time, producing an approximate solution. In this way, the rotating region does not rotate during the simulation. Then, this method is used to simulate in speedy way rotating elements without numerical rotation of physical rotor. This approach allows not to update the mesh position in each time step and then it is possible to use large steps that involve a steady-state in less time. Obviously, in this way, the boundary conditions remain transformed as if the domains were rotating but, instead, the domains remain fixed, just “frozen” [22], [23]. The fluid flows, as in the time-dependent case, are solved for the velocity vector in the stationary coordinate system u and not in v .

To have $\nabla \cdot (\rho v) = 0$, frozen rotor methods defines a parameter called *TIME*, imposed to 0 (it is written in parameters list), as:

$$\omega = wTIME \quad (2.8)$$

After this, the $\frac{\partial p}{\partial t} = 0$ and the mesh time derivative of the velocity is replaced by $\frac{\partial u}{\partial t} = \Omega x u$.

The frozen rotor approach is able, in particular contexts, to provide the same solution, starting to steady-state. For example, when the entire geometry is rotating or if the model is invariant in respect to position of rotating domain relative to the no-rotating domain. Typically, however, there is not steady-state solution. In alternative is possible to have a pseudo steady-state in which the solution is modified periodically around an average solution; if this is true, the frozen rotor develops an approximate solution that it is function of the position in which the rotor is frozen.

To know this rotor position, it is possible to make a parametric sweep over *TIME* parameter.

In general, anyway, frozen rotor method is valid to obtain initial values for time dependent simulations.

In fact, the above-mentioned pseudo steady-state can be reached through few revolutions in the case in which the starting point is frozen rotor solution; instead, if the starting point is $u=0$, they are necessary more revolutions.

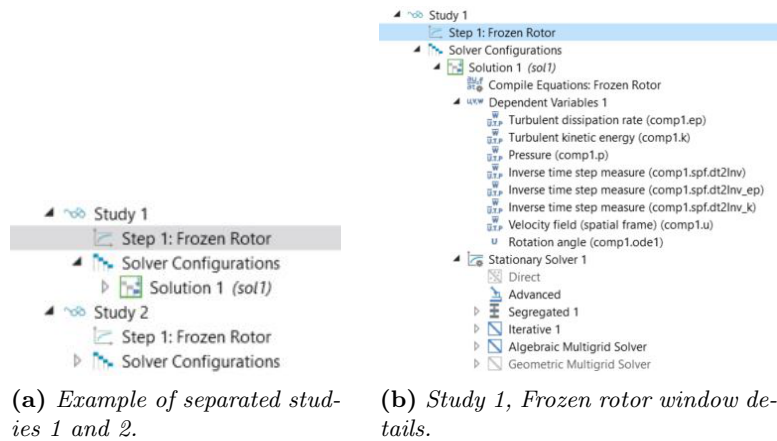
From the of setting solver point of view, Rotating Machinery interfaces work mainly with two types of geometries with rotating parts.

The first type is characterized by rotation of entire geometry, such as in individual parts in turbo machinery. In these cases, the selection for the rotating domain is done in *Definitions Node* including all domains.

The second type, instead, refers to geometries where it is possible to divide the modelled component into rotationally invariant geometries.

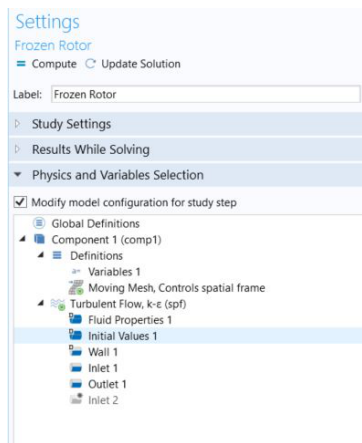
After this, needs to create a geometry using separate domains for fixed and rotating parts. Then, the following step consists to remove non rotating domains from the rotating domain selection.

In the fan case study, as above-mentioned, have been created two studies 2.14; the first, considering in $inlet_1$ the parameter velocity u_0 and the second considering instead in $inlet_2$ the pressure $p_{tot_in} - 0.5 * \rho_{Ref} * v_{ref}^2 (w \wedge 2)$.

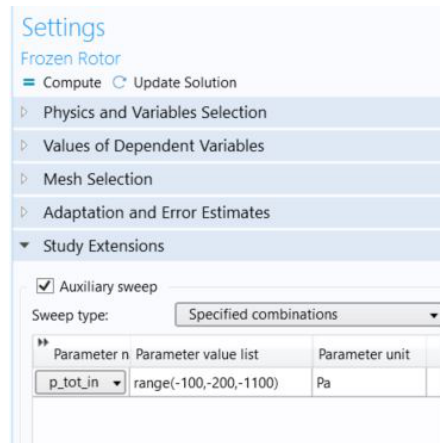


(a) Example of separated studies 1 and 2.

(b) Study 1, Frozen rotor window details.



(c) Study 1, example of frozen rotor setting.



(d) Study 2, pressure range setting.

Figure 2.14: Solver setting.

However, two studies are not separated from each other. In fact, Study 2 calculates refer to Study 1 results. Starting from this, the second study works results with different values of total pressure in inlet, as shown in figure 2.2(c). This is done in the Study Extensions window of Frozen Rotor - Study 2, as shown in figure 2.14(d). As showed in section 2.5, results changing with different pressure values and different rotation speed.

2.5 Mesh Setup

The next step before to solve the model, consists of study and analysis the mesh setup. The quality of CFD model is often determined by quality of the used mesh to solve the problem. In fact, a good mesh simplifies the convergence, it reduces computational requirements and makes accurate solutions. To create a good mesh, exist two important laws; the first involves there must not be empty regions in the computational domain and the second asserts there must not be overlapping mesh elements. COMSOL is able to guarantee, through automatic controls, the violation of above-mentioned laws [22], [23].

Other aspects need to consider about creating good mesh are the high quality, sufficient resolution for the desired accuracy and low computational cost. To have a high quality of mesh element, it is important that it is as isotropic as possible. It is possible to use different quality measures to quantify the quality of elements. If a generic element has quality equal 1, it is perfect; any element that deviates from its perfect form has then quality less than one. In the case that an element collapses or inverts, its area or volume becomes zero. Then, it is important to solve it and to modify the mesh to eliminate them because they generate equation systems that are hard to solve. The worst way to deform a mesh element is to skew it. In this case, angles element deviates from 90° . This involves a negative impact both on the local accuracy calculation and on high number of system conditions.

To understand the mesh quality, *growth rate* can be used. It represents the change in element size from one element to one of its neighbours; obviously it should be small to have accurate results.

Typically, structured meshes and free unstructured tetrahedral meshes have high growth rates. To have a sufficient resolution in a CFD problem it is important to anticipate sharp gradients because probably they are in such a way to create locally finer mesh only in particular points. Sharp gradients in the flow and pressure fields require a locally dense mesh to solve them.

Obviously is possible to make a mesh that it is very dense everywhere; however, the computational cost is very relevant. Then, it is important to only act in regions where the mesh is required by flow and to provide a good transition to regions in which also larger elements are a good compromise.

This considered, typically, the CFD mesh has regions with structured mesh and regions with free unstructured mesh as shown in fig. 2.15.

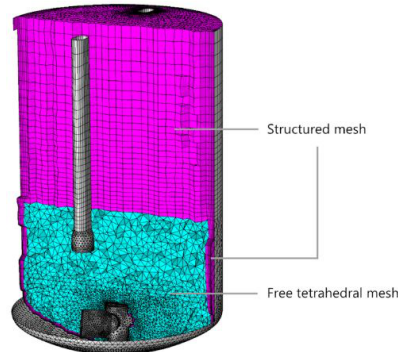


Figure 2.15: Example of elements with structured and free tetrahedral mesh.

Another shortly question regards the different element types using for the mesh and their different behaviour. Typically, tetrahedral elements are predefined element type used in COMSOL.

These methods can be valid for any 3D volumes, without to consider shapes or topologies. Other types of elements (bricks, prisms and pyramids) can be used only when it is necessary. In fact, these elements cannot always create to mesh a particular geometry, but it is necessary an user input. However, the main motivation to use these elements is in their possibility to reduce number of mesh elements.

In fact, they can have very high aspect ratios, instead, the algorithm to create a tetrahedral mesh is characterized by proportional ratio about equal to 1. So, when the solution varies gradually in certain directions or when the accuracy in particular regions is not relevant, it is possible use other elements over tetrahedral. In figure 2.16, different 3D elements examples are shown; in particular are tetrahedra, bricks, prisms and pyramids respectively.

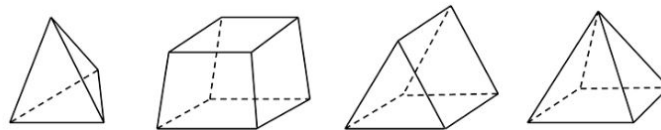


Figure 2.16: Example of 3D elements and free tetrahedral mesh.

As anticipated in chapter 2.2, other aspects that have importance and influence on computational cost are represented by any geometries built parts. So, it is extremely significant to create correctly the geometry.

It is possible to know how will be the solution, so that the mesh can be refined where necessary and maintained coarse where the solution accuracy is reasonable.

A good action consists, for example, to create a symmetric geometry, when it is possible; in this way, the symmetry plane removes about 50% of the elements and reduces the computational time without loss of accuracy.

Beyond this action, in the geometry are often included elements and details to whom CFD analysis is not interested, such as springs, bolts, etc; then, these details, can be replaced or removed. Furthermore, CAD geometry parts also tend not to fit perfectly.

In this case, mesh elements need to conform with them, developing results in a very dense mesh around the sliver faces. These are much smaller than the smallest allowed element size, so these elements tend to have high anisotropic and high skewness.

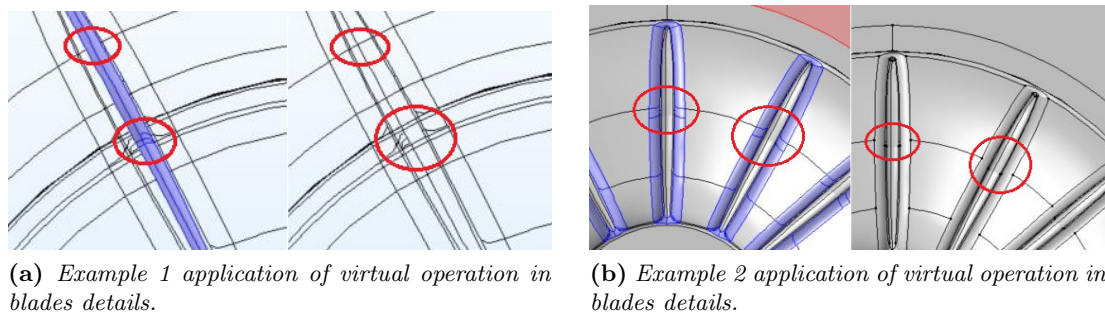


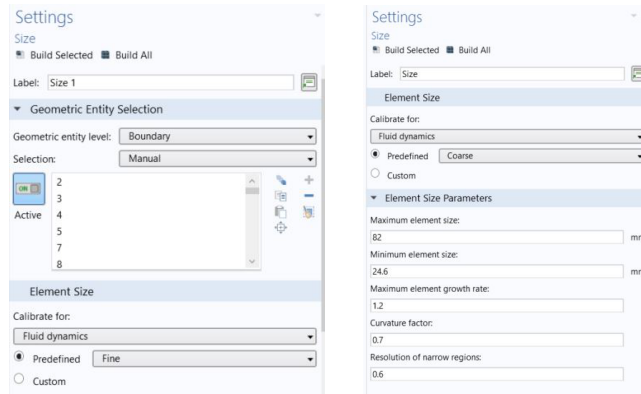
Figure 2.17: Virtual operation example.

In this way unnecessarily dense meshes are produced even with low quality, therefore they should be removed. In COMSOL, this operation can be done through *Virtual Operation* function, however, it is necessary to pay attention because using these operations, surface meshes can be changed, that it modifies the characteristics of the flow. In the fan case study virtual operations have been used to improve the geometry to make the mesh. An example of application of virtual operation is shown in figure 2.17 where, through *Form Composite Faces* and *Form Composite Domains*, the geometry is more adapted. In the right figure, is possible to observe the removed detail circled in red after virtual operation application.

This described, the mesh used in the fan model is based on *User-controlled mesh* about sequence type but it is characterized to two size; the first size, calibrate for fluid dynamics is a coarse mesh, with element size parameters observable shown in figure 48. The second, *size 1*, is used for the boundaries, so these have been chosen from boundary lists. In this case the element size is also calibrated for fluid dynamics, but it is a fine mesh and therefore the element size parameters are also changed than first size, as shown in figure 2.18.

To conclude this section, in respect to the above presented, figure 2.18 shows mesh view of the model.

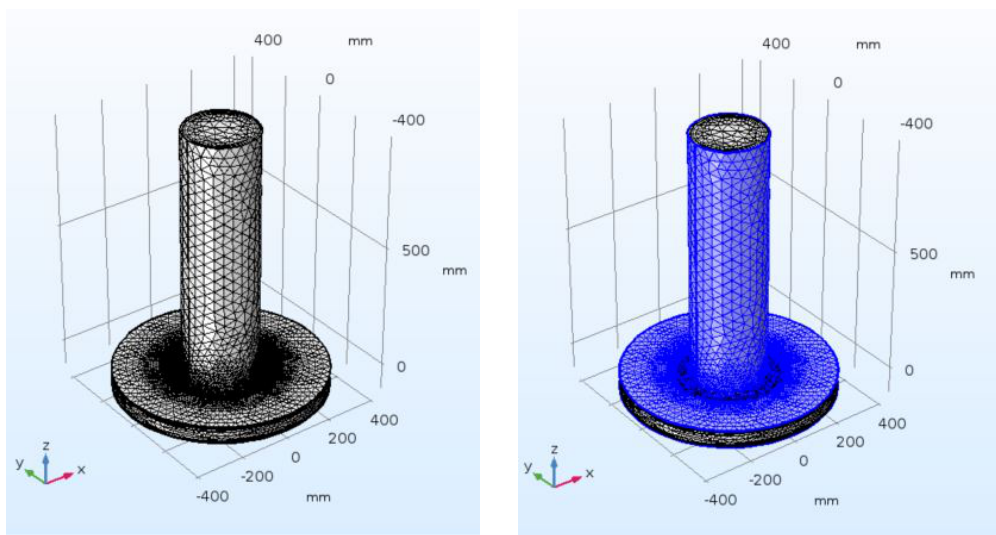
In particular, in the fig. 2.19(a) is possible to observe in detail three different mesh types applied in the fan.



(a) Setting window of mesh size 1.

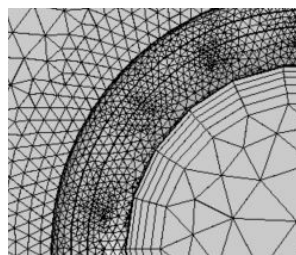
(b) Setting window of mesh size.

Figure 2.18: Mesh setting.



(a) View of total fan mesh.

(b) View of wall mesh.



(c) Details of different mesh in fan.

Figure 2.19: Mesh results.

2.6 Fluid Velocity Results

The final third step of CFD calculation is the post-processing phase where results are analyzed and discussed. Before to discuss the fluid velocity results obtained by simulations, it is also important to shortly present how results are developed in COMSOL. The results branch in COMSOL have tools for post processing and analysing the results that are *visualizations, data analysis, reports*. During results analysis and visualization, it is possible to divide main operation types, that are *Data Sets, Derived Values and Tables, Plot Groups and Plots*. To post-process the results, all these functions are used.

In the first, the source of data for plotting are provided. In the second, derived values define the evaluation of integrals, providing maximum and minimum values, values of variables in points and values of global variables. These results are stored in *Table Nodes* and are showed in the *Table Window*. The last window includes Plots and Plot Groups; in this case, a plot group means a collection of plots to show at the same time in the *Graphics Window*.

This said, results that are analyzed concern pressure and velocity behaviour of the fluid. To learn, means the amount of force applied perpendicular to the surface of an object per unit area over which that force is distributed [33]. The equation can be described as:

$$P = \frac{F}{A} \quad (2.9)$$

where P is the *pressure*, F [N] is the *force*, A [m²] is the *surface*. The main pressure units used are *psi* (pounds per square), *Pa* (Pascal), *atm* (atmosphere), *bar*. Starting from this, needs to divide different pressure types: *total pressure, dynamic pressure* and *static pressure*. Total pressure means the force per unit area when a fluid becomes in a rest period. This is equal to summarize of dynamic pressure and static pressure as shown:

$$P_{tot} = P_{st} + P_{dy} \quad (2.10)$$

Dynamic pressure represents the difference between the total and static pressure, as kinetic energy of the flowing fluid. This is a function of the fluid velocity and density, so that:

$$P_{dy} = \rho \frac{v^2}{2g} \quad (2.11)$$

where ρ [kg/m³] is the *density*, v [m/s] the *velocity* and g [m/s²] the *gravity*. Finally, the static pressure is the pressure when fluid is in rest period or when its measurement is done traveling along with the fluid flow. This represents the force on a fluid particle from all directions. Typically, been static pressure the pressure commonly measured, the generic term “pressure” indicates the static pressure.

This said, before to discuss results, another important concept is the *volumetric flow rate* or *volume flow rate*.

This means the volume of fluid flowing per unit time. The SI unit is m^3/s , where V is the volume of fluid and t is the time, and relative equation is:

$$Q_v = \dot{V} = \lim_{\Delta t \rightarrow 0} \frac{\Delta V}{\Delta t} = \frac{dV}{dt} \quad (2.12)$$

Another representation of volume flow rate can be obtained through the velocity of the fluid v and the cross-sectional vector surface A , that is:

$$Q_v = v \cdot A \quad (2.13)$$

These relationships are useful to read the fan characteristics. In particular the more important relationship is represented, for a constant rotation speed, by ratio between pressure increase, expressed through total pressure or static pressure, and volume flow rate.

The fan curve, expressed by pressure-volume characteristic, is obtained by data points plotted graphically for a constant speed. This curve is the basis for each airflow and pressure calculations; in fact, for an exact point of static pressure there is a corresponding volume flow rate corresponding at an exact rotation speed. The results, presented and discussed below, show just this characteristic for three different calculation with three constant rotation speeds.

I. Rotation speed results at 2500 rpm

Setting conditions:

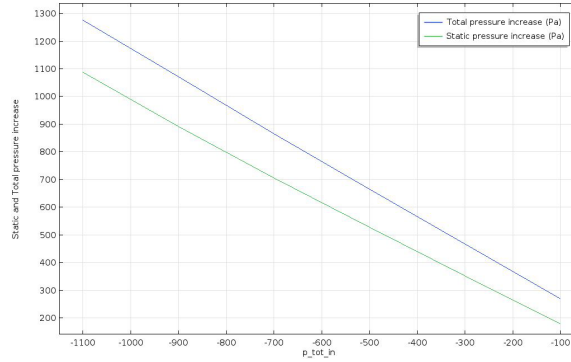
- *Inlet*₁ fluid velocity equal to $U_0=0.1$ m/s;
- *Outlet*₁ pressure equal to $p_0=0$ Pa;
- *Inlet*₂ $p_{\text{tot_in}}-0.5 \cdot \rho_{\text{Ref}} \cdot v_{\text{aveop1}}^2$ Pa;
- Pressure values of $p_{\text{tot_in}}$ in the range [-100, -300, -500, -700, -900, -1100] Pa;
- Fan rotation speed $v_{\text{rot1}} = 2500$ rpm.

The first calculation results obtained are reported in table 2.2 where, in function of $p_{\text{tot_in}}$ values, there are *Flow Rate* [m^3/s], *Static pressure increase* [Pa], and *Total pressure increase* [Pa] respectively. Furthermore, for each simulation, the calculation time is reported.

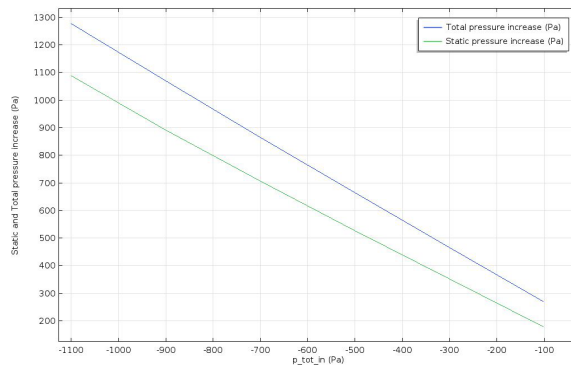
Analyzing the table it is possible to deduce that for a decrease of the p_{tot_in} , Static and Total pressure increase, while Flow rate decreases. Same results are also observable, in figure 2.20, through fan curves above-mentioned, where Static and Total pressure increase are shown in function of Flow rate and of p_{tot_in} respectively.

p_{tot_in} [Pa]	Flow Rate [m^3/s]	Static pressure increase [Pa]	Total pressure increase [Pa]
-100.00	1.2000	179.19	269.20
-300.00	1.0896	353.48	467.08
-500.00	0.9713	528.32	665.62
-700.00	0.8497	707.31	866.85
-900.00	0.7188	892.12	1071.8
-1100.00	0.5554	1088.7	1277.7

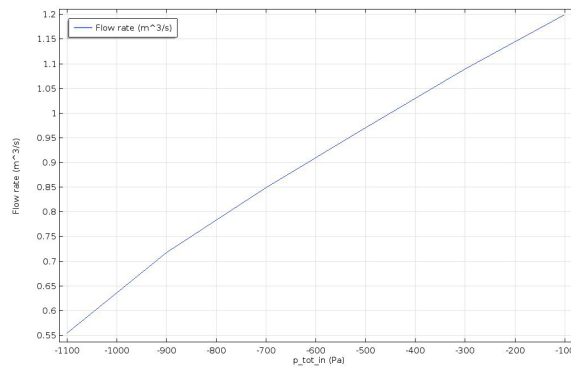
Table 2.2: Simulation results at 2500 rpm - Computation time: Study 1: 2h 52min, Study 2: 5h 25min.



(a) Static and total pressure increase in function of flow rate.



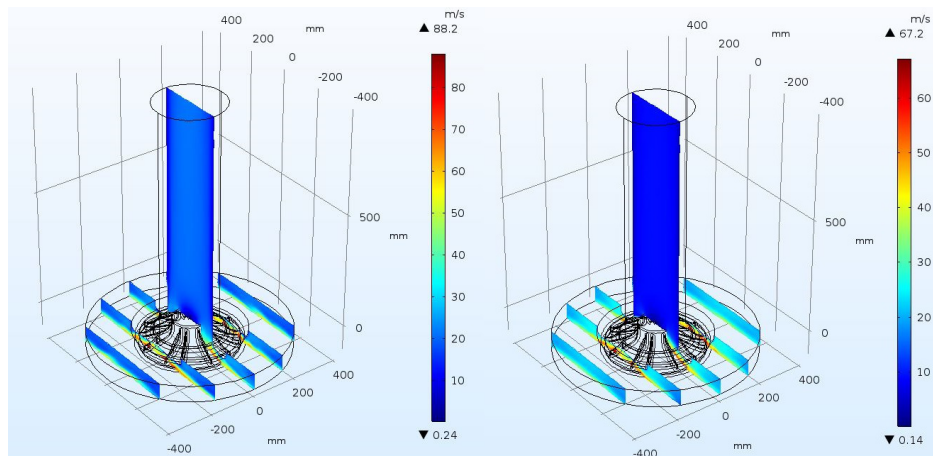
(b) Static and total pressure increase in function of p_{tot_in} .



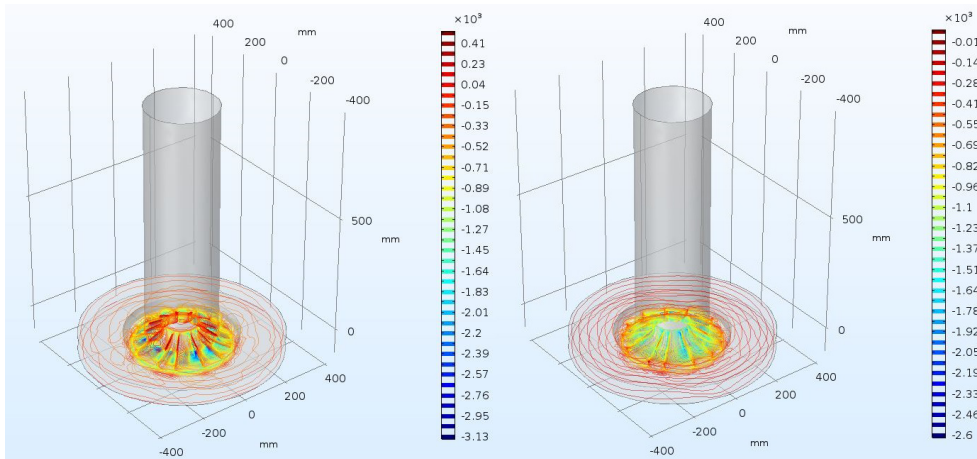
(c) Flow rate increase in function of p_{tot_in} .

Figure 2.20: Pressure and flow rate trends at $v_{rot1} = 2500$ rpm.

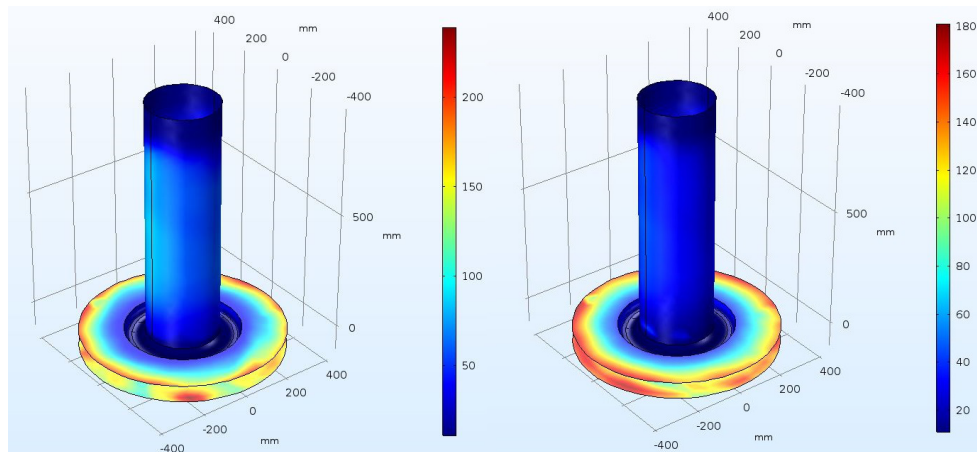
Finally, the velocity, pressure and wall resolution behaviours are graphically shown in the fan model structure in figure 2.21(a), (b) and (c), through different colours (red=high, blue=low), in function of value of $p_{tot_in} = -100$ Pa (left) and $p_{tot_in} = -1100$ Pa (right).



(a) Velocity behaviour.



(b) Pressure behaviour.



(c) Wall resolution behaviour.

Figure 2.21: Graphics results for $p_{\text{tot_in}} = -100$ Pa and -1100 Pa at $v_{\text{rot}_1} = 2500$ rpm.

II. Rotation speed results at 1500 rpm

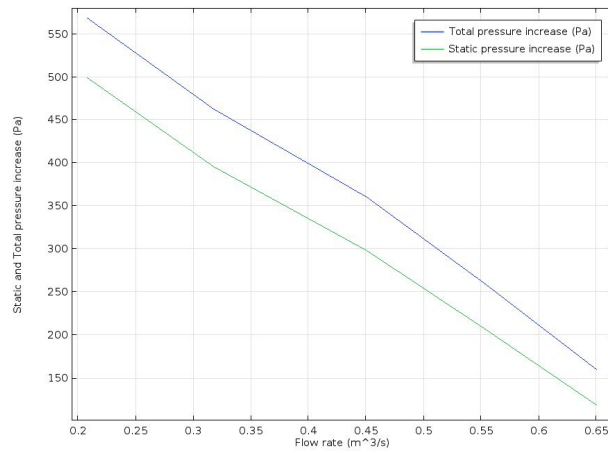
Setting conditions:

- *Inlet*₁ fluid velocity equal to $U_0=0.1$ m/s;
- *Outlet*₁ pressure equal to $p=0$ Pa;
- *Inlet*₂ $p_{\text{tot_in}}-0.5*\rho_{\text{Ref}}*v_{\text{aveop1}}(w\wedge 2)$ Pa
- Pressure values of $p_{\text{tot_in}}$ in the range [-100, -200, -300, -400, -500] Pa;
- Fan rotation speed $v_{\text{rot1}} = 1500$ rpm

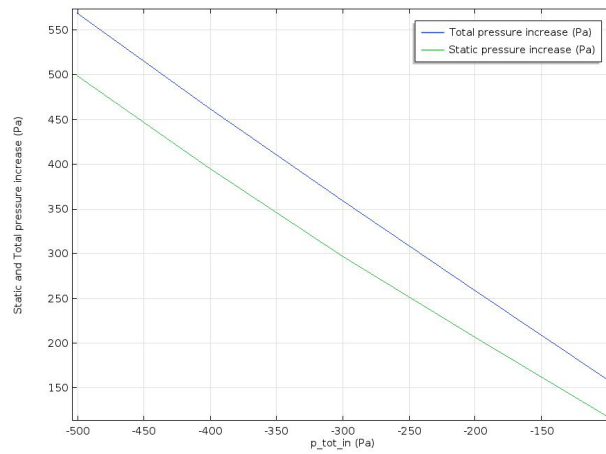
The second obtained results are reported in similar way to the first case v_{rot1} , with results in table 2.3, fan curve characteristics in figure 2.22 and velocity, pressure and wall resolution behaviours in figures 2.23.

p_tot_in [Pa]	Flow Rate [m ³ /s]	Static pressure increase [Pa]	Total pressure increase [Pa]
-100.00	0.6509	118.03	159.08
-200.00	0.5541	206.46	258.65
-300.00	0.4507	297.88	360.10
-400.00	0.3178	395.99	462.81
-500.00	0.2083	400.07	568.98

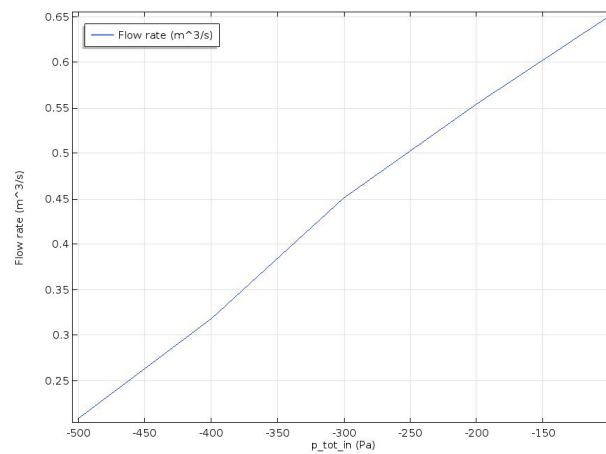
Table 2.3: Simulation results at 1500 rpm - Computation time: Study 1: 3h 27min, Study 2: 5h 25min.



(a) Static and total pressure increase in function of flow rate.



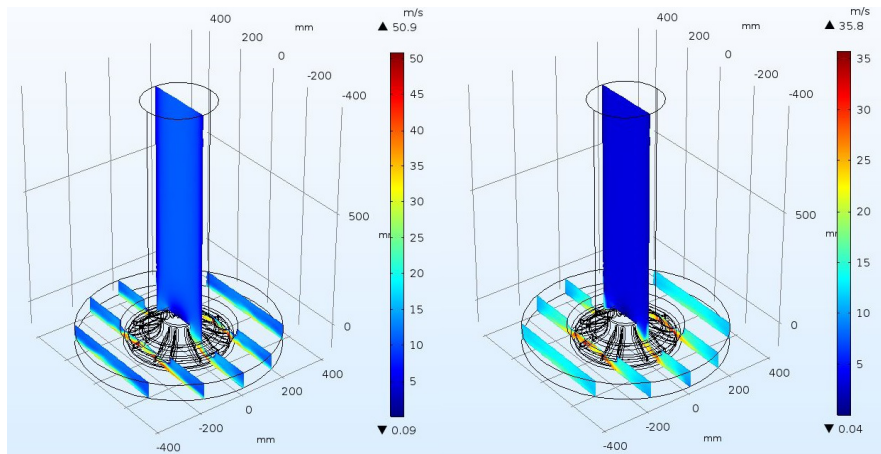
(b) Static and total pressure increase in function of $p_{tot.in}$.



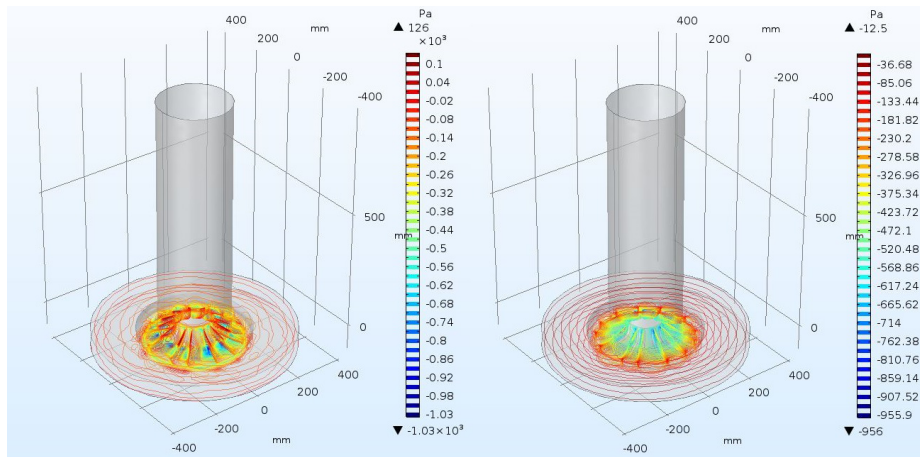
(c) Flow rate increase in function of $p_{tot.in}$.

Figure 2.22: Pressure and flow rate trends at $v_{rot1} = 1500$ rpm.

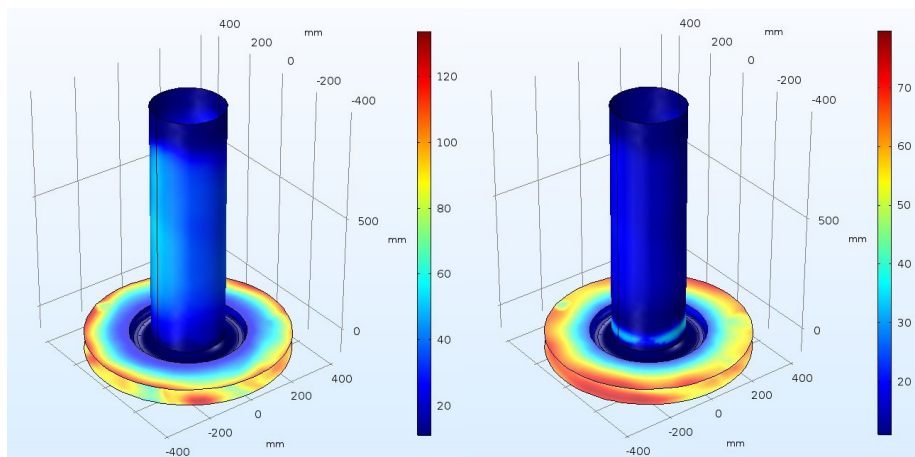
2.6. FLUID VELOCITY RESULTS



(a) *Velocity behaviour.*



(b) *Pressure behaviour.*



(c) *Wall resolution behaviour.*

Figure 2.23: Graphics results for $p_{\text{tot.in}} = -100$ Pa and -500 Pa at $v_{\text{rot1}} = 1500$ rpm.

III. Rotation speed results at 2000 rpm

Setting conditions:

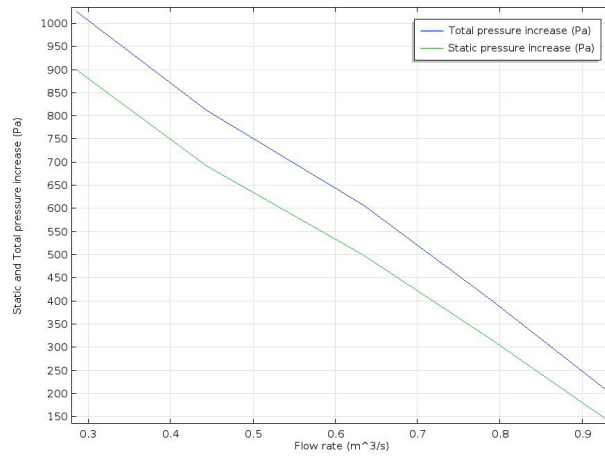
- *Inlet*₁ fluid velocity equal to $U_0=0.1$ m/s;
- *Outlet*₁ pressure equal to $p=0$ Pa;
- *Inlet*₂ $p_{\text{tot_in}}-0.5*\rho_{\text{Ref}}*\text{aveop1}(w\wedge 2)$ Pa
- Pressure values of $p_{\text{tot_in}}$ in the range [-100, -300, -500, -700, -900] Pa;
- Fan rotation speed $v_{\text{rot}_1} = 2000$ rpm

The results are reported following the same logic; table 2.4 includes numerical values, instead figure 2.24 shows the fan curve characteristics and in 2.25 the graphically behaviour of the model is indicated as a function of velocity, pressure and wall resolution.

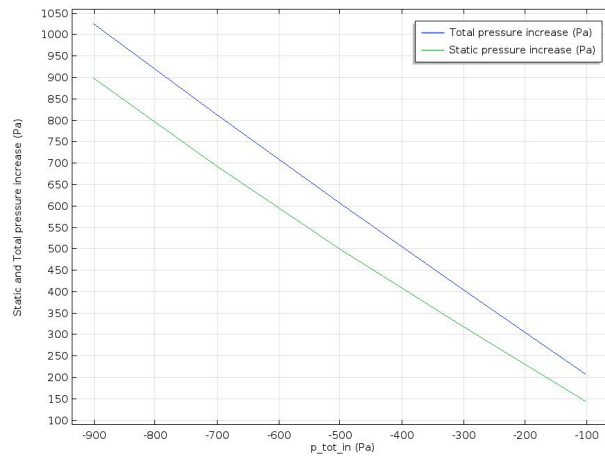
p_tot_in [Pa]	Flow Rate [m ³ /s]	Static pressure increase [Pa]	Total pressure increase [Pa]
-100.00	0.9294	144.10	206.96
-300.00	0.7871	319.21	405.19
-500.00	0.6343	499.47	607.04
-700.00	0.4435	692.55	812.63
-900.00	0.2864	899.91	1025.6

Table 2.4: Simulation results at 2000 rpm - Computation time: Study 1: 2h 46min, Study 2: 5h 25min.

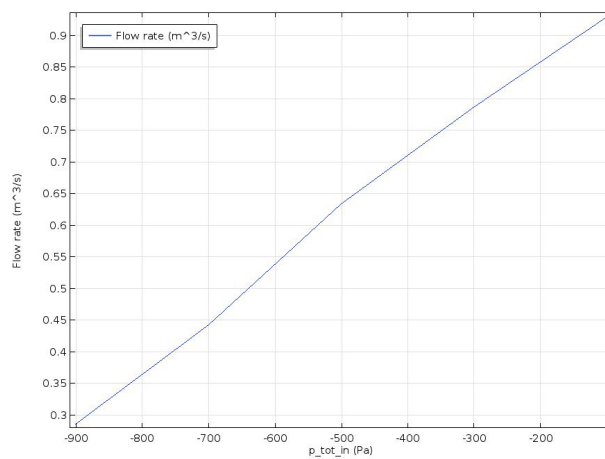
2.6. FLUID VELOCITY RESULTS



(a) Static and total pressure increase in function of flow rate.

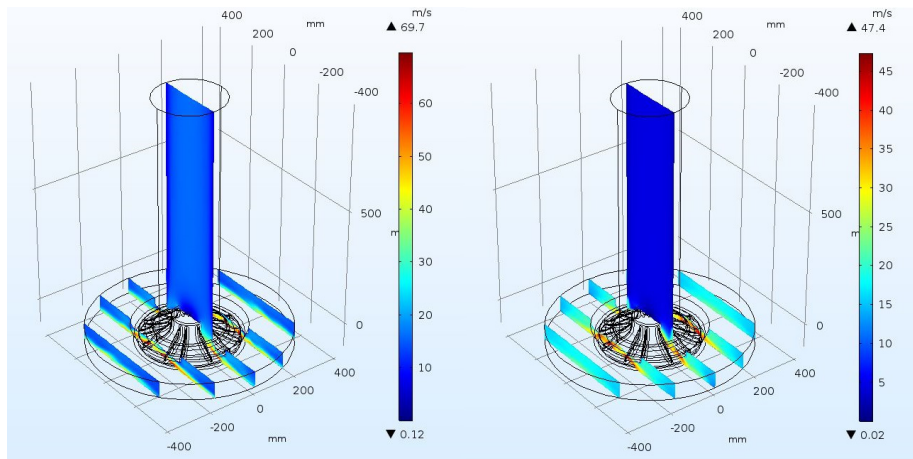


(b) Static and total pressure increase in function of $p_{tot.in}$.

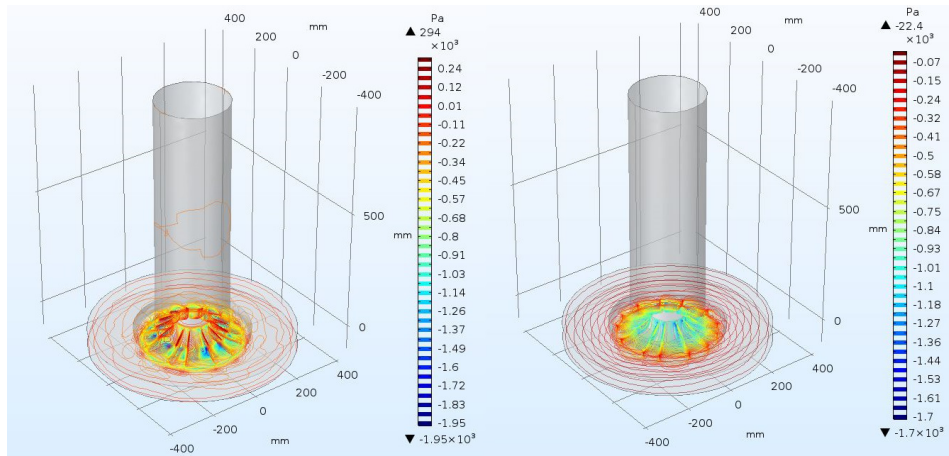


(c) Flow rate increase in function of $p_{tot.in}$.

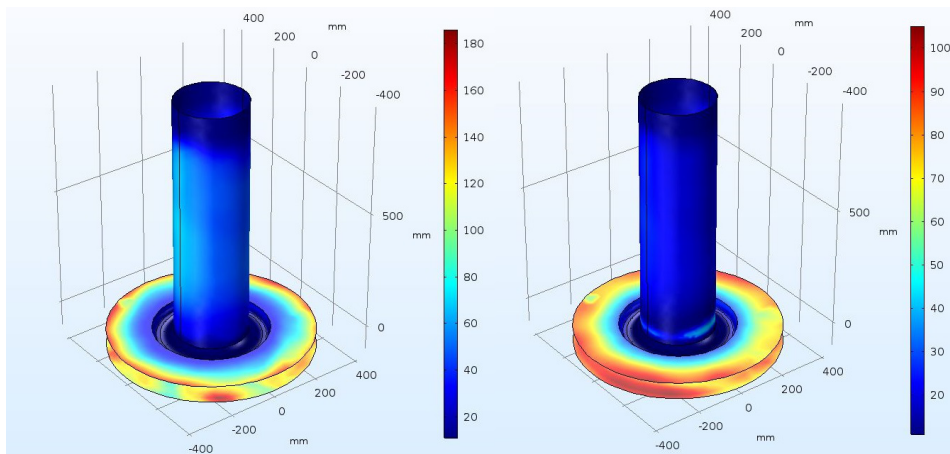
Figure 2.24: Pressure and flow rate trends at $v_{rot1}=2000$ rpm.



(a) Velocity behaviour.



(b) Pressure behaviour.



(c) Wall resolution behaviour.

Figure 2.25: Graphics results for $p_{tot.in} = -100$ Pa and -500 Pa at $v_{rot1} = 2000$ rpm.

Chapter 3

CFD Modeling of Traction Motors

Subsequently to the presentation about numerical modeling of cooling flow, in this chapter an approach to estimate the air flow of the electrical machines case study is presented. The linearity of the air flow is an important result that has been reached and analyzed. Subsequently, the air speed results will exploit as input data to develop the final thermal model.

3.1 Introduction

In the second chapter a presentation about the developed numerical fan model in COMSOL has been discussed. In view of the above, the same similar steps to develop the CFD model of the electrical motor are considered. In particular, the CFD air speed results discussed in this section are used to estimate cooling flow distribution in different parts of the motor and subsequently to estimate hot-spot temperature in the solid parts.

An important aspect that is discussed concerns the computation time. Typically, the standard CFD computation time for the air-cooled motors used in railway and e-mobility applications is characterized by hour to days per rotational speed but in this case study it has been significantly reduced. Consequently, every second saving in calculation time, results in hour of saving when running the motor in duty cycles.

To obtain an efficient developed CFD calculation and then an efficient thermal method, the functions used in numerical models are chosen to aim the minimum possible calculation time and with the purpose to keep a good accuracy. Considering the cooling system structure, the air speed has been analyzed in different motor parts, in particular in inlet and outlet, to accurately calculate the flow distribution. To achieve this, rotation of rotor, shaft, and fan have been taken in account [2]. The flow paths inside the machine in stator ducts, rotor ducts and air gap have been considered.

The velocity results are then used to calculate the local heat transfer coefficient, as it will be explained in chapter 4. Selection of the functions together with an optimization work of mesh quality and solver have been implemented.

Firstly, the CFD model is run without heat transfer function and replacing the air by boundary condition assuming flow direction normal from inlet to outlet.

The different flow speed results have been calculated only considering two motor rotation speed values, 1000 and 2500 rpm, and with a temperature equal to 20°C.

The possibility to consider only two speeds for CFD calculations has been possible through the achieved flow velocity behaviour linearity in order to derive the air flow equations to obtain the data input for the thermal model. In particular, as discuss in section 3.4, this outcome represents a big improvement because, exploiting the behaviour linearity, the air flow knowledge will be not got to run for each rotation velocity.

From technical point of view, to obtain this aim the transient sliding mesh function has been replaced by the frozen rotor function, similarly to chapter 2 previously discussed. This choice has been done because the first study was characterized by high time consuming [23].

Furthermore, significant optimization operations to improve the mesh and the solver have been executed. Additionally, velocity flow equations are derived with a limited number of calculation points with the purpose to eliminate the need for running CFD calculation together with thermal model in duty cycles.

Finally, it is important assert that, due to the weight of CFD calculations, for these results, the simulations have been executed using and comparing an ABB workstation laptop characterized by 32 Gb-RAM and 16 cores CPU and a standard laptop with 16 Gb-RAM and 8 cores CPU.

3.2 Model Building and Setting

As above-mentioned, a presentation about geometry building, frozen rotor function, mesh types and qualities are here discussed. The building of the motor geometry in similar way to explained steps in chapter 2 has been achieved.

The first step of geometry building is the setting of parameters list used in the model. This action has a relevant role because each element of the model can be also valid for another generic model. The complete model is built considering fan and air guide prototyped by ABB and the elements built by me in collaboration with Dr.-Ing. Shafigh Nategh and COMSOL team.

In this case, considering the geometry complexity, the parameters have been divided in lists, e.g. stator and winding, rotor and squirrel cage, housing, edge, shaft, others.

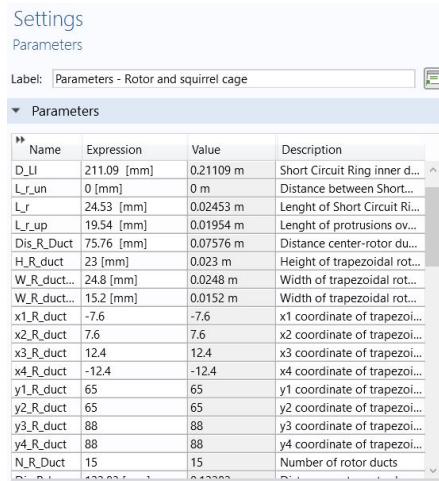
In figure 3.1 is shown an example of rotor parameterization.

Considering the geometry point of view, the motor has been built through 2D (x, y) geometries in the work plane and after extruding them in 3D (x, y, z). After that geometry is built, it is important to simplify it using functions such as *defeaturing* and *repair*. In this way, superfluous details for the meshing have been hidden. Finally, another relevant concerns the creation of *rotating volumes*.

In order to represent the air volume flow in the motor, a fictitious cylinder of air around the stator has been built.

This part is more important because is linked to the frozen rotor function and the study accuracy is dependent by this.

Then, the complete motor model in an entire geometry is assembled as shown in figure 3.2 considering 2D and 3D view.



Name	Expression	Value	Description
D_LI	211.09 [mm]	0.21109 m	Short Circuit Ring inner d...
L_r_un	0 [mm]	0 m	Distance between Short...
L_r	24.53 [mm]	0.02453 m	Lenght of Short Circuit Ri...
L_r_up	19.54 [mm]	0.01954 m	Lenght of protrusions ov...
Dis_R_Duct	75.76 [mm]	0.07576 m	Distance center-rotor du...
H_R_duct	23 [mm]	0.023 m	Height of trapezoidal rot...
W_R_duct...	24.8 [mm]	0.0248 m	Width of trapezoidal rot...
W_R_duct...	15.2 [mm]	0.0152 m	Width of trapezoidal rot...
x1_R_duct	-7.6	-7.6	x1 coordinate of trapezoi...
x2_R_duct	7.6	7.6	x2 coordinate of trapezoi...
x3_R_duct	12.4	12.4	x3 coordinate of trapezoi...
x4_R_duct	-12.4	-12.4	x4 coordinate of trapezoi...
y1_R_duct	65	65	y1 coordinate of trapezoi...
y2_R_duct	65	65	y2 coordinate of trapezoi...
y3_R_duct	88	88	y3 coordinate of trapezoi...
y4_R_duct	88	88	y4 coordinate of trapezoi...
N_R_Duct	15	15	Number of rotor ducts

Figure 3.1: Example of rotor parameters.

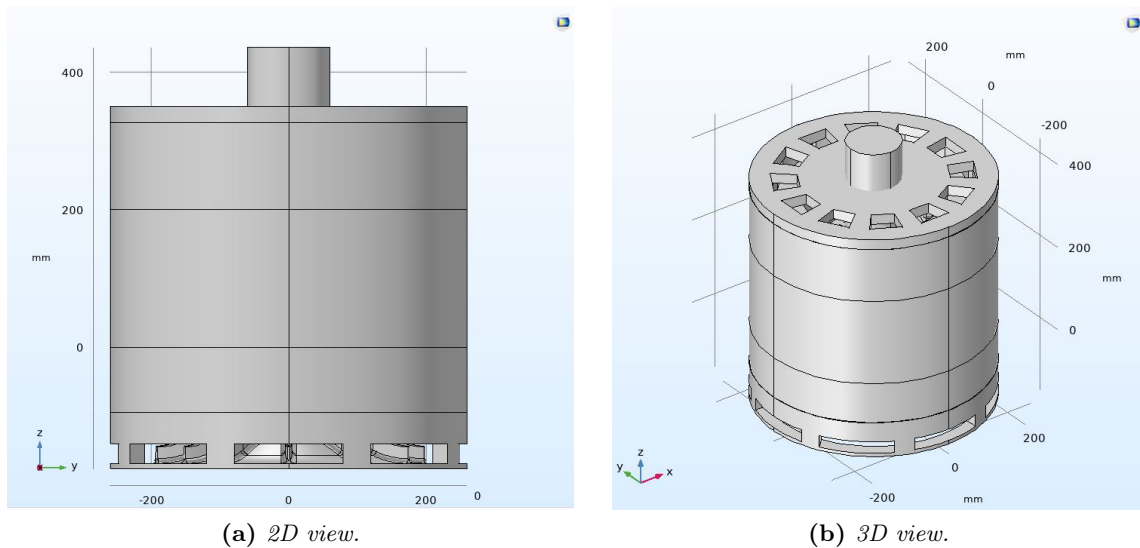


Figure 3.2: 2D (a) and 3D (b) view of motor model.

The next step consists in the boundary conditions definitions, representing the constraints for the solution of a differential equation to be resolved in a domain. Typically, when the boundary conditions need to be established, another node through physical boundary needs to be added. In particular, when this region needs to be divided by external, they are applied to geometric entities. Considering the same issues explained in chapter 2, it is possible to select the parts to whom are applied boundary conditions, as reported in figure 3.3.

Regarding to inlet, it is based on pressure or velocity data. Considering the pressure, this can be specified through a stress condition where the flow direction is required, which allows to have a well-posed condition. The inlet pressure value is set equal to $0.5 * spf * rho * w^2$ Pa, where *spf* represents a generic function to develop the study and rho is the density.

Referring outlet conditions, the typical approach uses a pressure through normal stress condition at the outlet; in this case the pressure is set equal to $P_0 = 0$ Pa.

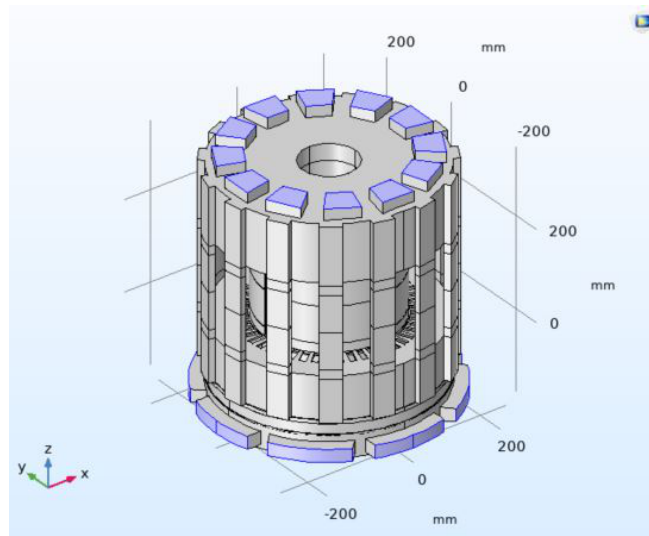


Figure 3.3: Example of boundary conditions selection.

3.3 Solver Setup: *Frozen Rotor* Function

The next step of CFD analysis concerns the resolution of equations with iterative method. This means that a solver needs to be used. Typically, to simulate turbulent flow the Navier-Stokes equations are mainly used, however the problem is linked to the high number of scales that are required in the flow. An alternative involves to considering the flow quantity divided into mean values and fluctuations where the relative effect through a turbulence closure is modeled. In this way, solving the model for the turbulence shutting, the computation is less expensive in respect to solve all turbulence scales.

As above-mentioned, considering a weakly compressible flow, it is possible to use a k - ϵ turbulent model, where the variables are the *kinetic energy* k and the *turbulent dissipation rate* ϵ . In this way the turbulent viscosity can be modeled as in 2.2. As previously done, the applied solver is the Frozen Rotor function.

This feature is mainly governed by *Navier-Stokes* and *continuity equations* and, as previously mentioned, it is useful for saving computational time and resources. Considering that a typical CFD model of an electric motor uses sliding mesh, this approach is obviously accurate but it is computationally intense and requires a transient simulation where the start-up of the motor is simulated until to obtain the desired rotational speed. To avoid this, it has been replaced by frozen rotor approximation for a given rotational speed.

In COMSOL, the frozen rotor function is especially used for flow in rotating machinery when the geometry topology is invariant with rotation. It is a good approximation to compute the velocity, pressure, turbulence, temperature for flow in rotating machinery and considering the particular case of *Stationary Study*. Through this function, it has been assumed that the rotating parts are frozen in position and, instead, the rotation is executed considering centrifugal and Coriolis forces.

In the case study, the rotor is frozen relative to the stator and the forces are added to the domain surrounding the rotor [22], [23]. From equation point view, the frozen rotor function allows, through rotating coordinate equations, to write and simplify the flow in the rotating domain as previously mentioned in 2.7.

This feature blocks the motion in a given position so that it allows to study the flow field with a fixed position of the rotor. A typical approach provides a good estimate of the pseudo-steady-state condition of the flow [4]. In the case study, the air speed results have been obtained considering a rotation speed velocity equal to 1000 and 2500 rpm. In particular the variation of the air speed and of the flow rate (mass or volume), in function of rotation speed and temperature, have been examined. The considered temperature is 20°C.

It is important notice that the air speed raises with an increase of rotation speed and temperature. In the same way, also the flow rate increase.

3.4 Mesh Qualities

Frozen Rotor function defined, the next relevant feature developed and improved is relative to the mesh. Typically, the CFD quality is linked to the mesh quality used to solve the problem. Obviously, the good mesh simplifies the convergence and improves the results accuracy but it also needs a high computational features. In this section, a good job about the mesh quality has been done; in fact, in order both to reduce the calculation time and to keep the accuracy, it has well been optimized.

COMSOL allows to guarantee the no-violation of the mesh laws; in particular empty regions must not exist in the computational domain and must not be overlapping mesh elements.

To improve the mesh feature and to guarantee a high mesh quality it needs to have an isotropic material such that the worst elements could be avoided. The improvement step which has been done concerns to guarantee relevant actions in regions where the flow is not neglectable [34], [35].

In addition to this, the mesh should be refined where a good accuracy is requested; to achieve this, a good action could be to build a symmetric geometry because it removes around 50% of the elements and reduces the computation time, with reasonable accuracy as well. [4]

Virtual Operations function, such as *Form Composite Faces* or *Domains*, have been often used to achieve this well-mesh improving the model where, for example, anisotropy is not neglectable, guaranteeing both improvements and a computational time decrease. This mentioned, the work has been developed achieving two separated studies relative of two different mesh quality.

1. The *Mesh 1 Study* is a low mesh quality where the accuracy is satisfied and the computation time is low. The mesh setup in order to have an element size calibrated for Fluid dynamics equal to *Extra Coarse* has been imposed. For each domain and boundary, elements have been selected and defined, as shown in figure 3.4;
2. The *Mesh 2 Study* is characterized by high mesh quality where the mainly difference is based on the element size of the mesh that has been set on *Coarser* element size. In this way, performing the same steps and considering the same reasonings of the Study 1, the improvements have been obtained. Obviously, the calculation time, comparing to the first mesh, is increased but, considering the total thermal development, this is considerably reduced in front of a 5% error between two studies.

These results represent the starting point to develop a good complete thermal model.

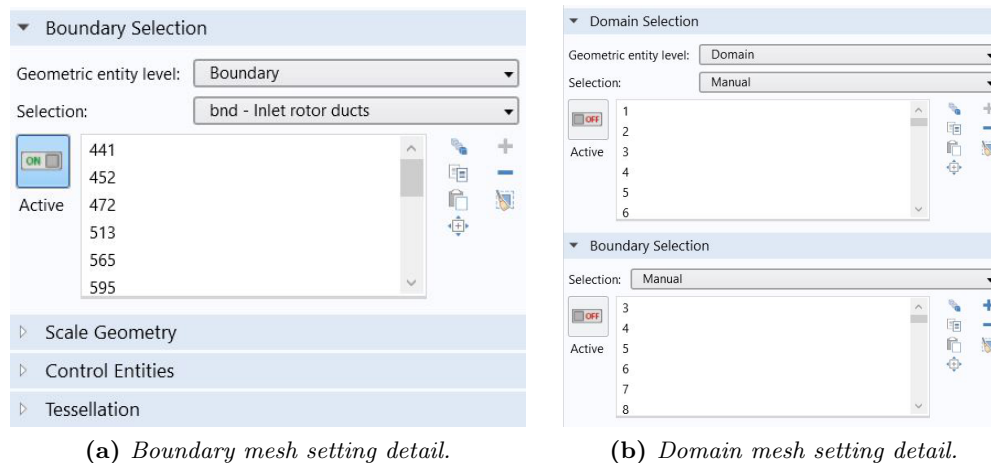
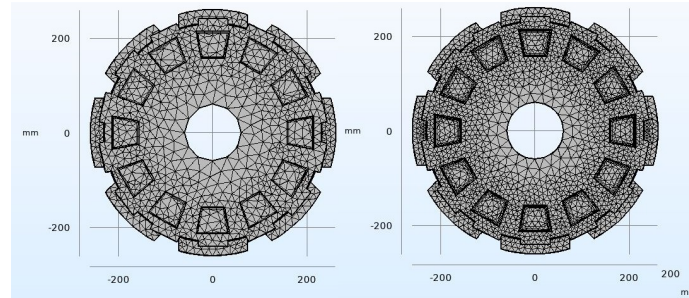
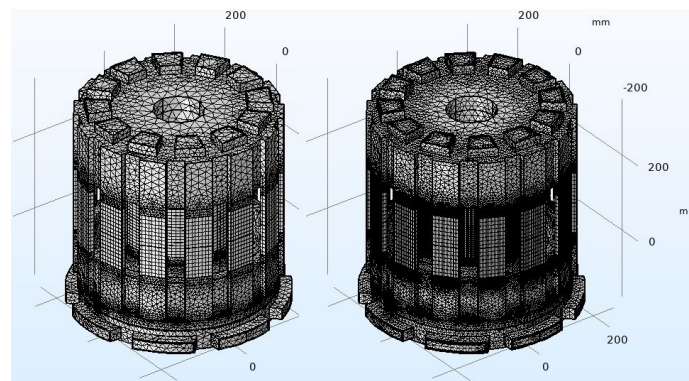


Figure 3.4: Mesh setting.

In figure 3.5, a mesh comparison between Study 1 and Study 2 through 2D and 3D view is shown.



(a) 2D detail view comparison CFD model mesh.



(b) 3D view comparison CFD model mesh.

Figure 3.5: 2D (a) and 3D (b) comparison for mesh 1 and 2

In order to know an overview of the created mesh, COMSOL provides the possibility to evaluate the statistics [22], [23]. In the statistic mesh window, a variety of data for different selections and measures quality are showed. The possibility to change the selection of the elements, e.g. domains and boundaries, knowing the relative numbers, is provided. *Skewness*, *maximum angle*, *volume versus circumradius*, *volume versus length*, *condition number* and *growth rate* are only several measures quality that the statistic mesh window allows to know.

They are shortly described below:

- The *skewness* is a measure for most mesh types. It is a report relative to bad element quality during mesh generation. Furthermore, this is based on the equiangular skew where the elements with large or small angles, comparing to the angles in an ideal element, are penalized;
- The *maximum angle* is a measure adapted for meshes where anisotropic elements are desired and then only elements with large angles are penalized;

- The *volume versus circumradius measure* is used in order to know a quotient of the element volume and the radius of the circumscribed circle of the element. It is sensitive to large angles, small angles and anisotropy. In particular, for triangular meshes in 2D or tetrahedral in 3D, it is a most suitable measure;
- The *condition number* is based on properties of the matrix transforming the actual element to an ideal element;
- The *growth rate* is based on a comparison of the local element size to the sizes of neighbouring elements in all directions.

Considering the numerical values, a quality mesh value close to 1 is the best possible, representing an optimal element in the chosen quality measure and instead the value equal to 0 is representative for degenerated elements.

In COMSOL, as above-mentioned, the meshing algorithm is developed to avoid low-quality elements; however, for high geometric aspect ratios, small edges and faces, the mesh quality developed could be low. To can guarantee an accurate result, it is important to know which minimum element quality and average element quality are sufficient for standard application. In general, elements with a quality around 0.1 are characterized by a poor quality and when it is around 0.01, it should be avoided.

However, in particular applications where the low quality elements in parts with less importance are located, elements with low quality could be accepted.

Finally, in the statistic mesh window, in order to get a quick knowledge about the quality mesh, a characteristic histogram can be analyzed.

Some above-mentioned characteristics about mesh quality are shown in figure 3.6 below.

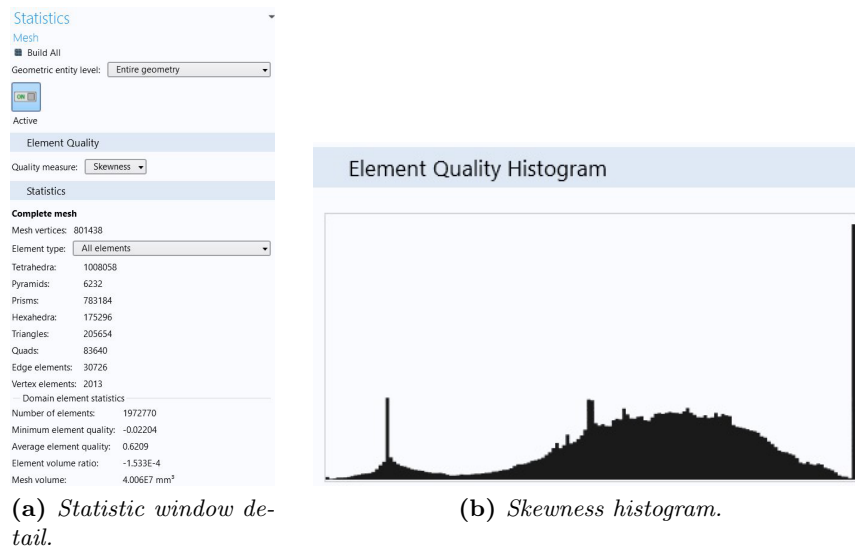


Figure 3.6: Mesh 2 statistic.

To get a knowledge of numerical report values about the mesh elements, it is also possible to plot the meshed model considering different colours to represent different elements quality. This can be observed with a comparison between mesh 1 and mesh 2 in figure 3.7 and in table 3.1.

	Mesh 1 Extra Coarse	Mesh 2 Coarser
Quality measure	Skewness	Skewness
Mesh vertices	163852	801438
Element type	All elements	All elements
Tetrahedra	303340	1008058
Pyramids	4045	6232
Prisms	137631	783184
Hexahedra	21594	175296
Triangles	72809	205654
Quads	17260	83640
Vertex elements	2013	2013
Number of elements	466610	1972770
Minimum element quality	-0.007441	-0.02204
Average element quality	0.5804	0.6209
Element volume ratio	-6.604E-4	-1.533E-4
Mesh volume	4.006E7 mm ³	4.006E7 mm ³

Table 3.1: Mesh 1 and mesh 2 comparison.

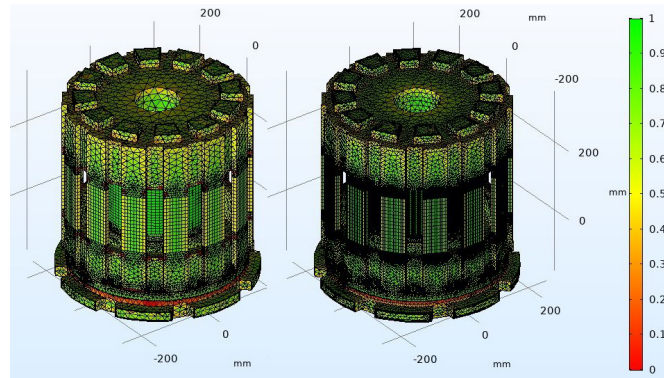


Figure 3.7: 3D view of CFD model mesh results.

3.5 CFD Results

The last topic about CFD calculation is reserved to analyze and discuss the obtained results, considering the two mesh studies, explaining and comparing them. As mentioned, data input set are mainly *rotational speed*, *temperature* and *pressure*. The considered rotational speed are 1000 and 2500 rpm, with a temperature set equal to 20°C and finally the pressure is considered constant and equal to 1 atm.

To get a flow behaviour knowledge, the achieved results are the *air speeds* [m/s] in stator ducts, rotor ducts and air gap and the *flow rate*, expressed by *volume flow rate* [m³/s] and *mass flow rate* [kg/s]. These results to calculate heat transfer coefficient are then used.

It is important to notice that both the air speed results in the different motor parts and the flow rate raise their values in direct proportion to the increase of rpm and temperature where, developing a linear behaviour, involve to not calculate the results for each rotation speed.

In fact, the fan pressure and the power vary directly with the ratio of the air density at the inlet to the standard density and the flow rate is instead not affected by the air density. In charts of 3.8(a) and (b) the flow rate, expressed in volume and mass, for Study 1 and 2 is shown. In particular, the linearity of the trend, that allows to demonstrate the validity of use only one two rotation speeds, can be observed.

The same topic is also valid for the figure 3.9(a).

In the first, the stator ducts air speed trend comparison for Study 1 and Study 2 is shown. In figure 3.9(b) is instead reported the air speed trend for stator ducts, rotor ducts and air gap for Study 2 only one.

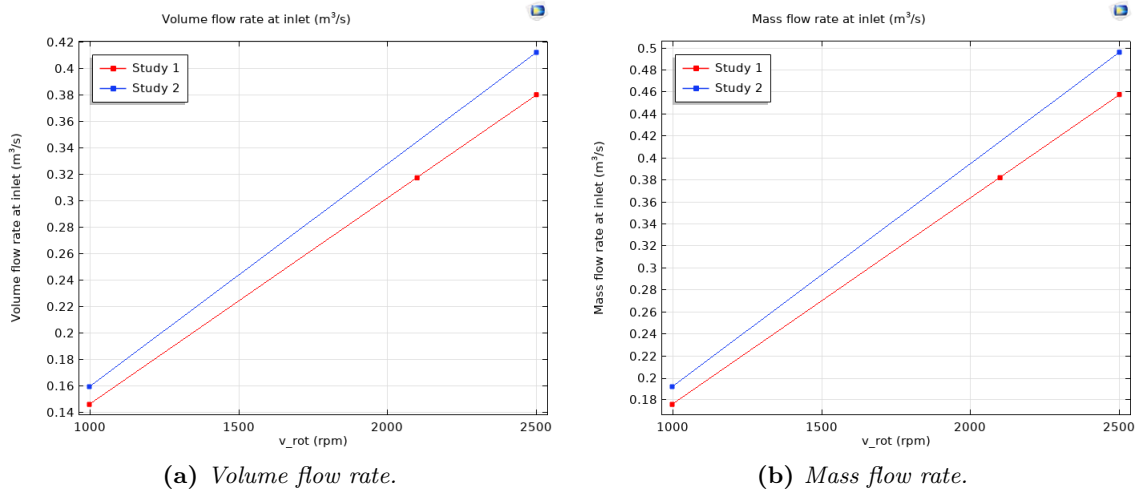


Figure 3.8: Flow rate increase in function of rotational speed at 20°C for Study 1 and Study 2. Flow linearity could be observed.

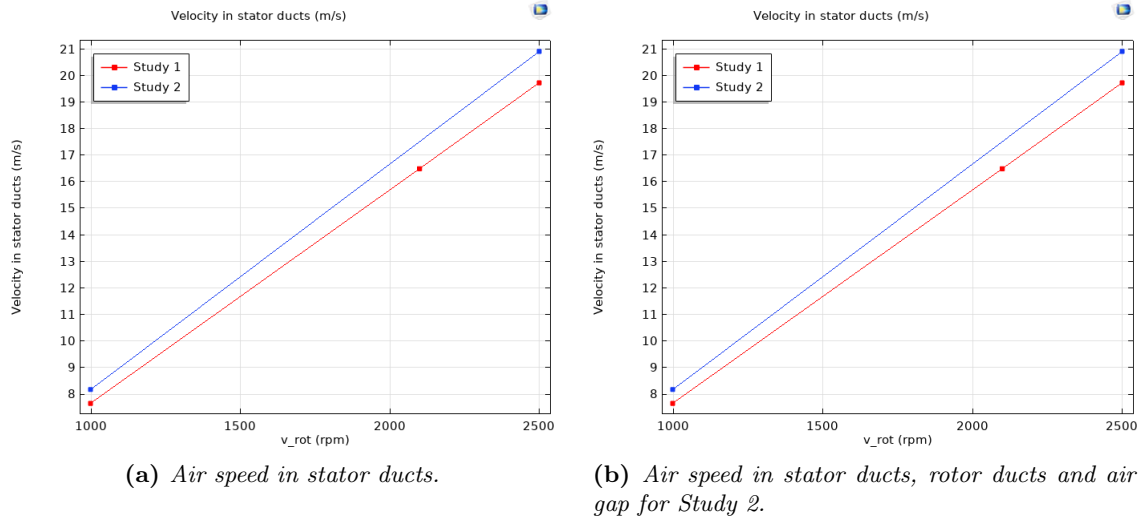


Figure 3.9: Air speed increase comparison. Trend linearity could be observed.

The linearity of the trend is also noticeable referring to numerical results reported in table 3.2.

In this way, considering the behaviour approximated with straight line, an EXCEL implementation to obtain air flow results (and heat transfer coefficient values, as in chapter four explained) at any speed, has been developed.

Motor part	Rotation speed [rpm]	Study 1	Study 2
		Air [m/s]	Air [m/s]
Stator ducts	1000	7.6503	8.1750
	2500	19.7384	20.9242
Air gap	1000	2.3469	2.2891
	2500	7.5975	6.9802
Rotor ducts	1000	9.4763	10.6639
	2500	24.5641	27.5665

(a) Air speed results °C.

Rotation speed [rpm]	Study 1	Study 2
	Flow rate [m ³ /s]	Flow rate [m ³ /s]
1000	0.1463	0.1597
2500	0.3803	0.4123

(b) Flow rate results °C.

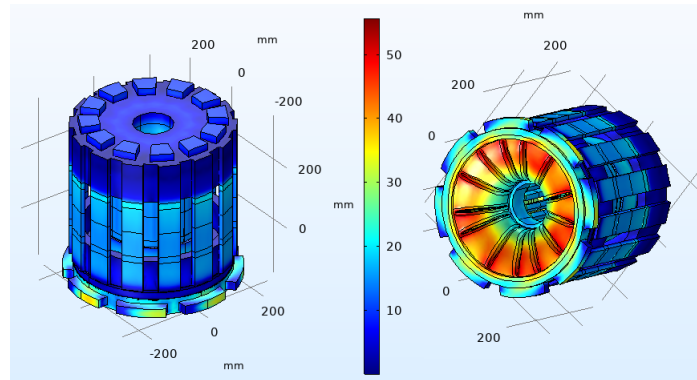
Table 3.2: Air speed (a) and volume flow rate (b) results at 20°C for Study 1 and Study 2.

Through numerical values has been also possible to evaluate the percentage difference between air speed and flow rate results obtained with Study 1 and 2 for further accuracy proof.

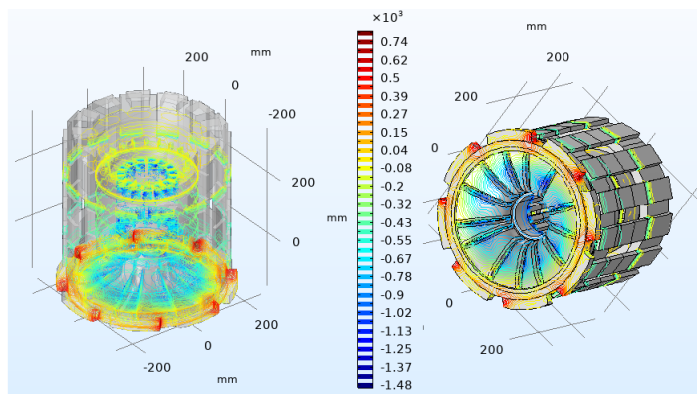
They are around to 2%, 6% and 12% for air gap, stator and rotor ducts respectively and 8% for volume flow rate.

After numerical values discussed, the same results in a graphic way can be observed.

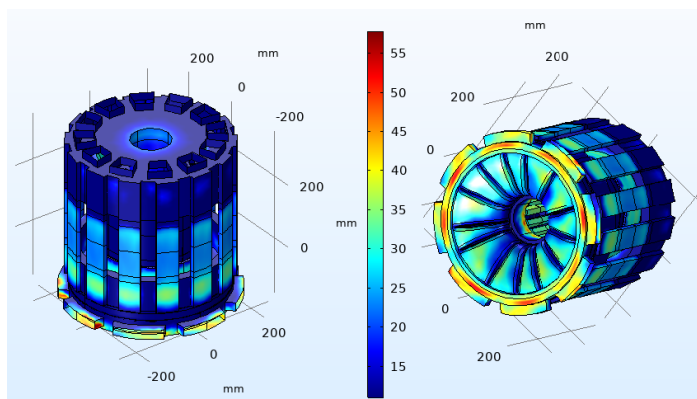
The velocity, pressure and wall resolution behaviours, considering the motor model structure, in different views, for Study 1 and 2, are shown in figure 3.10.



(a) Velocity behaviour for Study 1.



(b) Pressure behaviour for Study 2.



(c) Wall resolution behaviour for Study 1.

Figure 3.10: Graphics results at $v_{\text{rot}1} = 2500$ rpm for Study 1 and 2 respectively.

To conclude, as previously mentioned, the calculation time has been significantly reduced by purposeful model simplification and optimizations, anyway guaranteeing a good accuracy of the results, as shown in figure 3.11 where, from MATLAB elaboration, volume flow rate in function of rotation speed is reported, considering three different mesh types and the measurement trend, as it will be discussed in chapter 5. The meshes increasing their quality with correspond to an increase of the results and calculation time are obtained. Beyond that the linearity of the results is important to notice the calculation time that, as in the introduction mentioned, has been decreased from hour to days per rotational speed to around 30 minutes for high quality mesh, keeping the accuracy of results with a variation of small percentages between the results of the different meshes.

In particular it is possible to notice the perfect overlap obtained between measurements and mesh 3 results. This shows the increase of mesh quality coincides with an increase of the results.

As in the introduction mentioned, to calculate air flow in the electric motor case study and to get a good comparison between simulation time and results, an ABB workstation laptop characterized by 32 Gb of RAM and 16 cores and a standard laptop with 16 Gb-RAM and 8 cores CPU have been adopted.

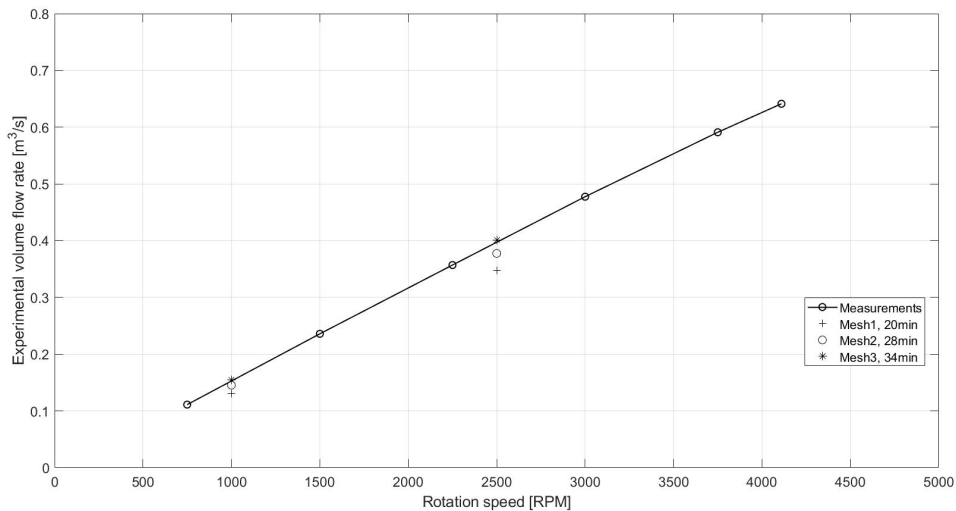


Figure 3.11: Comparison between CFD calculation results for flow rate at different mesh qualities.

Chapter 4

Thermal Modeling of Traction Motors

Subsequently to the CFD modeling presentation, in this chapter the air speed results, obtained through CFD calculation, are implemented as input data to develop the final thermal model to calculate temperature in the electrical machines critical parts when they work in intermittent operations.

4.1 Introduction

As above-mentioned the main requirements that distinguish traction applications from other standard motors are represented by the variety of cooling system and running condition. In fact, cooling systems can be liquid-cooled or air-cooled, considering different open shapes, e.g. closed or semi-closed, supplied by the same shaft-mounted or by external fans. In this case study, the fan is supplied by shaft-mounted.

In an electrical machine, to know the internal temperature in a given operating point during design is important. This because the maximum continuous rating calculation needs an adequate thermal model to know a cooling provision to avoid overheating due to the maximum current density in the windings. Furthermore, the stator temperature is linked to the efficiency and as such the resistivity of the copper windings increases with temperature. Finally, an inaccurate prediction needs an excessive safety margins. Improvements would reduce the number of prototype iterations required and minimize the cost.

As previously said, in this application the running conditions are intermittent and they involve that torque and speed are expected in every second of operation. All these aspects imply that a generic thermal modeling method should be developed covering different cooling to obtain an acceptable computation time.

To develop this, CFD analysis and thermal FE have been used, where the first method is combined with the analytical approach to reduce the size and complexity of the CFD and FE models. In particular, the air speed results of CFD calculation to estimate hot-spot temperature in the solid parts have been used.

Subsequently, separating the thermal model from the CFD, a generic method has been obtained where the calculated heat transfer coefficients, from velocity information, in the thermal model have been used.

To obtain an efficient developed thermal method, the functions used in numerical models are chosen to get the minimum possible calculation time and with the purpose to keep a good accuracy.

As explained in chapter 3, a good CFD calculation, allows to obtain an optimal thermal model.

Subsequently to CFD improvements, another important aspect concerns the 3D-FE analysis relative to the model of solid critical parts [2].

This step is relative to the parts of the model which are thermally critical and, to simulate analytically with a high accuracy, through FE modules they are modeled. The most critical parts that are modeled in FE are winding, active part and end windings.

A possible generic code algorithm to obtain an implementation to develop the complete thermal results in figure 4.1 is shown. This algorithm considers analytical and numerical modeling methods together, where thermal resistances, capacitances, heat sources and heat transfer coefficients in LP model are considered from CFD calculation results, dimensional data, losses and material properties.

Finally, the model has been run.

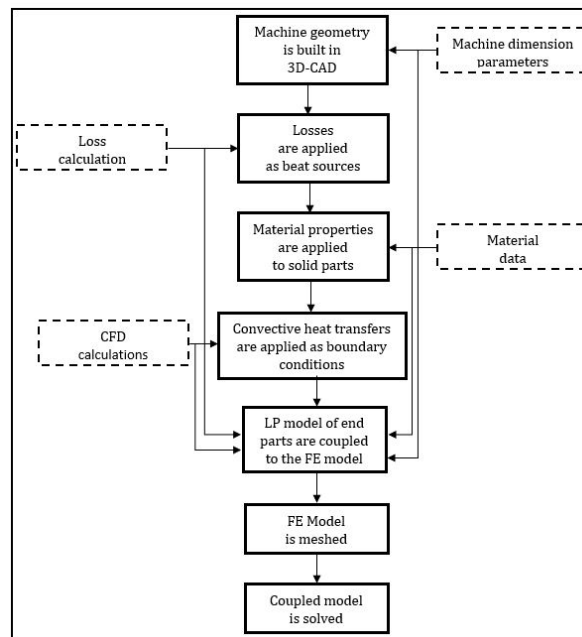


Figure 4.1: Thermal model algorithm.

4.2 Analytical Thermal Model

As mentioned, the developed thermal model considering different steps has been developed. The first important step concerns about 3D-Finite Element model. Convection is the heat transfer process due to fluid motion. In the case of natural convection, this motion is due to forces resulting from density variations in the fluid. If the fluid motion is forced, the fluid movement is achieved by an external force.

In this case study, this is a forced system where the fan represents the motion force. When the fluid velocity is large, the system makes a turbulence motion, called turbulent flow.

Otherwise, the mixing of hot and cold air is more efficient and the heat transfer increases.

The empirical heat transfer correlation, based on dimensionless analysis, are used to predict the heat transfer coefficients. The heat transfer coefficient (HTC) is the quantitative expression of the conductor capacity to be subject to thermal current such as convective transfer, between fluid and solid.

In an electrical machine fan-cooled, as this case study, the forced convection heat transfer gives improved dissipation, in respect to other cases, with the fan is fitted to the end of the shaft.

From CFD calculation the inlet air velocity has been estimated and, as said in chapter 3, the air velocity at the start of fan side is known. As above discussed, the air velocity and the flow rate are in a linear relationship with the shaft speed. After the calculation, in different motor parts the convective heat transfer has been applied to the FE model through boundary conditions using analytical models derived by the CFD calculation. In particular two FE models have been used.

A possible thermal modeling scheme based on combination of lumped parameter and numerical modeling methods considering the 3D-FE model can be observed in the figure 4.2.

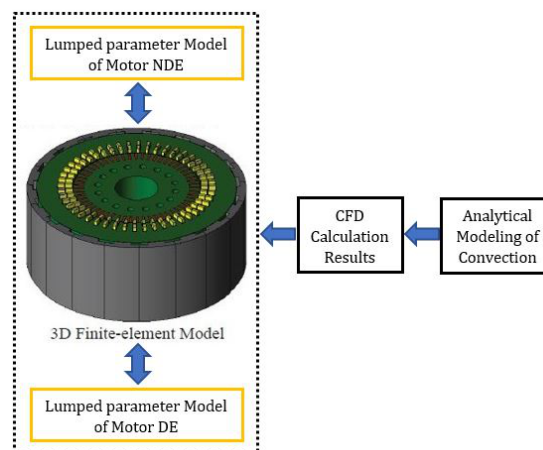


Figure 4.2: 3D-FE Model scheme [2].

The FE model includes the stator coils, stator lamination, housing, rotor bars and rotor lamination.

The temperature difference between the cold side and the hot side, where inlet and outlet are respectively located, and the complete active part of the motor should achieve an accurate estimation of temperature variation in the motor axial direction. The final result is a 3D finite element model of the motor active part to estimate a temperature variation in the axial direction guaranteeing a separate connection to end windings and bearings in drive and nondrive-end part. Through the 3D model, from 2D model, it is possible to reduce the estimate temperature difference between the cold and hot sides of the motor. However, the end winding hot spot temperature in the motor hot side cannot be estimated with good accuracy. About solid parts, they are modeled considering their thermal conductivity, specific density and mass density.

The stator coil complex structure is composed by copper conductors, slot linear, coil dividers, contact surfaces and impregnation. All these parts, where they are included, are accurately modeled.

The contact surfaces are modeled as boundary conditions between solid parts. Considering the convective heat transfers, from the housing and rotor/stator laminations to the coolant, have been modeled taking account boundary conditions with corresponding heat transfer coefficient.

Then, analyzing stator ducts, rotor ducts and the air gap, the heat transfer coefficients can be obtained considering different parameters [2]. Data are normally dimensionless and it allows that both the number of variables is reduced and the results to different machine sizes can be applied.

Furthermore, considering the linearity of CFD results, implementing an EXCEL algorithm, the HTC have been quickly derived.

Before to explain the heat transfer coefficients calculation, it is important to summarize about the fluid behaviour parameters. In fact, the HTC behaviour is linked to the velocity of the fluid. As mentioned in chapter 2, the flow behaviour is linked to the *Reynolds Number* (Re), that is a dimensionless number used in fluid mechanics to predicts flow patterns in different fluid flow situation.

Considering the Reynolds number formula 2.1, the flow in *laminar* and *turbulent* flow can be divided. The first occurs when a fluid flows in parallel layers, and, at low speeds, it tends, to flow without lateral mixing. The second instead occurs when the velocity increases in respect to laminar flow and being a flow less orderly, small packets of fluid particles are in lateral mixing.

Proportionally to the flow velocity, also the Reynolds number is low when the flow is laminar and higher when it is turbulent respectively. Between the two behaviours an intermediate zone is placed, called *transition zone*, as shown in figure 4.3.

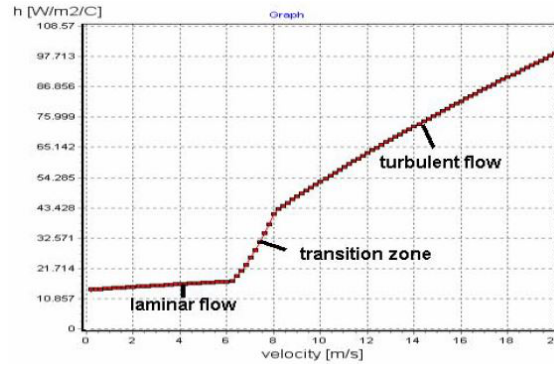


Figure 4.3: Heat transfer behaviour function of velocity.

However, as well as for speed the Reynolds Number also varies in function of ducts shape (circular, rectangular, etc.) and ducts zone (stator, rotor), as subsequently below shown.

Over than Re , another nondimensional parameter is represented by the Nusselt Number (N_u); it is obtained by the ratio of convective to conductive heat transfer across the boundary, as shown in standard equation 4.1 [37]:

$$N_u = \frac{h_{conv}}{h_{cond}} = \frac{h}{\frac{k_{\Theta}}{L_c}} \quad (4.1)$$

where h is the *flow HTC*, L [m] the *characteristic length* and k_{Θ} the *fluid thermal conductivity*. Starting from this, the HTC applied to the thermal model in the different motor parts, as described below, are calculated [2], [6].

I. Stator Heat Transfer coefficient

In the stator ducts, the HTC is defined as:

$$h_s = \frac{\rho N_u}{L_a} \quad (4.2)$$

where ρ [kg/m³] is the *density* function of the *temperature* θ [Kelvin or Celsius], N_u is the *Nusselt Number*, L_a [m] the *active length*.

It is necessary to distinguish N_u in function of the ducts shape and the flow (laminar or turbulent).

The following formulas, exploiting Reynolds number Re , to calculate the Nusselt number N_u in stator ducts, rotor ducts and in the air gap have been used.

When the flow is laminar, $Re < 2800$, and stator ducts are rectangular is valid:

$$Nu = 7.49 - 17.02 \frac{H_{duct}}{W_{duct}} + 22.43 \left(\frac{H_{duct}}{W_{duct}} \right)^2 - 9.94 \left(\frac{H_{duct}}{W_{duct}} \right)^3 + \frac{0.065 Re Pr \frac{L_c}{L_a}}{(1 + 0.04 Re Pr \frac{L_c}{L_a})^{\frac{2}{3}}} \quad (4.3)$$

where H_{duct} [m] is the *stator duct height* and W_{duct} [m] is the *stator duct width*, Pr is the *Prandtl Number* and L_c [m] is the *characteristic length* or *channel hydraulic diameter*, calculated as:

$$L_c = \frac{4A}{P} = \frac{2(W_{duct}H_{duct})}{W_{duct} + H_{duct}} \quad (4.4)$$

When the rotational speed increases, the air velocity in the cooling ducts also enhances and the flow becomes turbulent. Then, for turbulent flow, $Re > 2800$, Nu is:

$$Nu = \frac{\frac{f}{8}(Re - 1000)Pr}{1 + 12.7\sqrt{\frac{f}{8}}(Pr^{\frac{2}{3}} - 1)} \quad (4.5)$$

where the friction factor f is calculated as:

$$f = [0.79 \ln(Re) - 1.64]^{-2} \quad (4.6)$$

As previously mentioned, Nu is function of Re , which is directly proportional to the CFD air velocity calculated in the third chapter.

II. Rotor Heat Transfer Coefficient

The rotor HTC formula is the same valid for stator ducts 4.2:

$$h_r = h_s = \frac{\rho Nu}{L_a} \quad (4.7)$$

In respect to stator ducts, in this case for laminar flow, circular shape and $Re < 2300$, Nu is equal to:

$$Nu = 3.66 + \frac{0.0668 \frac{D}{L_a} Re Pr}{1 + 0.04 \left(\frac{D}{L_a} Re Pr \right)^{\frac{2}{3}}} \quad (4.8)$$

where D [m] is the *equivalent diameter* for circular ducts considering rotor ducts area as a trapezoidal one, where $B_{duct_{max}}$ [m] and $B_{duct_{min}}$ [m] are *major* and *minor duct base* respectively. In this case study rotor ducts are trapezoidal, then:

$$D = \sqrt{\frac{B_{duct_{max}} + B_{duct_{min}}}{\pi} H_{duct}} \quad (4.9)$$

When the flow is turbulent and $R_e > 2300$, N_u is equal to 4.5:

$$Nu = \frac{\frac{f}{8}(R_e - 1000)P_r}{1 + 12.7\sqrt{\frac{f}{8}}(P_r^{\frac{2}{3}} - 1)} \quad (4.10)$$

III. Air gap Heat Transfer Coefficient

The air gap HTC formula is the same previously defined in 4.2 and 4.7.

Considering that the flow in the air gap is axial due rotor rotation, N_u through two models is described.

When the rotational speed is low and the axial flow velocity is high and the condition is $R_{e_{rd}} < 4e4$ and $R_{e_{ax}} < 6.5e5$, the *Kuzay-Scott* model is [2],[6]:

$$Nu = 0.022 \left[1 + \left(\frac{L_{ag}v_r}{\pi \frac{D_{RO}}{2} u} \right)^2 \right]^{0.8714} R_{e_{ax}}^{0.8} P_r^{0.5} \quad (4.11)$$

When the rotation speed is high and $1.4e4 < R_{e_{rd}} < 2.7e6$ the *Childs-Turner* model considers [2, 7]:

$$Nu = N_{u_z} \left[1 + 0.068 \left(\frac{v_r}{u} \right)^2 \right] \quad (4.12)$$

where D_{RO} [m] and D_{SI} [m] are the *outer rotor* and *inner stator diameter* respectively, v_r [rpm] is the *rotational speed*, u [m/s] is the *axial air velocity*, L_{ag} [m] is the *radial air gap length* as 4.13, N_{u_z} is a *coefficient for higher rotational speeds* calculated as 4.14, $R_{e_{rd}}$ and $R_{e_{ax}}$ are the *Radial* and *Axial Reynolds Numbers* calculated respectively as 4.15 and 4.16:

$$L_{ag} = D_{SI} - D_{RO} \quad (4.13)$$

$$N_{u_z} = 0.023 R_{e_{ax}}^{0.8} P_r^{0.5} \quad (4.14)$$

$$R_{e_{rd}} = 0.1047 \frac{\left(\frac{D_{RO}}{2}\right)^2 v_r}{\mu} \quad (4.15)$$

$$R_{e_{ax}} = \frac{\rho L_a u}{\mu} \quad (4.16)$$

About N_u calculation, in this case it is important to assert that the flow is rarely laminar in the traction motors, just at low rotational speeds. When the axial flow through the air gap is not considered increases, it is described through the *Taylor* model reported in 4.17 and 4.18:

$$N_{u_{Ta}} = 0.409 T_a^{0.241} - 137 T_a^{0.75} \quad (4.17)$$

$$T_a = R_e \left(\frac{L_{ag}}{\frac{D_{RO}}{2}} \right)^{0.5} \quad (4.18)$$

However, in this case study, being the rotor rotating, the air gap HTC are 4.11 and 4.12.

IV. Other Heat Transfer Coefficients

The heat transfer coefficients for short circuit ring, end windings, shaft and end plate can be written, replacing, in the rotational speed v_{r_x} [rpm], x for with the relative element, as:

$$h_x = 15(1 + 0.4v_{r_x}^{0.9}) \quad (4.19)$$

Knowing the CFD air speed results, air gap, stator and rotor ducts characteristics and formulas, an EXCEL implementation to calculate the HTC in the different parts of the motor has been developed, as shown in figure 4.4.

In this way, considering the air speed values obtained from CFD calculation at only two rotational speed, e.g. 1000 and 2500 rpm, in data input, exploiting the behaviour linearity, the HTC for the different motor parts are immediately calculated in function of whatever rotational speed.

HTC algorithm at different speed values									
	v_rot (rpm)	Stator (m/s)	Rotor (m/s)	Airgap (m/s) [no axial flow]	Airgap (m/s) [axial flow]				
Input speed values	1000	8,17498771	10,66393172	2,28908013	2,28908013		<-- Insert CFD values		
	2500	20,9241835	27,56650101	6,980167238	6,980167238				
Output speed	2100	17,524398	23,0591492	5,729210676	5,729210676				
Re	-	45655,6684	31767,13666	1119,457612	Re_rad	Re_ax	Nu_l [Re_rad<E4; Re_ax<6.5E5]	Nu_h [1.4E4<Re_ax<2.7E6]	Nu_z
fr - Ta	-	0,02140026	0,023313732	80,23463064	3928,5142	1119,45761	5,120235503	16,7651825	5,34671432
Nu	-	98,3580368	74,31952437	3,158136266	5,120235503				
h	2100	584,246738	441,4579748	18,75932942	30,41419889				

Figure 4.4: HTC Excel algorithm.

4.3 Thermal Modeling in COMSOL

4.3.1 Geometry and Physics

Subsequently to 3D-FE model analytical explanation, the COMSOL model has been built and developed. Starting from previously built motor model, without flow it has been run, considering the solid parts only one.

The rest of geometry is kept the same of the CFD model as shown in figure 4.5.

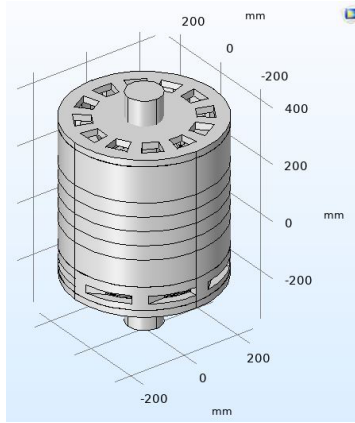


Figure 4.5: 3D view of motor model.

The geometry building explanation is the same of the chapter three; the only one difference concerns the layers building in order to model the heat flux and the temperature increase, as subsequently explained. Furthermore, to simulate the test heat capacity influence on the outlet bearing, in the geometry a short shaft part has been added.

More relevant are instead the differences about physics function, solver and materials setting. About the physics function, the *turbulent flow* function used in CFD model has been replaced by *heat transfer in solids* physic function.

This interface is used when heat transfer needs to be model by conduction, convection and radiation. The temperature equation defined in solid domains corresponds to the differential form of the Fourier's law that have additional terms like heat sources [22], [24], [25].

It is solved by the equation:

$$h_x = \rho C_p \left(\frac{\partial T}{\partial t} + \mu_{tr} \cdot \nabla T \right) + \nabla(q + q_r) = -\alpha T : \frac{ds}{dt} + Q \quad (4.20)$$

where C_p [J/(kg*K)] is the *specific heat capacity* at constant stress, T [K] is the *absolute temperature*, u_{tr} [m/s] is the *velocity vector* of translational motion, q [W/m²] is the *conduction heat flux*, q_r [W/m²] is the *radiation heat flux*, α [1/K²] is the *thermal expansion coefficient*, S [Pa] is the *second Piola-Kirchhoff stress tensor* and Q [W/m³] contains *additional heat sources*.

Considering this, the heat transfer interface is built exploiting thermal contact, heat source, heat flux functions, to simulate the different elements behaviour.

Thermal contact node defines the correlations for the conductance at the interface of two bodies in contact. It is applied for layers between conductors, layers between windings and stator lamination, contact surface and for bearings.

For example, the windings have been divided in layers where, in the thermal contact function, a specific thermal conductivity and thickness are defined, as shown in figure 4.6.

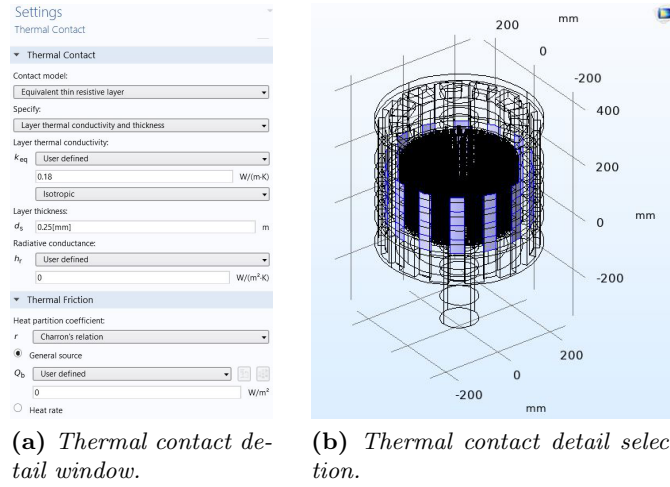


Figure 4.6: Thermal contact setup.

The *heat source* function is used to model the elements that represent the heat generation; windings, stator, rotor and bearings are selected considering for everyone the power losses expressed in Watt for each element, from the motor losses list.

In this way, the source terms Q_0 have been added, where Q_0 is the heat expressed like a linear heat rate:

$$Q_0 = \frac{P_0}{V} \quad (4.21)$$

where P_0 [W] is the power loss, V [m³] the total volume of the selected domains. In figures 4.7 heat sources details are shown.

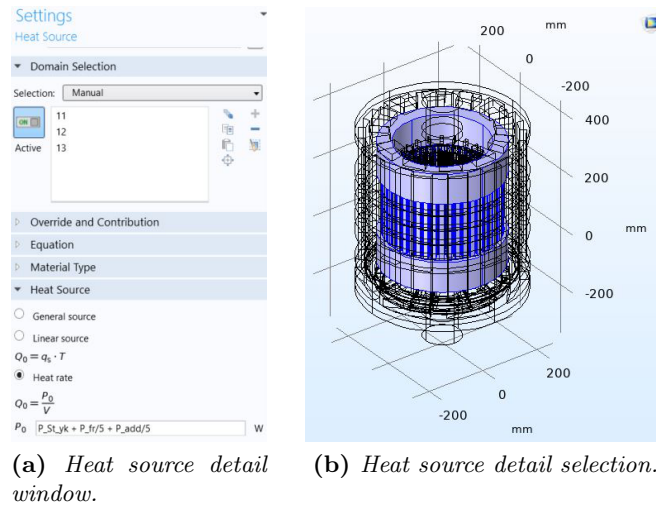


Figure 4.7: Heat source setup.

Focused on the power losses, the stator winding copper losses represent the more relevant losses and considering the current input to the motor and measuring the stator resistance are estimated.

In order to evaluate losses, the rotor cage losses from stator losses and laminations losses have been calculated, considering the measured stator input power.

Laminations and frictions losses are instead measured at no load and in different motor parts have been distributed.

Bearing losses, provided from bearing data sheet, in the two motor side have been divided.

In total, the losses term is equal around to 22 kW ¹.

Losses values are closely related to the materials selection and then the motor in different parts has been divided.

The materials selection has been made as follows:

- Aluminium for housing and contact surfaces;
- Steel for shaft and bearings;
- Iron for fan, air guide, rotor yoke and teeth and stator yoke and teeth;
- Copper for conductors, windings, rotor bars and short circuit ring.

For each material domain relatives physical and chemical properties have been set, such as *density* [kg/m³], *thermal conductivity* [W/(m·K)] which represents the material ability to conduct heat and *specific heat* [J/(kg·K)] which quantifies the amount of heat per unit mass required to increase the temperature by 1°C. Considering this, the influence of air specific heat in different motor points has been also considered.

In figure 4.8 an example of material selection with relative properties is shown.

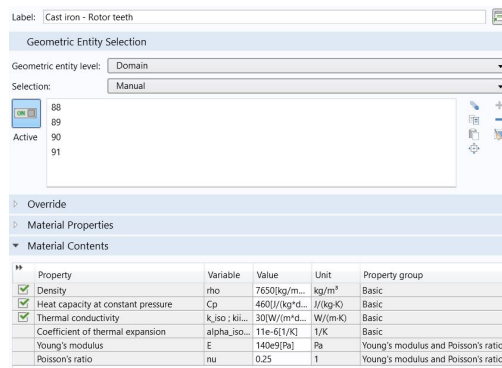


Figure 4.8: Example of material selection.

¹Provided by ABB laboratories

At last, the *heat flux* function is used to add heat flux across boundaries selecting ducts and channels where the air flows. In particular, the previous heat transfer coefficient for stator, rotor ducts and air gap calculated, are in this point applied. The active part is divided in four layers where, in everyone, the temperature increase obtained known inlet and outlet temperature is considered.

Having four active sub-zone to select stator, rotor ducts, and air gap, twelve different heat flux functions has been made. In figures 4.9 heat flux detail is shown [8].

For each element, the calculated HTC's h and the known *external temperature* T_{ext} have been applied.

The value depends on the geometry and the ambient flow conditions, as described in 4.22:

$$q_0 = h(T_{ext} - T) \quad (4.22)$$

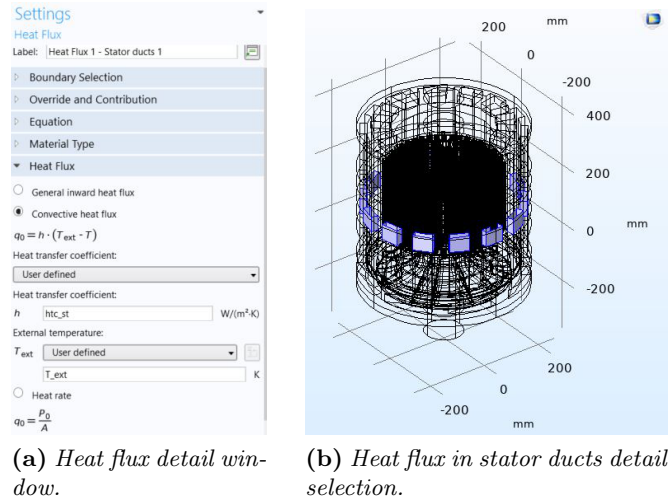


Figure 4.9: Heat flux setup.

4.3.2 Solver and Mesh Setting

Another difference between CFD and thermal model is relative to the solver. As explained, to calculate the air flow the frozen rotor solver has been used. In this step, instead, to run the model and to calculate the temperature a *time dependent* solver has been applied.

In heat transfer study, it is used to compute temperature changes over time. To evaluate the transient behaviour, in order to compare with the experimental measurement, the time lapse for the output starting from 0 to 4 hours, with step size of 30 minutes, has been set.

The mesh setting is similar to the CFD setting, where two mesh types have been evaluated and compared, guaranteeing a good accuracy and valid results.

In respect to CFD model where the mesh quality was extra coarse and coarser for Study 1 and 2 respectively, in this modeling coarser and fine mesh for Study 1 and 2 have been respectively analyzed.

Analyzing the figure 4.10 is noticeable the mesh increasing from Study 1 to Study 2. In particular, referring to quality mesh explanation in chapter 3 discussed, in figure 4.11 is noticeable the high quality of Mesh 2 than Mesh 1, with an average value around 0.7 in respect higher than mesh 1.

Finally, the calculation time is increased from mesh 1 to 2 respectively from around 4 minutes to 7 minutes, guaranteeing a good accuracy in every mesh.

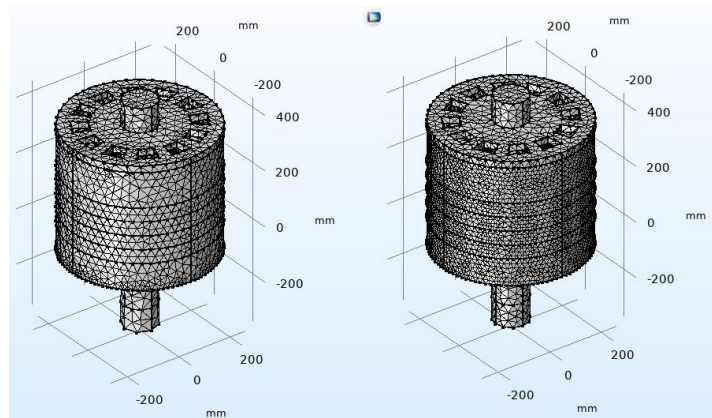


Figure 4.10: 3D view comparison of thermal model mesh qualities.

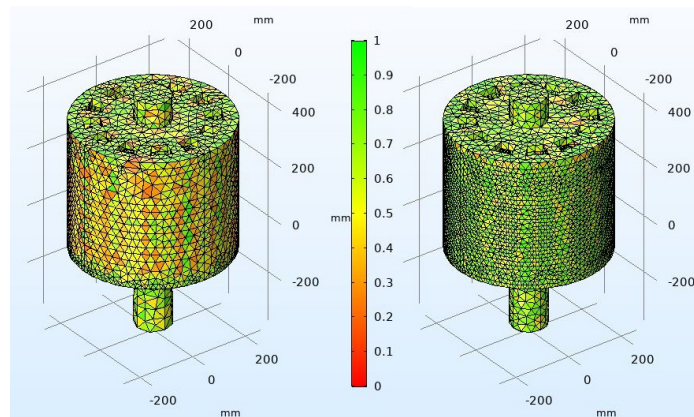


Figure 4.11: 3D view comparison of thermal model mesh results.

4.4 Temperature Results

After that thermal model run, in this chapter temperature results obtained considering the two different mesh are analyzed, discussed and compared.

To compare with experimental results in chapter 5 discussed, the temperature in different motor parts has been evaluated.

In particular, in the experimental setup 27 PT100 sensors ² have been applied in different points and in particular in stator, rotor, end winding, bearings and outlet.

In this way, to have a valid comparison attempts have been made the same sensors position in the thermal model, then considering different points in stator, rotor, end winding, bearings and outlet. As expected, the temperature results in each point have an exponential behaviour typical of the electrical motor.

Analyzing the figure 4.12, referred to outlet and stator slot respectively, is noticeable the same behaviour of two different mesh with a trends difference very low.

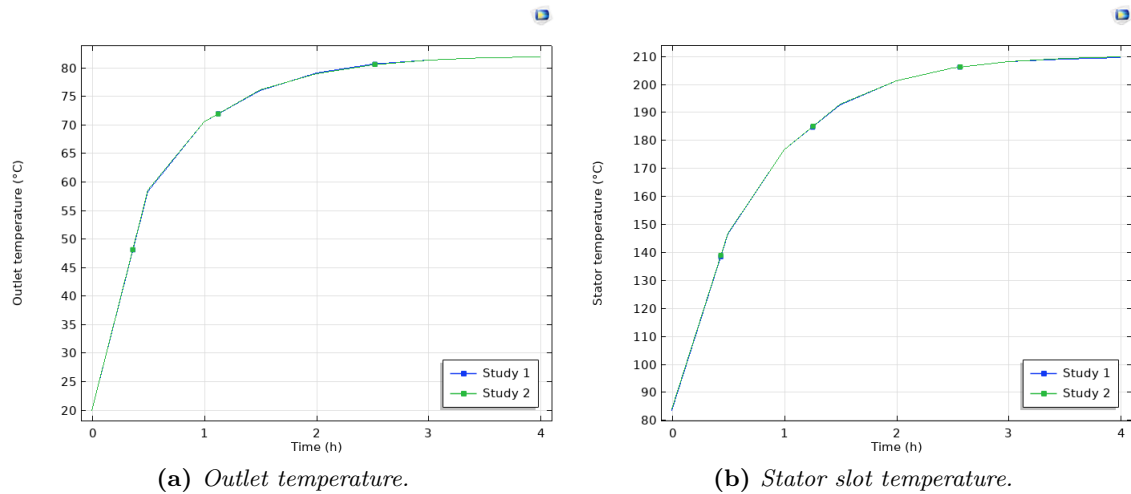


Figure 4.12: Temperature comparison in outlet (a) and stator slot (b) for Study 1 and 2.

²Provided by ABB test

The numerical results are instead reported in table 4.1, where the percentage difference $\Delta E\%$ between Study 1 and 2 has been calculated. The average $\Delta E\%$ is equal around to 1%.

Time [min]	Study 1 [°C]	Study 2 [°C]	ΔE [%]
30	58.392	58.696	0.52
60	70.642	70.594	0.07
90	76.159	76.211	0.07
120	79.140	79.082	0.07
150	80.694	80.640	0.07
180	81.447	81.425	0.03
210	81.830	81.824	0.01
240	82.001	82.020	0.02

(a) Outlet temperature °C.

Time [min]	Study 1 [°C]	Study 2 [°C]	ΔE [%]
30	155.832	156.078	0.16
60	187.187	187.329	1.96
90	203.297	203.799	1.77
120	212.291	212.502	1.46
150	217.092	217.182	1.25
180	219.235	219.515	1.41
210	220.078	220.679	1.51
240	220.952	221.237	1.52

(b) Stator slot temperature °C.

Time [min]	Study 1 [°C]	Study 2 [°C]	ΔE [%]
30	155.832	156.078	0.16
60	187.187	187.329	1.96
90	203.297	203.799	1.77
120	212.291	212.502	1.46
150	217.092	217.182	1.25
180	219.235	219.515	1.41
210	220.078	220.679	1.51
240	220.952	221.237	1.52

(c) End winding temperature at nondrive-end part °C.

Time [min]	Study 1 [°C]	Study 2 [°C]	ΔE [%]
30	155.832	156.078	0.16
60	187.187	187.329	1.96
90	203.297	203.799	1.77
120	212.291	212.502	1.46
150	217.092	217.182	1.25
180	219.235	219.515	1.41
210	220.078	220.679	1.51
240	220.952	221.237	1.52

(d) Bearing temperature at nondrive-end part °C.

Table 4.1: Temperature comparison in motor part for Study 1 and 2.

An example of comparison between outlet temperature and measured values in figure 4.13 is shown.

It is noticeable the accuracy of Study 1 and 2 comparing with measurements values.

This will be better discussed in chapter 5.

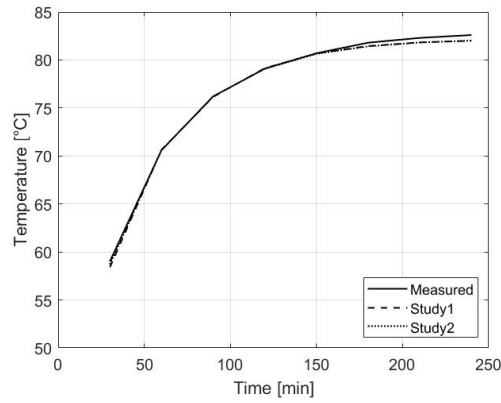


Figure 4.13: Measured and calculated outlet temperature for Study 1 and 2.

Finally, the temperature behaviour through graphic results can be analyzed. In figures 4.14 the behaviour of temperature increase in different time steps for Study 2, is shown. In figure 4.15 temperature detail is instead shown.

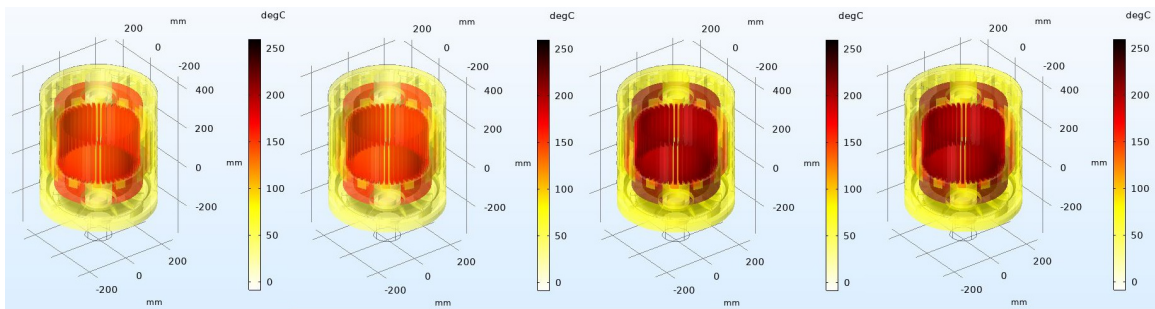


Figure 4.14: 3D view of inner temperature behaviour at 1800 s, 3600 s, 7200 s, 14400 s for Study 2.

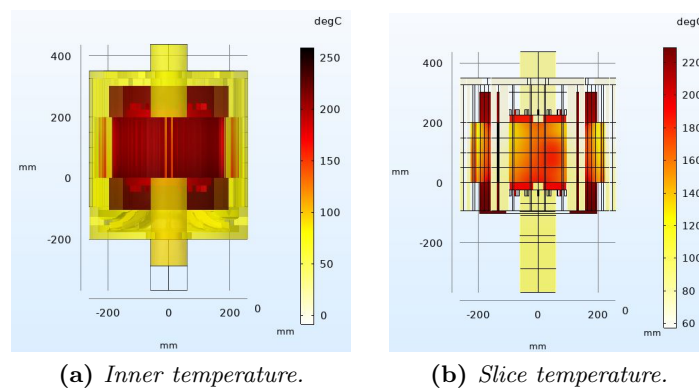


Figure 4.15: Temperature behaviour details for Study 1 (a) and 2 (b).

Chapter 5

Experimental Results

After that CFD and thermal model have been developed and relative results obtained, in order to verify the validity and accuracy of the calculated COMSOL results, the developed numerical and analytical methods have been verified and compared with experimental results done in laboratory. Experimental measurements both air flow and thermal behaviour for this motor case study have been made.

At last, chapter 5.4 is focused on another experimental thermal measurement method carried to the motor during the internship in ABB AB factory in Västerås (Sweden), in collaboration with Dr.-Ing. Shafiqh Nategh, his ABB AB team and Prof. Aldo Boglietti (Politecnico di Torino).

All experimental measurements have been done at ABB AB laboratories in Västerås.

5.1 Experimental Measurements Setup

As in the previous chapters mentioned, in order to evaluate the flow calculations accuracy and the developed thermal model, a comparison between the flow and estimated temperature with the relative experimental measurements done on an air-cooled traction motor designed and built by ABB has been done.

The traction motor analyzed in this case study has been chosen considering on the complexity. Open self-ventilated traction motor, considering their complex cooling structure, are known to be challenging to model in fluid dynamics and also thermally.

The cooling of this motor includes axial inlet where the air is sucked in, radial outlet, shaft-mounted fan and three parallel cooling paths including stator ducts, rotor ducts and air gap. Additionally, small blades on the rotor short-circuit ring provide extra turbulence in the motor end parts [2],[8], [9].

The rating data of the reference motor and a picture of the motor are shown in table 5.1¹ and in figure 5.1 .

¹Provided by ABB

Parameter	Value
V_{nom}	1100 V
I_{nom}	170 A
P_{nom}	245 kW
U_{rot}	1914 rpm

Table 5.1: Data rating for CFD measurements.



Figure 5.1: View of the motor.

5.2 Flow Measurements

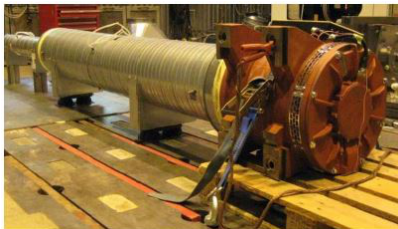
As mentioned, when the motor model has been explained, CFD calculation includes simplifications and optimizations with the aim of reducing the calculation time. Consequently, an accurate measurement of flow in the motor is needed to validate the developed quick CFD model.

Flow rate measurements considering a long tunnel connected to the motor to achieve the flow straight and uniform have been realized. The optimum length of the tunnel is estimated using a separate CFD calculation modeling the test setup [5].

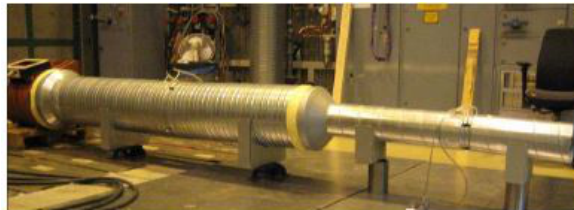
In particular, the tube before to be linked to the motor, is divided in three lengths with different diameters; the first part is around 1530 mm, the second 2360 mm and the third 200 mm, as shown in figure 5.2, 5.3.



Figure 5.2: Flow measurement setup scheme.



(a) View of flow measurement setup.



(b) Detail of flow measurement setup.

Figure 5.3: Flow measurement setup.

The air flow measurements, expressed as volume flow rate (m^3/s), are achieved considering a rotation speed range equal to 750, 2250, 3000, 3750 and 4110 rpm and through PVM100 micromanometer are measured.

The obtained flow results are reported in table 5.2 and plotted in the figure chart 5.4, respectively where, in order to compare the measurements and calculated flow rate values, through EXCEL implementation, the percentage difference at 2100 rpm calculated is less than 4%.

Rotation speed [rpm]	Frequency [Hz]	Tube diameter [mm]	Mixed Pressure Mixed [Pa]	Flow rate [m^3/s]
750	25	200	16.0	0.1112
1500	50	200	72.0	0.2359
2250	75	200	165.0	0.3571
3000	100	200	295.0	0.4774
3750	125	200	452.0	0.5910
4110	137	200	532.0	0.6412

Table 5.2: Flow rate experimental results.

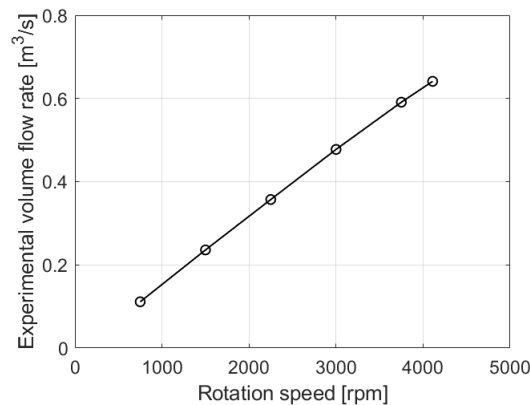


Figure 5.4: Experimental volume flow rate measurements. Linearity trend could be observed.

In figure 5.5, considering the flow results obtained in COMSOL and explained in chapter 3, is possible to compare the experimental flow rate results and the mesh results.

A good agreement between modeling results and measurements has been achieved; in particular an increase of the mesh quality corresponds a better overlap between results. In conclusion, the calculation time has been reduced to minutes for flow estimation in the complete motor operation range, starting from hour and ending to minutes guaranteeing, anyway, the validity of results and the trend linearity that, as mentioned, has been important because it allows to avoid calculating the results for each rotation speed [4].

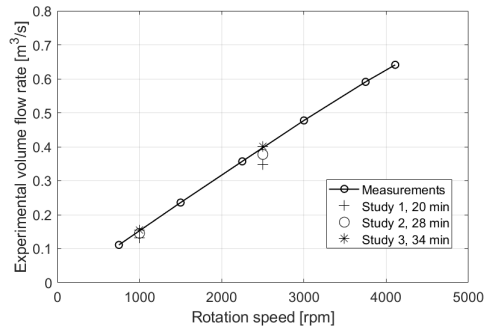


Figure 5.5: Measured and calculated flow rate results at different mesh qualities.

5.3 Thermal Measurements

About the thermal measurements, in order to give an accurate evaluation of the results, the tested motor with different temperature sensors has been equipped. PT100 sensors in different parts of the stator lamination and in the end winding hot side, bearing, short circuit rings and rotor active part have been placed. Then the motor in order to evaluate the temperature measurements that are carried out when running the motor in both steady-state and duty-cycles to the instruments has been linked.

Thermal experimental setup and data rating to run the test in table 5.3² and 5.6 are reported.

Parameter	Value
V_{nom}	1100 V
I_{nom}	160 A
P_{nom}	230 kW
U_{rot}	2163 rpm

Table 5.3: Data rating for thermal measurement.



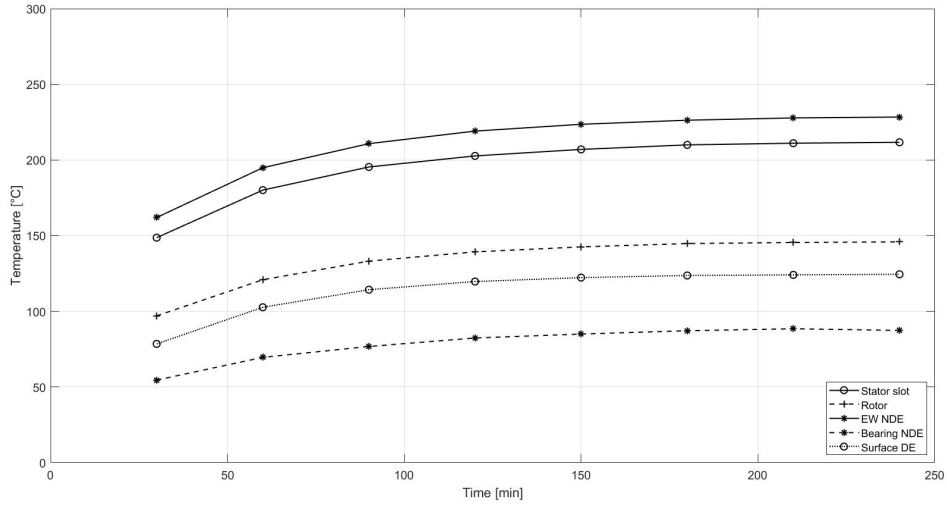
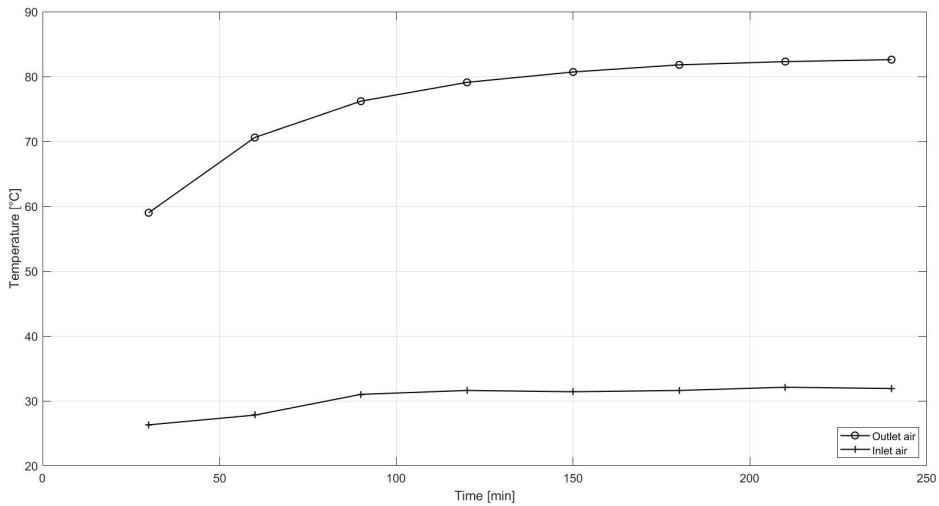
Figure 5.6: View of thermal measurement setup.

The results considering 27 sensors placed in different points for a testing time equal to 4 hours are obtained [4].

Supplying with a voltage less than a rated value and a rated current different thermal measurements have been obtained.

In figure 5.7(a), the temperature trend of end winding, stator slot, rotor, bearing and surface, considering for each part only one sensor, are reported. Thermal temperature measurements relative to inlet and outlet, as instead shown in figure 5.7(b), where the outlet temperature increase is noticeable.

²Provided by ABB

(a) *Experimental air temperature in different motor parts.*(b) *Experimental air temperature in inlet and outlet.***Figure 5.7:** Thermal experimental measurements.

At last, for thermal measurements as well, a comparison between experimental and simulation results for outlet, stator slot, end winding and bearing at nondrive-end part, considering the mesh types in chapter 4 discussed, are reported in table 5.4 where the difference between experimental and Study 2 values is calculated and shown in figure 5.8.

Time [min]	Study 1 [°C]	Study 2 [°C]	Measured [°C]	ΔE [%]
30	58.392	58.696	59.0	0.52
60	70.642	70.594	70.6	0.01
90	76.159	76.211	76.2	0.01
120	79.140	79.082	79.1	0.02
150	80.694	80.640	80.7	0.07
180	81.447	81.425	81.8	0.46
210	81.830	81.824	82.3	0.58
240	82.001	82.020	82.6	0.71

(a) Outlet temperature °C.

Time [min]	Study 1 [°C]	Study 2 [°C]	Measured [°C]	ΔE [%]
30	146.640	147.052	148.7	1.12
60	176.729	176.876	180.1	1.82
90	192.720	193.010	195.4	1.24
120	201.514	201.539	202.7	0.58
150	206.041	206.107	207.0	0.43
180	208.248	208.375	210.0	0.78
210	209.287	209.518	211.1	0.76
240	209.820	210.075	211.7	0.77

(b) Stator slot temperature °C.

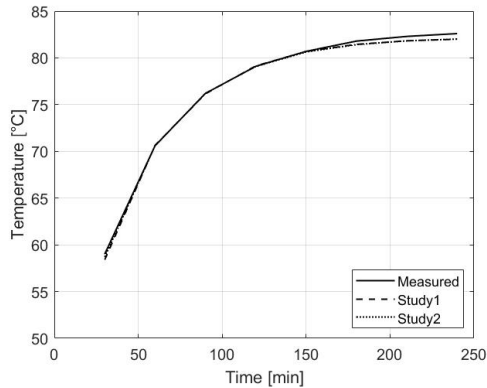
Time [min]	Study 1 [°C]	Study 2 [°C]	Measured [°C]	ΔE [%]
30	161.212	161.310	162.0	0.43
60	193.614	193.862	194.9	0.54
90	210.553	210.882	210.8	0.04
120	219.858	219.884	219.1	0.36
150	224.618	224.712	223.6	0.49
180	226.980	227.113	226.3	0.36
210	228.101	228.325	227.8	0.23
240	228.632	228.917	228.4	0.23

(c) End winding temperature at nondrive-end part °C.

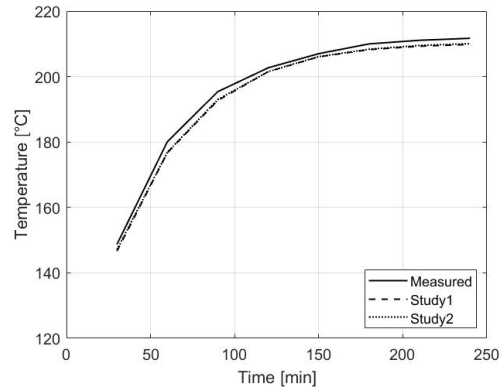
Time [min]	Study 1 [°C]	Study 2 [°C]	Measured [°C]	ΔE [%]
30	51.708	51.402	54.6	6.22
60	67.970	67.962	69.6	2.41
90	78.230	78.239	76.8	1.84
120	84.126	84.016	82.4	1.92
150	87.232	87.163	85.0	2.48
180	88.798	88.751	87.2	1.75
210	89.551	89.559	88.5	1.18
240	89.907	89.956	87.4	2.84

(d) Bearing temperature at nondrive-end part °C.

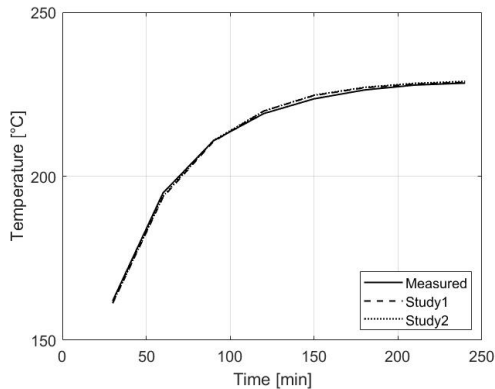
Table 5.4: Thermal numerical comparison between calculated and measured results.



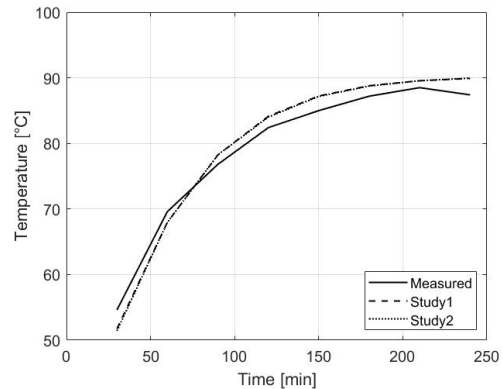
(a) Outlet thermal results comparison.



(b) Stator thermal results comparison.



(c) End winding at nondrive-end part thermal results comparison.



(d) Bearing at nondrive-end part comparison.

Figure 5.8: Measured and calculated thermal results at different motor parts for Study 1 and 2.

5.4 Short-Time Transient Thermal Measurements Method

As previously mentioned, to conclude this work, during the internship period in Västerås (Sweden), in order to know and evaluate the thermal motor behaviour, another experimental method on the motor has been done and applied.

The applied approach is based on the *short-time thermal transient identification method* that allows to know the slot thermal parameters of induction motors for different applications.

The generalized model considers the mutual heat exchange between the windings and the possible problems of temperature mismatch. This model also considering lumped parameters thermal-network has been developed.

In general, through this procedure is possible to improve the accuracy of the steady-state and transient thermal estimated during the machine design and building an accurate transient thermal model that for temperature checking can be used.

5.4.1 Experimental Test Setup

Laboratories, instruments and tests have been an ABB AB concession.

Considering that in the electric motors to the stator winding region is attributed the main heat source in the machine, it imposes the most important temperature limit. This zone, in fact, is characterized by a random distributed composite where the behaviour depends on several factor such as winding arrangement, impregnation technique and material physical parameters. To can get the temperature predictions, *equivalent thermal resistance* R_{Θ} and *equivalent thermal capacitance* C_{Θ} are considered [9],[10].

The first represents the heat transfer between stator copper and iron lamination and the second represents the thermal capacitance of the winding system, considering conductor and insulation.

To analyze the parameters, in figure 5.9 is shown the scheme of adopted method.

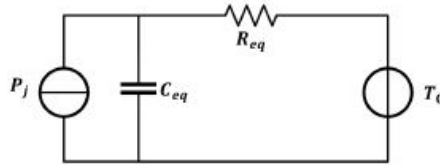


Figure 5.9: First order winding thermal modeling scheme.

In this way, winding system is modeled as a first-order thermal network where the current generator is inserted to represent Joule power loss P_j in the winding, instead R_{Θ} and C_{Θ} represent the thermal resistance from the winding to the stator core iron and the thermal capacitance of winding plus insulation respectively.

Both R_{Θ} and C_{Θ} can be evaluated by means of the transient DC test.

The method consists on the heating the stator windings of the motor by the injection of a DC current, in the order of magnitude of the rated value. The heat source is localized in the windings and iron and mechanical losses are generated. The isothermal operating condition for the stator assembly is considered accepted for the averaged stator temperature rise up to 1°C [5].

Considering that the *initial temperature* T_0 and *initial winding resistance* R_0 are known from the winding resistance variation, using the material temperature coefficient, it is possible to estimate the average winding temperature as:

$$T = \frac{R_T}{R_0}(234.5 + T_0) - 234.5 \quad (5.1)$$

where R_T [Ohm] is the *winding resistance* at the temperature T and 234.5 is the inverse of copper temperature coefficient.

The mathematical solution of the thermal network can be described by a first order differential equation 5.2 where all the variables are known and R_{Θ} can be obtained minimizing the squared deviation between the measured temperature with the sensor and the one achieved by means of the mathematical model, as reported below in 5.4 and 5.5 [11].

$$T(t) = T_0 + P_j R_{\Theta} (1 - e^{-\frac{t}{\tau}}) \quad (5.2)$$

$$T(t) = T_0 + T_{\infty} (1 - e^{-\frac{t}{\tau}}) \quad (5.3)$$

where $T_{\infty} = P_j R_{\Theta}$ and $\tau = R_{\Theta} C_{\Theta}$ is the *time constant*, can be used to predict the temperature increase during.

$$T_i = T_{i-1} + (T_0 + P_{i-1} R_{\Theta} - T_{i-1}) (1 - e^{-\frac{t_i - t_{i-1}}{\tau}}) \quad (5.4)$$

$$\Delta E = \frac{(T_i - T_{i-1})^2}{(T_{i-1})^2} \quad (5.5)$$

Considering that iron core temperature and T_0 are around equal, the initial step of the temperature transient is adiabatic.

In this way is possible to represent the thermal energy dissipated calculated from the electric power as:

$$W(t) = \int v(t) i(t) dt \quad (5.6)$$

From the *accumulated energy* W , the thermal capacitance is obtained from the slope of dissipated energy as a function of the overtemperature approximated with a straight line, described by:

$$C_{\Theta} = \frac{dW}{dT} \quad (5.7)$$

Then, knowing C_{Θ} , the thermal resistance R_{Θ} is calculated from the time constant τ of the fitting exponential functions 5.2 and 5.3.

The experimental setup considering thermal sensors placed in the end windings to evaluate the temperature has been made.

The current values, exploiting an amperometric clamp (“pinza amperometrica”) and a shunt have been measured and compared. Measurements of voltage, current and temperature for one hour have been continuously recorded where, to acquire data, a sample times equal to 0.1, 1 and 5 seconds have been considered.

For this case study, a sample time equal to 5 seconds has been demonstrated be a good compromise, as discuss below.

Finally, to log and elaborate the data, Yokogawa 1800 power analyzer has been used.

To evaluate the thermal parameters the procedure requires to supply the stator phases with a current obtained from a DC power supply, according to the V-I, based on the assumption that the stator lamination is isothermal during a short-time thermal transient.

Considering this, the test should be interrupted when the stator lamination temperature increases by 1°C , where the error is more than of a fixed error threshold. Considering that the neutral point of induction motor is often not accessible, testes have been realized feeding in series only two phases at a time, U-W and V-W respectively (the first test is not considered).

In this way the thermal capacitance and resistance values are obtained referring to two-phase set and then, to refer them to three-phase set, a corrective factor has been applied, as discuss in below. Furthermore, to consider only one two phases for test, in the thermal resistance evaluation is relevant.

Finally, this setting test allowed to compare the thermal measurements of the tests and to evaluate the validity, considering that the test behaviour should be the same.

5.4.2 Experimental Test Results

I. Test 1

In the first stage, the test with a sample time equal to 0.1 seconds has been done. In this way, running for 1 hour, a high number of samples have been elaborated, allowing difficult to obtain accurate results. In fact, as shown in figure 5.10(a), the resistance trend is not linear as expected, instead the end winding temperature shown in 5.10(b), measured through sensor, is acceptable. The considered time is equal to 3600 seconds.

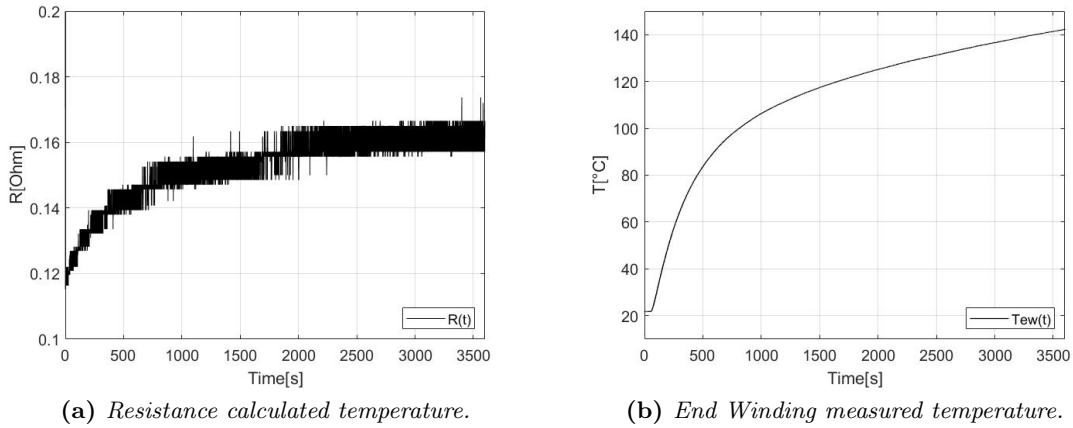


Figure 5.10: Test 1: Resistance (a) and End Winding (b) calculated temperature – Time 3600 s.

To improve the results and to obtain an increasing trend has been thought to filter them or to reduce the evaluation time but, as noticeable in figures 5.11(a) and 5.11(b), the trends are not acceptable yet.

In particular in (a) a filter equal to 5 s and an evaluation time equal to 900 seconds have been applied. In (b), instead, the filter is equal to 10 seconds, considering 3600 seconds.

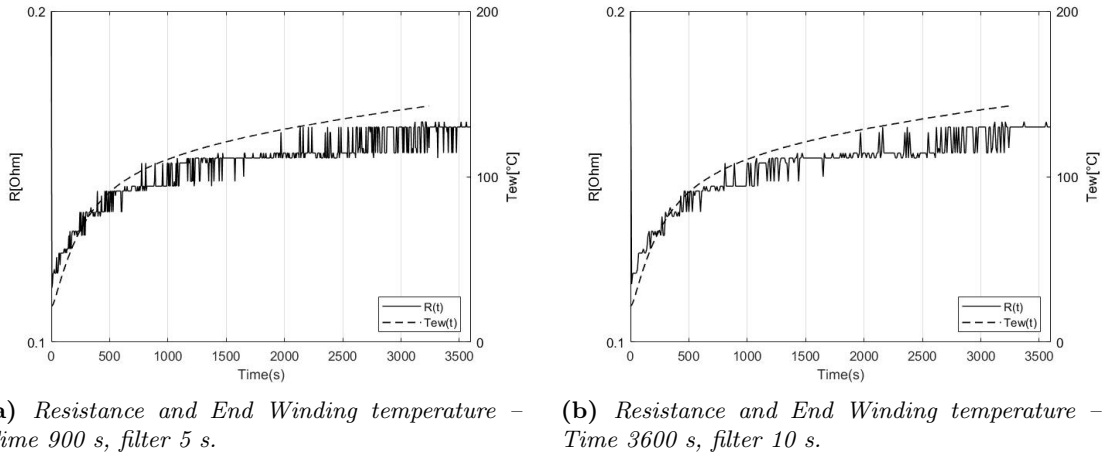


Figure 5.11: Test 1: Test 1: Resistance and End winding filtered temperature with 5 s (a) and 10 s (b).

II. Test 2

Considering the unacceptable results of the first test, in the second one a sample time equal to 1 second and some improvements, during and post-test, have been applied. The supplied phases are U-W.

Then, in figure 5.12 the comparison between the original resistance trend and the end winding measured temperature for a time equal to 3600 seconds is plotted.

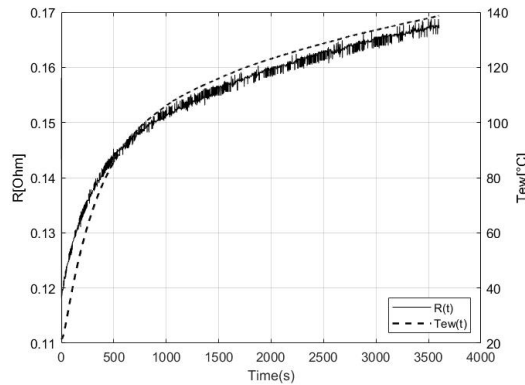


Figure 5.12: Test 2: Resistance calculated temperature – Time 3600 s.

The trend is slightly better than the first test, but the accuracy is unacceptable.

However, applying a moving average function with sample time equal to 10 seconds, an important improvement has been obtained. In this way the trend is more linear and the results accuracy can be considered acceptable, as shown in figure 5.13.

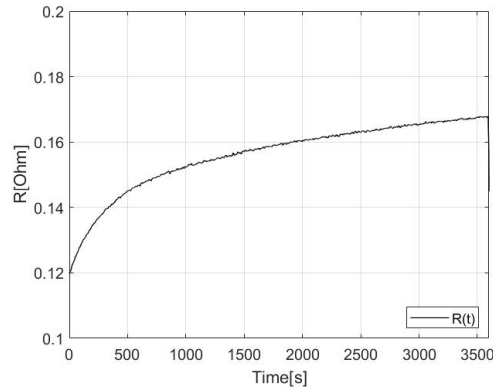


Figure 5.13: Test 2: Filtered resistance temperature – Time 900 s, filter 5 s.

Processing the results of current, voltage, temperature and time, the evaluated values of thermal resistance and capacitance, from 5.7, are equal to:

$$C_{\Theta} = 14393 \text{ J/K}$$

$$R_{\Theta} = 0.025 \text{ W/K}$$

From this, the trend of energy $W(t)$ calculated as in 5.6 in figure 5.14(a) is shown and, applying the 5.3, the temperature trend, comparing experimental and computed, is reported in figure 5.15. The moving average allows to notice that the winding first order thermal model is valid for a time interval equal around to 600 seconds (10 minutes) where the comparison between computed and experimentally measured trend demonstrates a good coincidence.

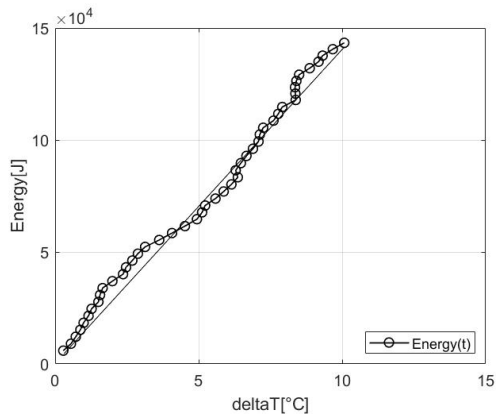


Figure 5.14: Test 2: Elaborated energy trend.

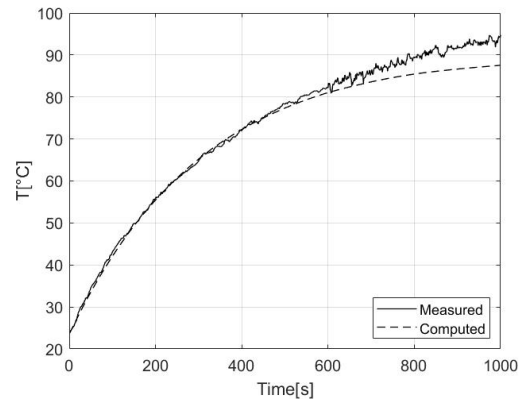


Figure 5.15: Test 2: Temperature comparison.

III. Test 3

Finally, the last one experimental test, considering a sample time equal to 5 seconds has been done. The supplied phases are V-W.

In this case, realizing a good setting to the data logger and considering the improvements obtained for the second test, the experimental and computed results are perfectly coincident.

Starting from the measurement results, in figure 5.16 is possible to observe the linearity of the resistance and end winding trend, to demonstrate that two phenomena should have perfectly the same trend.

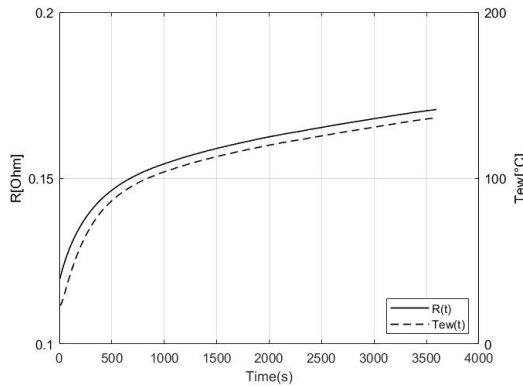


Figure 5.16: Test 3: Resistance calculated temperature – Time 3600 s.

Processing the test results, the thermal capacitance and resistance have been calculated. They are more reliable for this case study and equal to $R_{\Theta} = 16282 \text{ J/K}$, $C_{\Theta} = 0.027 \text{ W/K}$.

Considering that the values with two phases has been done, referring them to three phases, they are:

$$C_{\Theta_2} = 16282 \text{ J/K} \rightarrow C_{\Theta_3} = 16282 \left(\frac{3}{2}\right) \text{ J/K} = 24423 \text{ J/K}$$

$$R_{\Theta_2} = 0.027 \text{ W/K} \rightarrow R_{\Theta_3} = 0.027 \left(\frac{3}{2}\right) \text{ W/K} \leq 0.018 \text{ W/K}$$

In R_{Θ_3} the \leq has been used because it cannot into account that the inactive phase U contributes in cooling the active zone. In fact, exists a contact between the end-winding of each phases set that allows an additional thermal path between the active set and the inactive one where the thermal resistance is influenced. In similar way to test 2, the trend of energy $W(t)$ from to 5.6 and the temperature comparison behaviour from to 5.3 are calculated and plotted in figure 5.17 and 5.18 respectively.

In 5.18 the first order model could be observed for the first 600 s.

The similar trend of experimental and computed results showing the validity and accuracy of the method are evaluated.

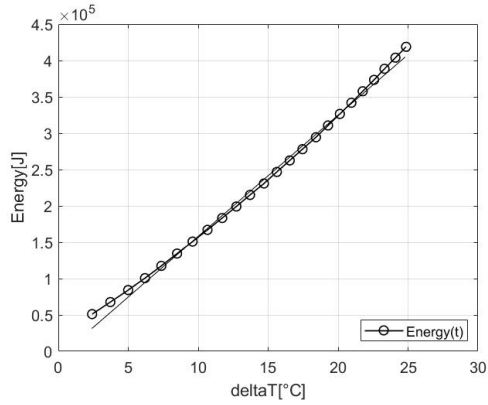


Figure 5.17: Test 3: Elaborated energy trend.

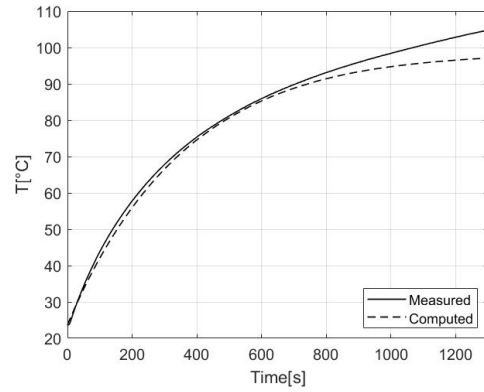


Figure 5.18: Test 3: Temperature comparison.

However, a further results improvement to compute the equivalent thermal parameters through Excel and MATLAB algorithms has been guaranteed. In this way, the updated thermal capacitance, resistance and conductivity are equal respectively to:

$$\begin{aligned}
 C_{\Theta_2} = 14324 \text{ J/K} &\rightarrow C_{\Theta_3} = 14324 \left(\frac{3}{2}\right) \text{ J/K} = 21483 \text{ J/K} \\
 R_{\Theta_2} = 0.0246 \text{ W/K} &\rightarrow R_{\Theta_3} = 0.0246 \left(\frac{3}{2}\right) \text{ W/K} \leq 0.016 \text{ W/K} \\
 K_{\Theta_2} = 0.0796 \text{ W/(m}\cdot\text{K)} &\rightarrow K_{\Theta_3} = 0.1194 \text{ W/(m}\cdot\text{K)} \text{ Thermal conductivity}
 \end{aligned}$$

The evaluated energy and temperature trends, after the developed algorithm, are instead shown in figures 5.19 and 5.20 respectively.

In particular in 5.20 it should be noted that the measured and computed values are perfectly overlapped for the first 600 seconds guaranteeing, for the winding first order model, an excellent accuracy and validity of the work [5].

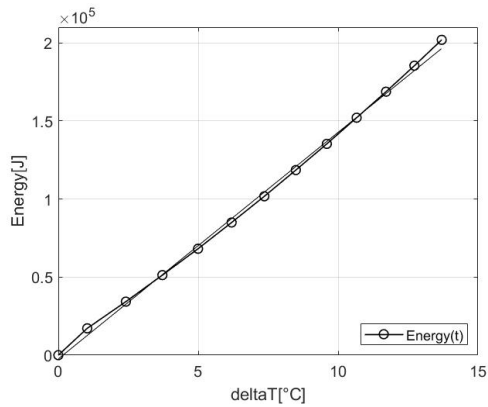


Figure 5.19: Test 3: Improved elaborated energy trend.

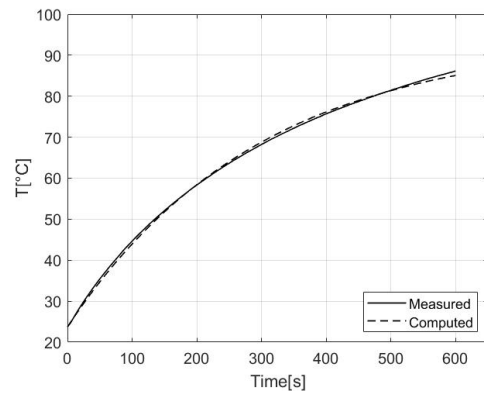


Figure 5.20: Test 3: Improved temperature comparison.

Chapter 6

Conclusion and Future Works

In this chapter a short summary and conclusion about the achieved results are discussed. Also, ideas and possible future works linked to the results carried out study are dealt.

6.1 Final Summary

In this thesis, thermal behaviour of electrical motor for railway and e-mobility traction have been studied.

The focus has been reserved on the hybrid approach based on CFD calculation to calculate flow and consequently temperature to give an accurate modeling of heat transfer in the electrical machines critical parts when the motor run in intermittent operations. The developed study through Analytical and Numerical method with Finite Elements methods and CFD simulations have been done.

In particular, to estimate the winding hot spot temperature and the temperature distribution, the analytical approach by numerical approach has been replaced, with good accuracy.

Then, the FE numerical results to know all temperature behaviour have been considered. In this way the proposed modeling can be applied how a general method to know the heat transfer.

CFD simulations to estimate the fluid distribution in the motor, e.g. in stator, rotor ducts and air gap, with COMSOL tool have been done. Then, the obtained CFD results to model the heat transfer have been applied. Through EXCEL implementation, from flow rate and air velocity results, heat transfer coefficients have then calculated and in the thermal model applied.

It has been demonstrated that the linearity trend of CFD simulations allows to give a significantly reduction of the calculation time both for flow and thermal calculations where it has been reduced to minutes to estimate the flow and to seconds per operating point in thermal calculations.

Furthermore, the temperature distribution prediction in the motor with a great accuracy and reliability of the proposed model has been demonstrated to be possible.

Finally, flow and thermal experimental measurements have been evaluated to compare the calculated results, achieving once again a good agreement between modeling results and measurements.

At last, the *Short-Time Transient Thermal Measurements Method* has been validated with great accuracy comparing the measured and calculated values.

6.2 Future Developments

Being aware that the thermal effects have an important role during the motor life cycle and that a correct evaluation and estimation of the behaviour could improve it, the good accuracy results allows, starting from this study, to can develop a possible generic method also valid for other motors.

In particular, both the time calculation reduction, the linearity behaviour and the heat transfer prediction represent a good prospective to develop and improve the future study and the future thermal motor behaviour.

Furthermore, through COMSOL tool, a possible partnership between ABB and COMSOL could be possible in order to develop a simple but accurate model able to evaluate the thermal effect in the traction motors.

Appendix A

List of Acronyms

In this appendix, acronyms and symbols used in the thesis are listed.

Acronym	Meaning
CFD	Computational Fluid Dynamic
LP	Lumped Parameter
FE	Finite Element
FEA	Finite Element Analysis
FEM	Finite Element Method
FV	Finite Volume
FVM	Finite Volume Method
FDM	Finite Difference Method
DNS	Direct Numerical Simulation
LES	Large Eddy Simulation
RANS	Reynold-Averaged Navier-Stokes
PDE	Partial Differential Equations
2D	Two Dimensional
3D	Three Dimensional
k	Turbulent kinetic energy
ϵ	Turbulent dissipation rate conductivity
ω	Angular displacement
σ	Angular velocity vector
ρ	Density
μ	Dynamic viscosity

Acronym	Meaning
P	Pressure
F	Force
A	Area
P_{st}	Static pressure
P_{dy}	Dynamic pressure
g	Gravity
U,u	Air velocity
V	Volume
t	Time
Q_v	Volumetric flow rate
Gb	Gigabyte
Re	Reynolds number
Re_{rd}	Radial Reynolds number
Re_{ax}	Axial Reynolds number
N_u	Nusselt number
P_r	Prandtl number
k_{Θ}	Fluid thermal conductivity
Lc	Characteristic length
La	Active length
H_{duct}	Duct height
W_{duct}	Duct width
p	Perimeter
f	Friction factor
D	Equivalent diameter
$B_{duct_{max}}$	Major base in duct
$B_{duct_{min}}$	Minor base in duct
D_{RO}	Outer rotor diameter
D_{SI}	Inner stator diameter
L_{ag}	Radial air gap length
v_r, U_{rot}	Rotational velocity
T_a	Taylor number
T	Temperature
q	Conduction heat flux

Acronym	Meaning
q_r	Radiation heat flux
Q	Additional heat sources
P_0	Initial power losses
C_p	Specific heat
V_{nom}	Rated velocity
I_{nom}	Rated current
P_{nom}	Rated power
R_{Θ}	Thermal resistance
C_{Θ}	Thermal capacitance
P_j	Joule power loss
T_0	Initial temperature
R_0	Winding resistance
τ	Time constant

Appendix B

List of Measurement Units

In this appendix, the most used Measurement Units are listed.

Symbol	Unit	Meaning
V	Volt	Voltage
A	Ampere	Current
W	Watt	Power
J	Joule	Energy
m	Meter	Length
s	Seconds	Time
kg	Kilogram	Weight
Hz	Hertz	Frequency
m ²	Square Meters	Area
m ³	Cubic Meters	Volume
rpm	Revolutions per Minutes	Rotational speed
m/s	Meters per Second	Air speed
m/s ²	Meter per Square Second	Acceleration
m ³ /s	Cubic Meters per Second	Volumetric flow rate
kg/s	Kilograms per Second	Mass flow rate
kg/m ³	Kilograms per Cubic Meters	Density
Pa	Pascal	Pressure
K, °C	Kelvin, Celsius degree	Temperature
J/(kg·K)	Joule per Kilogram Kelvin	Specific heat capacity
W/(m·K)	Watt per Meter Kelvin	Thermal Conductivity

Appendix C

List of Selected Publications

In this appendix the selected publications from this thesis and project are listed.

I. PAPER I

C. Scema, S. Nategh, A. Boglietti, L. Boscaglia, D. Ericsson, "A Hybrid Thermal Modeling Method for Traction Motors Used in Duty-Cycles", IEEE International Electric Machines and Drives Conference (IEMDC), San Diego (CA), May 2019.

II. PAPER II

S. Nategh, A. Boglietti, E. Carpaneto, C. Scema, L. Boscaglia, "An Optimization Method for Cooling System Design of Traction Motors", IEEE International Electric Machines and Drives Conference (IEMDC), San Diego (CA), May 2019.

III. PAPER III

L. Boscaglia, S. Nategh, A. Boglietti, C. Scema, F. Bonsanto, "Conjugate Heat Transfer Model for Self Ventilated Traction Motors" ¹

¹Submitted in IEEE Energy Conversion Congress and Expo (ECCE), Baltimore (MD), Sept. 2019

List of Figures

1.1	Open air forced ventilated motors [1].	4
1.2	Open air self-ventilated electric traction motor [1].	5
1.3	Enclosed air self-ventilated motor electric traction motor [1].	5
1.4	Comparison between estimated (brown) and measured (green) temperature of the end winding (a) and of the bearing (b), at specific torque (black) and speed (blue) [2].	6
1.5	Example of analytical LP model of the end winding [2].	7
1.6	Example of lumped parameters thermal model of an electric motor [3].	8
1.7	Example of thermal FE model of the stationary part of an electric motor [3].	10
1.8	Example of velocity in CFD motor model.	10
2.1	Example of list of parameters of fan building.	18
2.2	View of fan.	19
2.3	View of air guide.	19
2.4	View of fan and air guide.	19
2.5	Work plane window.	20
2.6	Geometrical shapes window.	20
2.7	Examples of geometry building.	20
2.8	Examples of defeaturing and repair function.	21
2.9	Example of delete faces function to remove details.	21
2.10	2D (a), (c) and 3D (b), (d) outer and inner fan model view	22
2.11	Boundary condition setting.	24
2.12	Boundary condition selection.	24
2.13	Example of boundary condition setting.	25
2.14	Solver setting.	28
2.15	Example of elements with structured and free tetrahedral mesh.	30
2.16	Example of 3D elements and free tetrahedral mesh.	30
2.17	Virtual operation example.	31
2.18	Mesh setting.	32
2.19	Mesh results.	32
2.20	Pressure and flow rate trends at $v_{rot1} = 2500$ rpm.	36
2.21	Graphics results for $p_{tot_in} = -100$ Pa and -1100 Pa at $v_{rot1} = 2500$ rpm. .	37
2.22	Pressure and flow rate trends at $v_{rot1} = 1500$ rpm.	39

2.23	Graphics results for $p_{tot_in} = -100$ Pa and -500 Pa at $v_{rot1} = 1500$ rpm. . .	40
2.24	Pressure and flow rate trends at $v_{rot1} = 2000$ rpm.	42
2.25	Graphics results for $p_{tot_in} = -100$ Pa and -500 Pa at $v_{rot1} = 2000$ rpm. . .	43
3.1	Example of rotor parameters.	46
3.2	2D (a) and 3D (b) view of motor model.	46
3.3	Example of boundary conditions selection.	47
3.4	Mesh setting.	49
3.5	2D (a) and 3D (b) comparison for mesh 1 and 2	50
3.6	Mesh 2 statistic.	51
3.7	3D view of CFD model mesh results.	52
3.8	Flow rate increase in function of rotational speed at 20°C for Study 1 and Study 2. Flow linearity could be observed.	53
3.9	Air speed increase comparison. Trend linearity could be observed.	54
3.10	Graphics results at $v_{rot1} = 2500$ rpm for Study 1 and 2 respectively.	55
3.11	Comparison between CFD calculation results for flow rate at different mesh qualities.	56
4.1	Thermal model algorithm.	58
4.2	3D-FE Model scheme [2].	59
4.3	Heat transfer behaviour function of velocity.	61
4.4	HTC Excel algorithm.	64
4.5	3D view of motor model.	65
4.6	Thermal contact setup.	66
4.7	Heat source setup.	66
4.8	Example of material selection.	67
4.9	Heat flux setup.	68
4.10	3D view comparison of thermal model mesh qualities.	69
4.11	3D view comparison of thermal model mesh results.	69
4.12	Temperature comparison in outlet (a) and stator slot (b) for Study 1 and 2.	70
4.13	Measured and calculated outlet temperature for Study 1 and 2.	72
4.14	3D view of inner temperature behaviour at 1800 s, 3600 s, 7200 s, 14400 s for Study 2.	72
4.15	Temperature behaviour details for Study 1 (a) and 2 (b).	72
5.1	View of the motor.	74
5.2	Flow measurement setup scheme.	74
5.3	Flow measurement setup.	74
5.4	Experimental volume flow rate measurements. Linearity trend could be observed.	75
5.5	Measured and calculated flow rate results at different mesh qualities.	76
5.6	View of thermal measurement setup.	76
5.7	Thermal experimental measurements.	77

5.8 Measured and calculated thermal results at different motor parts for Study 1 and 2.	79
5.9 First order winding thermal modeling scheme.	80
5.10 Test 1: Resistance (a) and End Winding (b) calculated temperature – Time 3600 s.	82
5.11 Test 1: Test 1: Resistance and End winding filtered temperature with 5 s (a) and 10 s (b).	83
5.12 Test 2: Resistance calculated temperature – Time 3600 s.	83
5.13 Test 2: Filtered resistance temperature – Time 900 s, filter 5 s.	84
5.14 Test 2: Elaborated energy trend.	84
5.15 Test 2: Temperature comparison.	84
5.16 Test 3: Resistance calculated temperature – Time 3600 s.	85
5.17 Test 3: Elaborated energy trend.	86
5.18 Test 3: Temperature comparison.	86
5.19 Test 3: Improved elaborated energy trend.	86
5.20 Test 3: Improved temperature comparison.	86

List of Tables

1.1	List of model parameters [3].	8
2.1	Comparison of advantages and disadvantages for FE and FV.	17
2.2	Simulation results at 2500 rpm - Computation time: Study 1: 2h 52min, Study 2: 5h 25min.	35
2.3	Simulation results at 1500 rpm - Computation time: Study 1: 3h 27min, Study 2: 5h 25min.	38
2.4	Simulation results at 2000 rpm - Computation time: Study 1: 2h 46min, Study 2: 5h 25min.	41
3.1	Mesh 1 and mesh 2 comparison.	52
3.2	Air speed (a) and volume flow rate (b) results at 20°C for Study 1 and Study 2.	54
4.1	Temperature comparison in motor part for Study 1 and 2.	71
5.1	Data rating for CFD measurements.	74
5.2	Flow rate experimental results.	75
5.3	Data rating for thermal measurement.	76
5.4	Thermal numerical comparison between calculated and measured results. . .	78

Bibliography

- [1] S. Nategh, D. Lindberg, O. Aglen, R. Brammer and A. Boglietti, *Review and Trends in Traction Motor Design: Electromagnetic and Cooling System Layouts*, 2018 XIII International Conference on Electrical Machines (ICEM), Alexandroupoli, 2018, pp. 2600-2606.
- [2] S. Nategh, H. Zhang, O. Wallmark, A. Boglietti, T. Nassen and M. Bazant, *Transient Thermal Modeling and Analysis of Railway Traction Motors*, in IEEE Transactions on Industrial Electronics, vol. 66, no. 1, pp. 79-89, Jan. 2019.
- [3] S. Nategh, *Thermal Analysis and Management of High-Performance Electrical Machines*, Ph.D. Dissertation, KTH Royal Institute of Technology, Stockholm, Sweden, June 2013.
- [4] C. Scema, S. Nategh, A. Boglietti, L. Boscaglia, D. Ericsson, *A Hybrid Thermal Modeling Method for Traction Motors Used in Duty-Cycles*, IEEE International Electrical Machines and Drives Conference (IEMDC), San Diego, CA, USA, May 2019.
- [5] S. Nategh, A. Boglietti, E. Carpaneto, C. Scema, L. Boscaglia, *An optimization method for cooling system design of traction motors*, International Electric Machines and Drives Conference (IEMDC), May 2019.
- [6] D. A. Staton and A. Cavagnino, *Convection Heat Transfer and Flow Calculations Suitable for Analytical Modelling of Electric Machines*, IECON 2006 - 32nd Annual Conference on IEEE Industrial Electronics, Paris, 2006, pp. 4841-4846.
- [7] D. A. Howey, P. R. N. Childs and A. S. Holmes, *Air-Gap Convection in Rotating Electrical Machines*, in IEEE Transactions on Industrial Electronics, vol. 59, no. 3, pp. 1367-1375, March 2012.
- [8] A. Boglietti, M. Cossale, S. Vaschetto and T. Dutra, *Winding Thermal Model for Short-Time Transient: Experimental Validation in Operative Conditions*, in IEEE Transactions on Industry Applications, vol. 54, no. 2, pp. 1312-1319, March-April 2018.
- [9] A. Boglietti, R. Bojoi, S. Rubino and M. Cossale, *Load Capability of Multiphase Machines under Normal and Open-Phase Fault Conditions*, 2018 IEEE Energy Conversion Congress and Exposition (ECCE), Portland, OR, 2018, pp. 242-247.

-
- [10] P. Pescetto, S. Ferrari, G. Pellegrino, E. Carpaneto and A. Boglietti, *Short-Time Transient Thermal Model Identification of Multiple Three-Phase Machines*, 2018 IEEE Energy Conversion Congress and Exposition (ECCE), Portland, OR, 2018, pp. 222-228.
- [11] D. Staton, A. Boglietti and A. Cavagnino, *Solving the more difficult aspects of electric motor thermal analysis in small and medium size industrial induction motors*, in IEEE Transactions on Energy Conversion, vol. 20, no. 3, pp. 620-628, Sept. 2005.
- [12] A. Boglietti, E. Carpaneto, M. Cossale and S. Vaschetto, *Stator-Winding Thermal Models for Short-Time Thermal Transients: Definition and Validation*, in IEEE Transactions on Industrial Electronics, vol. 63, no. 5, pp. 2713-2721, May 2016.
- [13] S. Nategh, S. Øvrebø, S. Mahdavi and O. Wallmark, *Thermal modeling of a permanent magnet machine built using Litz wire*, 2015 International Conference on Electrical Systems for Aircraft, Railway, Ship Propulsion and Road Vehicles (ESARS), Aachen, 2015, pp. 1-6.
- [14] D. Staton, A. Boglietti and A. Cavagnino, *Solving the more difficult aspects of electric motor thermal analysis*, IEEE International Electric Machines and Drives Conference, 2003. IEMDC'03., Madison, WI, USA, 2003, pp. 747-755 vol.2.
- [15] Ferziger J. H., Perić, *Computational Methods for Fluid Dynamics*, 3 ed., Springer, 2002.
- [16] Andersson B., Andersson R., Håkansson L., Mortensen M., Sudiyo R., van Wachem B., *Computational Fluid Dynamics for Engineers*, 1 ed., Cambridge, 2012.
- [17] Comini G., Croce G., Nobile E., *Fondamenti di Termofluidodinamica computazionale*, 4 ed., Servizi Grafici Editoriali, 2014.
- [18] Versteeg H. K., Malalasekera W., *An Introduction to Computational Fluid Dynamics*, 2 ed., Pearson Prentice Hall.
- [19] Kuzmin D., *A Guide to Numerical Methods for Transport Equations*, Friedrich-Alexander Universität, 2010.
- [20] Schnipke R. J., *A Streamline Upwind Finite Element Method for Laminar and Turbulent Flow*, Ph.D. Dissertation, School of Engineering and Applied Science University of Virginia, 1986.
- [21] Soldani G., *Metodo ai volumi finiti: Equazioni ellittiche*, Università di Padova, 2007.
- [22] COMSOL Multiphysics, *Reference Manual*, 2017.
- [23] COMSOL Multiphysics, *CFD Module: Application Library Manual*, 2017.
- [24] COMSOL Multiphysics, *Heat Transfer Module: Application Library Manual*, 2017.
- [25] COMSOL Multiphysics, *Heat Transfer Module: User's Guide*, 2017.

- [26] www.slideshare.net/Rahuldey1991/methods-of-cooling-of-electrical-machines.
- [27] www.mathematik.uni-dortmund.de/~kuzmin/cfdintro/lecture1.pdf.
- [28] www.knowledge.autodesk.com/support/cfd/learn-explore/caas/CloudHelp/cloudhelp/2017/ENU/SimCFD-Learning/files/GUID-12A9AED8-2047-4D3A-BC80-82BE9CF47517-htm.html.
- [29] www.cfd-online.com/Wiki/Finite_volume.
- [30] [/www.comsol.com/blogs/fem-vs-fvm/](http://www.comsol.com/blogs/fem-vs-fvm/).
- [31] www.researchgate.net/post/Is_FEM_has_any_advantages_over_FVM_Why_COMSOL_still_use_FEM.
- [32] www.cfd-online.com/Forums/main/197380-why-comsol-use-fem-instead-fvm.html.
- [33] www.eng-software.com/about-us/press/articles/understanding-the-distinction-between-total-static-and-dynamic-pressure/.
- [34] www.comsol.com/blogs/meshing-your-geometry-various-element-types/.
- [35] www.comsol.it/blogs/how-to-set-up-a-mesh-in-comsol-multiphysics-for-cfd-analyses/.
- [36] www.knowledge.autodesk.com/support/cfd/learn-explore/caas/CloudHelp/cloudhelp/2015/ENU/SimCFD-Learning/files/GUID-1E6EB6B4-4E07-45E4-958F-27ABD46E8C87-htm.html.
- [37] www.en.wikipedia.org/wiki/Nusselt_number.
- [38] www.engineeringtoolbox.com/air-prandtl-number-viscosity-heat-capacity-thermal-conductivity-d_2009.html.
- [39] www.en.wikipedia.org/wiki/Reynolds_number.
- [40] www.comsol.com/blogs/guidelines-for-modeling-rotating-machines-in-3d/.
- [41] www.comsol.se/model/centrifugal-pump-44191.
- [42] www.comsol.se/model/forced-convection-cooling-of-an-enclosure-with-fan-and-grille-6222.
- [43] www.en.wikipedia.org/wiki/Computational_fluid_dynamics.
- [44] Dispense di Fisica Tecnica, prof. Baccoli. R., Università di Cagliari, Ingegneria Elettrica ed Elettronica, a. a. 2013-2014.
- [45] Dispense di Macchine Elettriche II, prof. Cavagnino A., Politecnico di Torino, Dipartimento Energia, Ingegneria Elettrica, a. a. 2016-2017.
- [46] Dispense di Azionamenti Elettrici, prof. Pastorelli M., Politecnico di Torino, Dipartimento Energia, Ingegneria Elettrica, a. a. 2017-2018.

